Incorporation of species interdiffusion in boundary layer modelling of filmwise condensation with non-condensable gases

Nan Jiang

université PARIS-SACLAY

Incorporation of species interdiffusion in boundary layer modelling of filmwise condensation with non-condensable gases

Incorporation de l'interdiffusion des espèces dans la modélisation de la couche limite de condensation en film avec des gaz incondensables

Thèse de doctorat de l'université Paris-Saclay

École doctorale n°579, sciences mécaniques et énergétiques, matériaux et géosciences (SMEMaG)
Spécialité de doctorat : mécanique des fluides
Unité de recherche : Université Paris-Saclay, CNRS, Laboratoire interdisciplinaire des sciences du numérique, 91405, Orsay, France
Référent : Faculté des sciences d'Orsay

Thèse présentée et soutenue à Orsay, le 18 juin 2021, par

Nan JIANG

Composition du Jury :

Christophe JOSSERAND Directeur de Recherche, LadHyX, Ecole Polytechnique	Président
Stéphanie GIROUX-JULIEN Maître de Conférences, HDR, Université Claude Bernard Lyon 1	Rapporteuse & Examinatrice
Stéphane MIMOUNI Ingénieur, HDR, EDF R&D	Rapporteur & Examinateur
Hervé DUVAL Professeur, CentraleSupélec, Université Paris-Saclay	Examinateur
Patrick LE QUERE Directeur de Recherche, CNRS, LISN, Université Paris-Saclay	Examinateur

Direction de la thèse :

Bérengère PODVIN Chargée de Recherche, HDR, LISN, Université Paris-Saclay	Directrice de thèse
Etienne STUDER Ingénieur, CEA/DES/ISAS/DM2S	Co-encadrant

Thèse de doctorat

NNT : 2021UPAST063

“山重水复疑无路，柳暗花明又一村。”

——陆游《游山西村》[1]

[1] “After endless mountains and rivers that leave doubt whether there is a path out, suddenly one encounters the shade of a willow, bright flowers and a lovely village.” (Poem by Lu You, from the Southern Song Dynasty of China)

Remerciements

Cette thèse a été réalisée au Centre d'études de Saclay (DES/ISAS/DM2S/STMF/LATF) et au sein du Laboratoire Interdisciplinaire des Sciences du Numérique (LISN).

Je voudrais exprimer toute ma gratitude aux membres du jury : à Christophe Josserand pour m'avoir fait l'honneur de présider mon jury de thèse, à Stéphanie Giroux-Julien et à Stéphane Mimouni pour avoir accepté d'être rapporteurs de ce travail et à Hervé Duval et Patrick Le Quéré qui ont consenti à juger cette thèse.

Je tiens à remercier Etienne Studer pour m'avoir accueilli au CEA Saclay, pour son point de vue expérimental, pour ses enseignements et ses inspirations, pour m'avoir fait un bon exemple d'un chercheur avec une grande passion et pour son encouragement et son soutien surtout pendant la période difficile.

Je tiens à remercier Bérengère Podvin pour avoir dirigé cette thèse, pour son point de vue numéricien, pour ses enseignements et ses inspirations, pour sa patience et son appréciation constante des valeurs de ce travail et pour son soutien jusqu'à la fin.

Enfin j'adresse mes remerciements à ma famille qui m'a soutenu et à tous ceux qui m'ont apporté une aide, scientifique, technique, ou qui m'ont apporté leur amitié.

Contents

List of Figures

List of Tables

Chapter 1

Introduction

1.1 Motivation

During the course of a severe accident in a Pressurized Water Reactor (LOCA or Loss Of Coolant Accident), pressurization of the containment occurs and hydrogen can be produced by the reactor core oxidation and distributed in the containment vessel (FIG. 1.1). Vaporization of the primary circuit water leads to a peak in the pressure which is limited by heat transfer and condensation on the cold walls.

During accident transients, high-pressure cooling water leaves the primary circuit and enters the containment where it flashes into steam. This steam is then condensed on the containment vessel wall, with a strong dependence of the peak pressure and temperature in the containment on the environment conditions. These include in particular the amount of non-condensable gases present and the bulk steam flow induced convection effects.

Heat transfer after the accident is characterized by two stages:

- condensation and forced convection, due to the depressurization of the primary circuit, which is associated with strong atmospheric turbulence

- condensation and natural (or mixed) convection

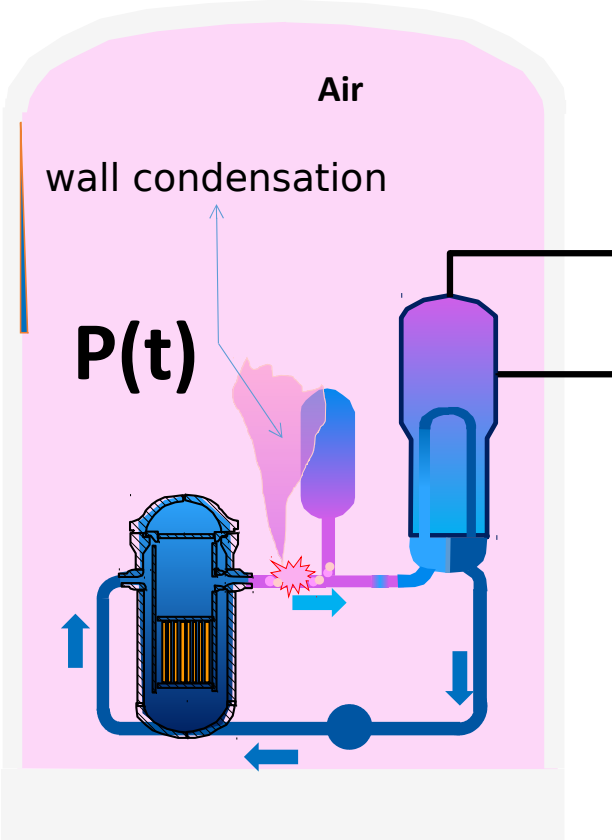

Figure 1.1: Reactor building

Correct prediction of the distribution of hydrogen is essential to assess flammability and detonation conditions in the containment. This distribution is influenced by convection as well as condensation effects. In particular, wall condensation induces a local reduction in the vapour concentration, which leads to a higher hydrogen concentration near the walls and therefore a higher detonation risk. Moreover, as detailed below, condensation is affected by the presence of non-condensable gases (air, hydrogen). Owing to the large volume of the reactor containment, accurate prediction of the heat transfer at the wall remains a challenge.

1.2 Experimental Correlations

The first codes used to compute heat transfer at the wall relied on simple dimensional correlations determined from experiments. Uchida [Uchida et al., 1965] provided the following expression for the heat transfer coefficient for steel:

$$h_{\text{Uchida}} = 380 \left(\frac{Y_{air}}{1 - Y_{air}} \right)^{-0.5} \tag{1.1}$$

where Y_{nc} represents the non-condensable mass fractions. Here the non-condensable gas is air.

Tagami [Tagami, 1965] proposed the following modification in forced convection:

- $t \leq t_p : h = 0.66 \left(\frac{E}{V t_p} \right)^{0.6} \sqrt{\frac{t}{t_p}} = h_{tag}(t)$
- $t = t_p : h = h_* = 0.66 \left(\frac{E}{V t_p} \right)^{0.6}$
- $t \geq t_p : h = h_* e^{\frac{t - t_p}{20}} + h_{Uchida} * \left(1 - e^{\frac{t - t_p}{20}} \right)$

where

- t is the current time
- t_p is the current time corresponding to the pressure peak
- E is the energy released through the break during depressurization
- V is the containment volume

Tagami also proposed the following expression for natural convection:

$$h_{Tagami} = 11.4 + 284 \left(\frac{1 - Y_{air}}{Y_{air}} \right) \tag{1.2}$$

It is generally found that the values given by theoretical correlations are lower than the empirical heat transfer measurements in natural convection. Green and Almenas (1996) [Green and Almenas, 1996] proposed three reasons for the under-prediction:

(i) Bulk velocities used in theoretical models are much lower than reality.

(ii) The presence of mist in the gas-vapour boundary layer under saturated conditions may increase the sensible heat transfer from the atmosphere to the walls.

(iii) Heat transfer processes are enhanced by film dynamics such as the presence of ripples, which are associated with higher turbulent levels.

Furthermore, as pointed out by Leduc [Leduc, 1995] and Peterson [Peterson, 1996], the correlations are dimensional and established for small geometries, which may limit their range of applicability in full-scale containment vessels. Finally, the correlations provide an average value for the exchange coefficient, and local concentrations are not available, which does not make accurate computation possible.

1.3 Condensation

The largest part of the heat transfer is due to condensation. Condensation can occur either as a film or as droplets (see FIG. 1.2). In our case, with the possible exception of horizontal surfaces, we only need to consider the case of film condensation. Film condensation takes place when the temperature of a vertical, impermeable, and wettable wall next to a gaseous medium saturated with vapour falls below saturation temperature. Owing to gravity, the liquid flows downwards. Mist can be present in the boundary layer. This leads to the creation of a two-phase region between the liquid film and the vapour region, where both droplets and vapour are present (FIG. 1.3). It is assumed that (i) the vapour temperature is equal to the saturation temperature, (ii) the temperature in the liquid region is

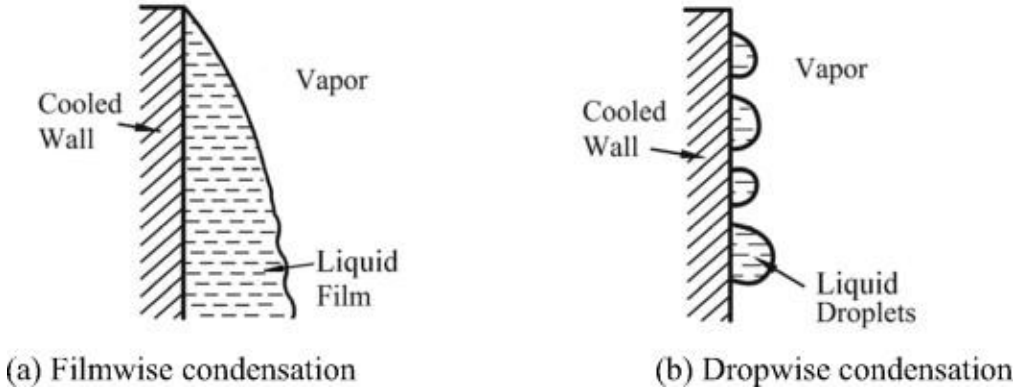

Figure 1.2: The two modes of wall condensation

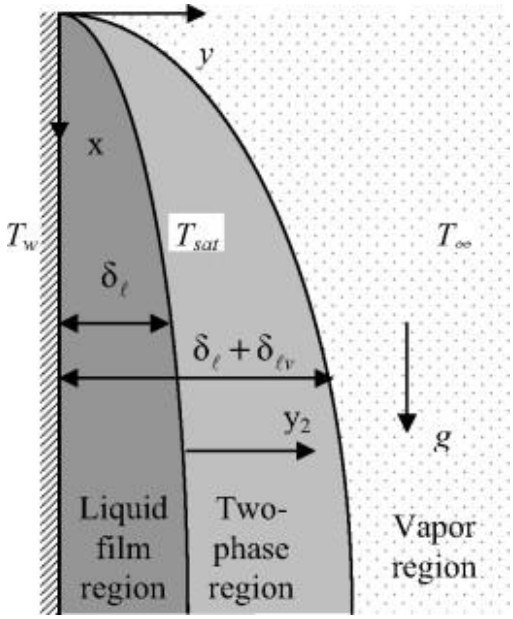

Figure 1.3: Transport Phenomena in Multiphase Systems

below saturation temperature, (iii) the temperature in the two-phase region is at saturation temperature.

We note that the presence of an non-condensable gas in the vapour leads to a strong thermal resistance which is higher than that due to droplets. A very little fraction of non-condensable gas can therefore lead to a strong increase in thermal resistance.

1.4 Film modeling

Film flow dynamics are expected to have an impact on the accurate prediction of the heat transfer coefficient. Nusselt [Nusselt, 1916] first derived a laminar film thickness based on the assumptions of viscous flow where no shear or wave motion exist at the liquid interface. His theory showed that the liquid film mass flow rate increases as a cubic power of film thickness. Following Nusselt's work, much theoretical and experimental research for the film thickness has been conducted and tabulated. Recently, Zadrazil et al. (2014) [Zadrazil et al., 2014]'s experimental study showed that falling film flows could be classified into different regimes depending on the length of wave subtract, wave length, the film thickness of wave, and the film thickness subtract. Typically, a vertical film flow always starts from droplets agglomeration, and gradually develops into laminar, then wavy, then turbulent film flow depending on length of the cooling plate. Transition from laminar to turbulent falling film flow can occur at a critical film Reynolds number of 1,600 - 1,800. Visual observations of the film in the COPAIN experiments [Bazin and Castelli, 2000] have shown that the film is a complex structure with very thin regions and flowing rivulets in between (see FIG. 2.4).

An approach for turbulent film flows is to use the diffusion layer model, a lumped approach for the film heat transfer rate estimation over the length of the heat transfer plate. With the presence of non-condensable gas, the diffusion layer model gives a useful approach to predict the condensation rate. Non-condensable gas accumulates at the liquid-vapour interface when the condensate liquid film forms near the cold wall (see FIG. 1.4). The condensate film and heat/mass transfer rates in gas/vapour mixtures are calculated separately. Under steady-state conditions, the heat fluxes on the film surface and on the cooling wall remain the same. The condensate heat transfer is driven by the temperature difference between the cooling wall and the interface ($T_i - T_w$). Both latent and sensible heat are transferred through the interface, and the gas/vapour mixture regions.

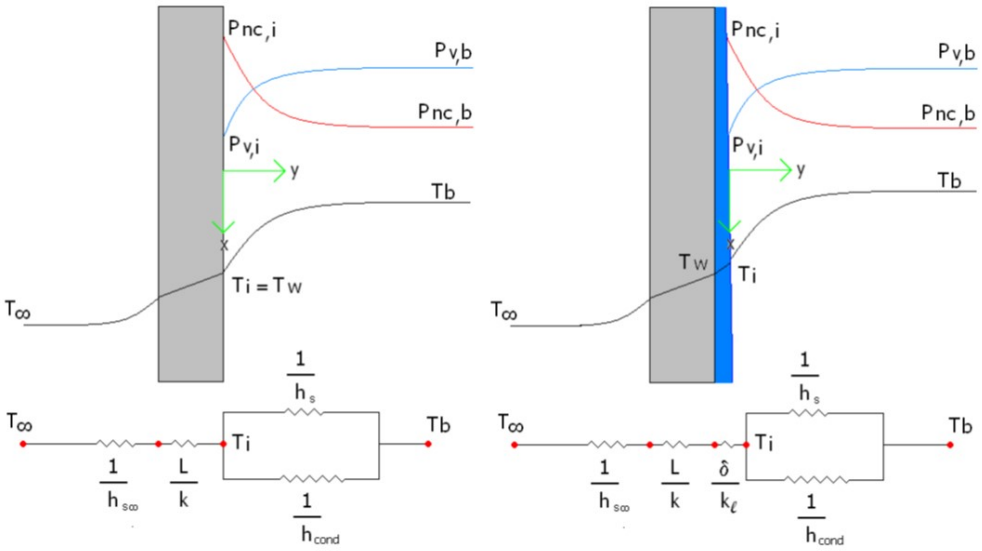

Figure 1.4: Filmwise condensation in vapour/non-condensable gases mixture [Bucci, 2009]

1.5 Turbulent flow

Due to convection effects, it is not generally possible to consider that the flow is laminar. We first give a brief description of the turbulent boundary layer and approaches used to model it.

1.5.1 Turbulent boundary layer without heat or mass transfer

The boundary layer is classically divided [Hinze, 1976] into two regions:

- an inner region, where the relevant scales depend on diffusion processes and wall transfers. In the case of a purely dynamic case, these scales consist of the kinematic viscosity $\nu = \mu/\rho$, where μ is the fluid viscosity and ρ the density and the friction velocity u_τ defined from the wall shear $\rho u_\tau^2 = \mu \frac{dU}{dy}|_{\text{wall}}$ where y is the wall distance. A length unit ν/u_τ can be defined. These units are referred to as wall units and labelled with a $+$ suffix.

- an outer region, where the relevant scales are external: in the case of a purely dynamic boundary layer, they consist of the velocity U_e and the boundary layer thickness δ, which can be defined as the height at which the flow reaches 99% of the external velocity U_e

- A matching layer can be defined over the two regions. In this region, called the inertial sublayer, the appropriate length scale is the wall distance y and the mean velocity U in this region is characterized by a logarithmic profile:

$$U/u_\tau = \frac{1}{\kappa} \ln y + C \tag{1.3}$$

  where κ is the Von Karman constant ($\kappa = 0.41$) and C is a constant ($C \sim 5.5$ in the case of a turbulent channel [Tennekes and Lumley, 1972]).

The classic picture of the boundary layer is modified when additional physics due to heat and/or mass transfer are present. More details will be given in the next chapter.

1.5.2 Turbulence models

As noted above, direct numerical simulation of phenomena in the turbulent regime over a realistic domain is not possible given the large spectrum of scales involved. Since the flow is in general turbulent, modelling of the turbulent fluxes is required.

Low-Reynolds turbulence models have gained popularity over high-Reynolds turbulence models with wall functions as they can be integrated down to the wall, so that they do not require to actually chose an arbitrary wall distance. However, extremely fine meshes are required near walls to ensure an appropriate representation of the strong gradients close to the wall and an accurate integration of the source terms associated with the low-Reynolds turbulence models in the viscous region (typically under $y_+ = 10$). As a result of

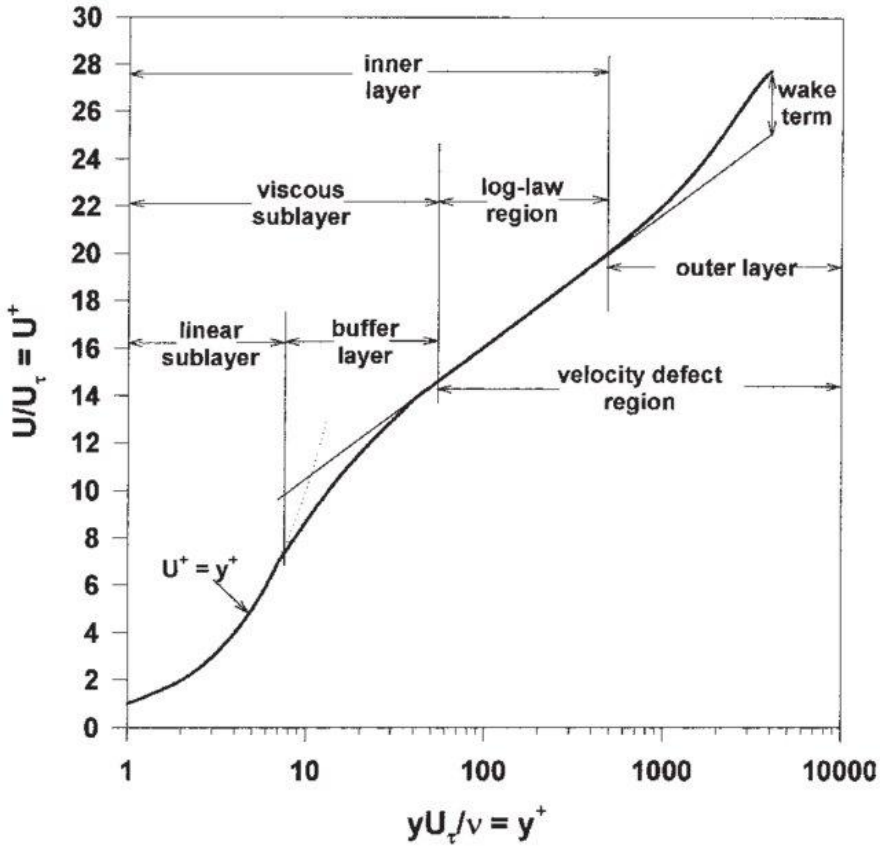

Figure 1.5: Turbulent boundary layer

this requirement, most of the computational resources are concentrated in the boundary layers, and the constraint on the mesh size induces limits for the computation.

An interesting alternative to low-Reynolds models is provided by wall functions to model the inner part of the boundary layers. It has been shown that traditional high-Reynolds turbulence models yields a faster convergence than for the low Reynolds case [Frazza et al., 2018]. However, wall functions can be difficult to manipulate, as their implementation depend on the definition of a wall distance, which is itself sensitive to the flow conditions such as the pressure gradient. [Kalitzin et al., 2005]. Traditional wall functions are based on the ”logarithmic-law” and thus require to be used around $y_+ = 30$. Below $y_+ = 20$ the ”logarithmic-law” is not verified. Wall functions need to be carefully implemented in order to obtain mesh convergence [Frazza et al., 2018].

1.5.3 Turbulence models and condensation

Mechanistic condensation modeling has been traditionally addressed through two different approaches: i) the solution of conservation equations in the boundary layer and ii) the application of the heat/mass transfer analogy. As detailed below, analysis of the full boundary layer equations can provide theoretical insight into the different physical phenomena but cannot result in practical calculations of the full scale spectrum of containment. In contrast, the analogy models based on correlations of mass transfer obtained by the Chilton - Colburn analogy [Bergman et al., 2006] can be easily implemented. Heat transfer process is controlled by the mass concentration gradient through the non-condensable layer, as the sum of sensible heat and latent heat flows. The models assume closure laws for heat transfer across the film and generally require that natural convection effects be neglected [Leduc, 1995], although extensions of the modeling approach have been given by [Kim and Corradini, 1990] for natural convection in the presence of a non-condensable gas.

Leduc [Leduc, 1995] provided an improvement of Kim and Corradini’s model and [Kim

and Corradini, 1990] gave an analytical form for wall functions that accounted for the wall suction associated with condensation. Agreement with experiments was observed: the heat transfer coefficient increased with the vapour fraction and the average velocity of the gas mixture.

In the course of this thesis we revisit Leduc's approach and examine the influence of additional physical phenomena on the characteristics of heat and mass transfer.

1.6 An overview of the coupling phenomena considered in this thesis

Our analysis throughout the manuscript is based on the conservation equations of mass, momentum, energy and species. We give a brief overview of the various physical phenomena that may be included in the analysis.

1.6.1 Natural convection

Temperature variations result in modifications of the fluid properties such as the viscosity, conductivity and density. As a simplifying assumption, it is possible in some cases to neglect these variations and to assume that the dynamics of the flow are essentially independent from the temperature. The temperature is therefore considered as a passive scalar that is advected and diffused by the flow, which corresponds to a situation of *forced convection.*

Conversely, in other cases, the relevant approximation is that of *free convection*, a situation in which the flow dynamics are entirely driven by the temperature variations, and in particular by the gravity-induced buoyancy force resulting from density variations. If

these variations are sufficiently small, the Boussinesq approximation provides a simplified framework in which the flow can be assumed to remain incompressible and density variations are only taken into account in the momentum equations. In the more general case however, the Boussinesq approximation fails and variations of the physical properties need to be taken into account in all conservation equations.

Many real-life cases correspond to a more complex situation of *mixed convection*, involving cross-coupling between velocity and temperature fluctuations. One typically defines relevant dimensionless parameters, such as the Richardson number that determines the relative influence of shear and buoyancy effects, in order to provide a model that will be complex enough to capture relevant physics, yet simple enough for useful and practical implementation.

1.6.2 Wall aspiration due to condensation

In the remainder of the thesis, following Leduc, as a first approximation we will model the film and the condensate as a wall with suction, i.e a wall-normal negative velocity. Wall suction influences the characteristics of the boundary layer as was shown early on by Tennekes [Tennekes and Lumley, 1972] (see FIG. 1.6). In particular the mean velocity is characterized by a new velocity scale that depends on the suction rate.

1.6.3 Soret effect

The mass diffusion flux J_i for each species k can be expressed with the Fick law

$$\mathbf{j}_k = -\rho D \boldsymbol{\nabla} Y_k \tag{1.4}$$

where D is a diffusion coefficient and Y is the mass fraction of the reference composition.

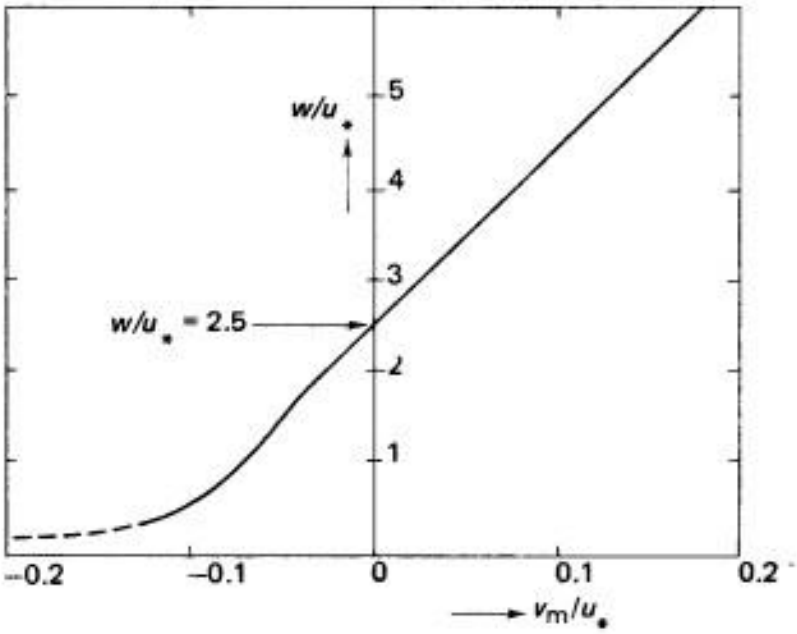

Figure 1.6: Turbulent boundary layer with aspiration; v_m is the aspiration velocity, u_τ the friction velocity and w the new velocity scale such that $U/w = \ln y + C$, where C is a constant [Tennekes and Lumley, 1972]

Thermo-diffusion, also known as the Soret effect, is a coupled process by which solutes are transported in a medium under the action of a thermal gradient. Although most solutes have positive coefficients indicating that they will diffuse down the thermal gradient (away from the heat source), a number have negative coefficients and may move up the gradient. A stationary temperature gradient in a liquid mixture induces a stationary concentration gradient through the Soret effect. The vapour mass flux is then

$$\mathbf{j}_v = -\rho D \boldsymbol{\nabla} Y_v - \alpha_D \rho D Y_v (1 - Y_v) \frac{1}{T} \boldsymbol{\nabla} T \tag{1.5}$$

where T is the temperature and α_D is the thermal diffusion ratio for vapour.

1.6.4 Dufour effect

Conversely, the Dufour effect represents the energy flux due to a mass concentration (chemical potential) gradient which results in a temperature change. The energy flux can

be expressed using the Fourier law

$$\mathbf{q} = -k\boldsymbol{\nabla}T \tag{1.6}$$

Taking into account the Dufour effect, the flux writes

$$\mathbf{q} = -k\boldsymbol{\nabla}T + q_D \tag{1.7}$$

with

$$\mathbf{q}_D = \alpha_D RT \frac{M}{M_a M_v}\mathbf{j}_v. \tag{1.8}$$

For binary liquid mixtures, the Dufour effect is usually considered negligible, whereas in binary gas mixtures the effect can be significant.

1.6.5 Species Interdiffusion

A third coupling effect appears in the energy flux owing to the interdiffusion of species, i.e the energy transfer associated with the fact the different species have different enthalpies. In the case of a binary mixture of air (a) and vapour (v), we have $\mathbf{j}_v + \mathbf{j}_a = \mathbf{0}$ and the interdiffusion flux writes

$$\mathbf{q}_I = (c_{p,v} - c_{p,a})T\mathbf{j}_v \tag{1.9}$$

where $\mathbf{j}_v$ is the total vapour flux (including the Soret effect).

In many studies these different coupling terms are omitted from the analysis without justification.

1.7 Organization of the thesis

The manuscript is organized as follows:

- After the rapid overview of the physical processes given in this chapter, a more detailed description of the state of the art will be given in Chapter 2.
- A model to describe coupled mass and heat transfer in the laminar case is presented and validated in Chapter 3.
- Low-Reynolds turbulence models are described in Chapter 4.
- Wall functions are derived in Chapter 5 based on the resolution of a system of 1-D ODEs.
- Chapter 6 presents the conclusion and perspectives.

Chapter 2

State-of-the-Art

In this chapter, we will first detail the equations governing the transport of steam in a mixture of non-condensable gases for filmwise condensation on a cold wall. Then, to solve these equations, we recall the assumptions usually made to simplify the problem. After setting-up the simplified system of equations, we give the different approaches followed in the literature to model the mass, heat and momentum fluxes in coherence with the spatial and temporal discretizations. We then add a review of the data available in the literature to validate these models. Finally, from this overview of the global problem, we present the work done in this thesis to improve the modeling of filmwise condensation in turbulent flow at high Reynolds number with wall function.

2.1 Balance equations and simplifications

The containment atmosphere is a mixture of gases of which only the steam is condensable under the conditions of temperature and pressure encountered in incidental or accidental situations in nuclear power reactors. Moreover, this steam coexists with non-condensable gases such as nitrogen and oxygen from the air, hydrogen etc. In our approach we con-

sider for the sake of simplicity only one non-condensable gas. The steam can therefore condense on a cold surface whose temperature is lower than the saturation temperature of the steam at its partial pressure in the volume. It thus disappears along the wall to form a liquid film. Dropwise condensation is not considered in this work. This phase change allows the transport of steam from the bulk to the wall. This transport of steam leads to a transport of non-condensable gases and because of the impermeable nature of the interface to these gases, there is an accumulation of these non-condensable gases close to the wall. Non condensable gases dissolution in the liquid film is also neglected. There is therefore a resistance to the steam flow, i.e. to mass and energy transfer. This resistance is supposed to be larger than the film resistance (at a sufficiently high content of non condensable gases). Consequently, the liquid film is neglected, the interface is located at the wall and the shear velocity at the liquid/gas interface is imposed equal to zero. The general transport equation of a gas species characterized by its mass fraction Y_v in a gas mixture is written:

$$\frac{\partial \rho Y_v}{\partial t} + \boldsymbol{\nabla} \cdot \rho Y_v \mathbf{U} = -\boldsymbol{\nabla} \cdot \mathbf{j}_v + S_v \tag{2.1}$$

The total mass flux of species v is thus decomposed into two terms: a convection or entrainment by the flow and a diffusive transport:

$$\dot{\mathbf{m}_v}'' = Y_v \rho \mathbf{U} + \mathbf{j}_v. \tag{2.2}$$

Different mechanisms act to create diffusive transport and this topic has been examined in detail in the thesis work of [Bucci, 2009]. This diffusive flux is divided into several terms involving the gradient of mass fractions of each chemical species (generalized mass diffusion), the temperature gradient (Soret or thermodiffusion effect) and the pressure gradient (barotropic effect).The last term is neglected in our application due to the size of the device. The simplification of considering the mixture of non-condensable gases as a single chemical species allows the mass flux of steam to be written as follows [Bird et al., 2006]:

$$\mathbf{j}_v = \rho D_{v,m} \boldsymbol{\nabla} Y_v + \alpha_D \rho Y_v \left(1 - Y_v\right) \frac{1}{T} \boldsymbol{\nabla} T \tag{2.3}$$

The first term is generally known as Fick's law and the second is called the thermodiffusive or Soret effect. $D_{v,m}$ stands for the diffusion coefficient of steam in the gaseous mixture and α_D represents the thermal diffusion ratio. This thermodiffusion effect is generally neglected in our problem without really providing any justification except that this term couples the diffusive flux with the energy equation and therefore neglecting it simplifies the problem. Recently, Bian et al. [Bian et al., 2019] have incorporated this effect in a numerical model of steam condensation and they showed that its effect can play a role in mass transfer in the case of huge content of non condensable gas or highly superheated air/steam mixture, i.e. large temperature differences.

With the previous assumptions, at the condensation interface the mass flux is zero for the non-condensable gases and therefore we deduce that the steam flux in the direction orthogonal to the interface is written:

$$\dot{m_{v,w}}'' = \frac{j_{v,w}}{1 - Y_{v,w}} = \frac{\rho D_{v,m} \, \boldsymbol{\nabla} Y_v|_w}{1 - Y_{v,w}} \tag{2.4}$$

In the models, the transfer at the wall will therefore be completely characterized by knowing the conditions at the interface and this flux under the assumption of non-condensable gas impermeability.

For the conservation of energy in condensation, the energy flux can be written in the form [Jiang and Studer, 2020]:

$$\mathbf{q} = -k \boldsymbol{\nabla} T + \left(c_{p,v} - c_{p,n.c.}\right) T \mathbf{j}_v + \alpha_D R T \frac{M}{M_{n.c.} M_v} \mathbf{j}_v \tag{2.5}$$

with the terms of the Fourier law, the interdiffusion term (see Appendix B) and the Dufour effect. In general, in filmwise condensation, the diffusive term of the Fourier law is the most

important. In a similar way to the Soret effect, keeping only this term has the advantage of not coupling the equations together and thus considerably simplifying the problem to solve.

Finally, momentum balance is very similar to classical compressible Navier-Stokes equations:

$$\frac{\partial}{\partial t}(\rho \mathbf{U}) + \boldsymbol{\nabla} \cdot (\rho \mathbf{U} \otimes \mathbf{U}) = -\boldsymbol{\nabla} P + \boldsymbol{\nabla} \cdot \tau + \rho \mathbf{g} \tag{2.6}$$

and, the multi-species gaseous mixture is only affecting the density ρ and the kinematic viscosity μ in the shear-stress tensor τ. In this equation, no new hypothesis are used.

2.2 Modeling of heat and mass transfer fluxes

2.2.1 General Approach

Historically, the thermal-hydraulic behavior of the containment has been studied with numerical tools of increasing complexity. Until the 1990's, the behavior was analyzed with mono-volume computer codes (Lumped Parameter codes or LP codes), thus with a simple mass and energy balance. In these tools, the wall condensation was taken into account by a global or empirical correlation such as the one of Uchida [Uchida et al., 1965] already mentioned. These correlations provide a global heat exchange coefficient h_{tot} in the empirical form:

$$h_{tot} = C \left(\frac{m_v}{m_{tot}} \right)^{\gamma} \tag{2.7}$$

where C and γ are constants fitted to experimental data. Then, the condensation rate is calculated by dividing the exchanged flux by the latent heat of phase change $H_{lat,w}$. This correlation was determined experimentally in an small enclosure. Then, these results are extrapolated to the scale of the containment. These correlations are widely used in industrial applications and many of them are implemented in computer codes. However,

they depend on the geometrical and experimental conditions and they should be only use in their range of application.

More recently, the containment was discretized into control volumes of a characteristic size of about ten meters and in these volumes mass and energy balances were performed. The exchange of mass and energy between the volumes is not done by writing a true momentum balance equation but by simplifying the problem using a Bernouilli type law. In these tools (TONUS [Benteboula and Dabbene, 2020] ASTEC [Chatelard et al., 2014], MELCOR [Yoo et al., 2018] ...), wall condensation is modeled by empirical correlations but also by correlations based on the analogy between heat and mass transfer [Ambrosini et al., 2006]. In this case, by analogy with Newton's law defining a heat transfer coefficient, we can define a mass transfer coefficient h_m by:

$$h_m = \frac{j_{v,w}}{Y_{v,w} - Y_{v,\infty}}. \tag{2.8}$$

The mass flow is then written:

$$\dot{m_{v,w}}'' = h_m \frac{Y_{v,w} - Y_{v,\infty}}{1 - Y_{v,w}} = h_m B_m \tag{2.9}$$

with B_m the driving force of the condensation. It can be shown that under the condition of equality of the mass and thermal diffusivities (i.e. a unitary Lewis number) the transport of heat or steam in an incompressible and laminar boundary layer are identical in the natural convection regime. Therefore, the correlations governing heat transfer, namely the Nusselt number Nu as a function of the Reynolds number Re, Grashof number Gr and Prandtl number Pr, can be used to calculate the Sherwood number $\mathrm{Sh} = h_m l / \rho D_{v,m}$ (l characteristic length and properties are calculated for so-called 'film' conditions) as a function of Reynolds, Grashof and Schmidt Sc numbers. The validity of this approach has been extended for high fluxes by taking into account the suction effect. The corrected

mass transfer coefficient is then written:

$$h_{m,suc} = h_m F = h_m \frac{B_m}{e^{B_m} - 1} = h_m \frac{\frac{\dot{m_{v,w}}''}{h_m}}{e^{\frac{\dot{m_{v,w}}''}{h_m}} - 1}. \tag{2.10}$$

Correction coefficients are also applied on the heat transfer [Kays, 1972] and on the friction coefficient [Ackermann, 1972]. An important work of validation of this approach has been done [Ambrosini et al., 2014] but the characteristic length l remains if the Sherwood number is not directly proportional to l. Only natural convection flows in which $Sh \approx Gr^{1/3}$ allow to avoid the length scale l.

2.2.2 Mean Flow models

Since the beginning of the 2000's, CFD or field simulation tools have been used to study the thermal-hydraulic behavior of the containment vessel with the resolution of the averaged Navier-Stokes equations of mass, energy and momentum balance as well as the possibility to refine the mesh in the vicinity of the wall. Thus, the previous correlations can be applied with significant variations of the characteristic length l orthogonal to the wall (which can be seen as the distance from the interface from which the gaseous mixture is considered to be infinite). A direct numerical simulation (DNS) at the scale of the containment of a nuclear power reactor is unlikely to be attainable despite the increasing power of modern calculators. Consequently, the alternative approach of solving Reynolds averaged Navier-Stokes equations is an attainable solution but it requires turbulence transport terms to be modeled.

First, according to Reynolds, the average mixture variables are given by a time average and a fluctuating term:

$$\phi = \overline{\phi} + \phi' \tag{2.11}$$

This averaging technique addresses incompressible flows having constant density. How-

ever, flows of interest in this dissertation have density variations induced by fluctuating species mass fraction and temperature. Favre has introduced a density weighted averaging procedure more suitable for our problem [Favre, 1958]. According to Favre averaging method, each transported quantity is decomposed into a mean value and a fluctuating one:

$$\phi = \widetilde{\phi} + \phi'' \tag{2.12}$$

where $\widetilde{\phi} = \overline{\rho\phi}/\overline{\rho}$ and $\overline{\rho\phi''} = 0$. If we consider the compressible averaged steam species balance equation for example, it writes:

$$\frac{\partial \overline{\rho}\widetilde{Y_v}}{\partial t} + \boldsymbol{\nabla} \cdot \left(\overline{\rho}\widetilde{Y_v}\widetilde{\mathbf{U}}\right) = -\boldsymbol{\nabla} \cdot \mathbf{j}_v - \boldsymbol{\nabla} \cdot \left(\overline{\rho}\widetilde{Y_v''\mathbf{U}'}\right) \tag{2.13}$$

where the right hand-side term is composed of molecular diffusion flux and the fluctuating contribution. This last term is modeled by the gradient-diffusion hypothesis consisting of assuming that the turbulent transport term is proportional to the mean mass fraction gradient:

$$\overline{\rho}\widetilde{Y_v''\mathbf{U}'} = -\overline{\rho}D_t\boldsymbol{\nabla}\widetilde{Y_v} \tag{2.14}$$

where the proportionality coefficient D_t is assumed to be proportional to the eddy viscosity ν_t through the turbulent Schmidt number Sc_t. Estimation of the mass transfer rate is possible on the basis of interface boundary conditions, provided that the local gradients are accurately solved. Consequently, the turbulence models used in the simulations must deal with this requirement and it depends mainly on the spatial discretization in the near-wall region.

2.2.3 Near-wall treatment

If the mesh can be locally refined, the turbulence model has to have low Reynolds number capabilities and the grid size has to reach a size located in the viscous layer where the

velocity profile is as linear as possible. As heat and mass transfer are equally important, the mesh size must also be such that the temperature and mass fraction profiles are linear. Generally, these conditions are expressed in a dimensionless form from the velocity scale u_{ref} and the dimensionless numbers of Prandtl (Pr) and Schmidt (Sc) leading to:

$$y^+ = \frac{y\,u_{\text{ref}}}{\nu} \approx 1,\ y^+\text{Pr} \approx 1 \text{ and } y^+\text{Sc} \approx 1 \tag{2.15}$$

Since low-Reynolds number effects are incorporated in the turbulence model and therefore the mesh by approaching the wall is refined, there is no need for a model for the mass, thermal and momentum fluxes. We can directly use the molecular contributions associated to impermeability constraints to derive boundary conditions. The resolution of the near-wall zones by these models makes it a good candidate for a scaling up to wall functions used with coarser grid (see next paragraph). One should not forget that the low Reynolds number behavior is obtained in these models by damping functions which allow to find the known asymptotic behavior for the different dynamic variables and that generally the thermal and the mass transport are not the main topic of the investigated problems. Chapter 3 gives some elements on this subject but this work cannot fully replace a direct numerical simulation like the one undertaken by Bahavar et al. [Bahavar and Wagner, 2020] but the use of such tools is outside the scope of this thesis.

At the length scale of a containment, a refined resolution of the boundary layer is often out-of-the-scope the used simulation tools. Consequently, coarser discretizations are applied in the near-wall region and the turbulence models stay in the high Reynolds number domain. The connection to the wall is then done with the use of wall functions connecting the variables in the near-wall mesh to the values on the wall. In order to describe this topic in detail, we must first recall some classical elements of wall turbulence modeling. Turbulent flows are affected by the presence of walls. Due to no-slip condition of the fluid at the wall, the presence of strong mean velocity gradients in the vicinity of the wall will produce turbulent kinetic energy.

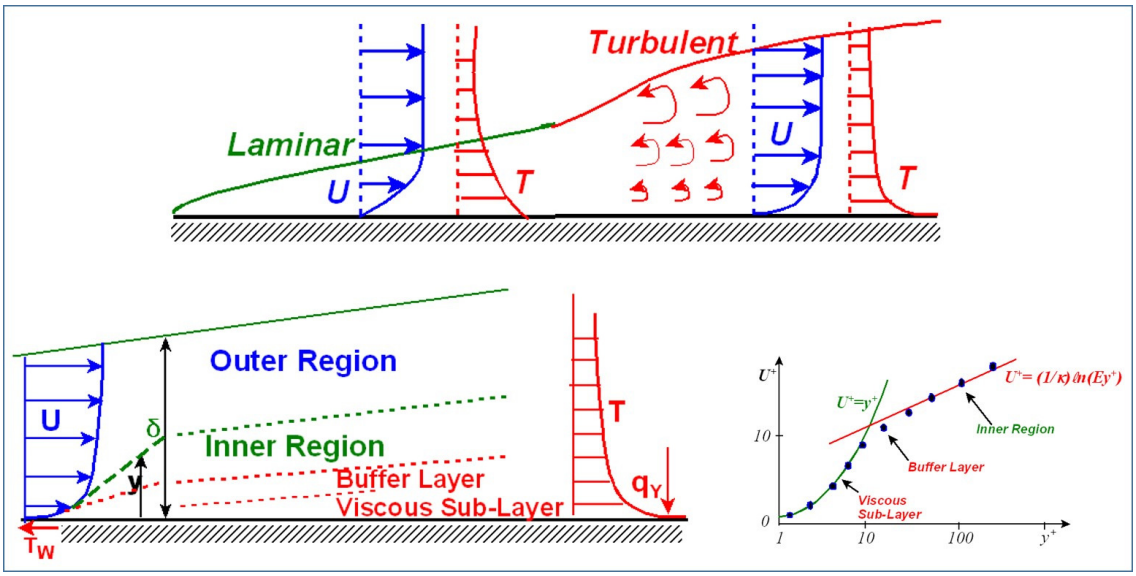

Figure 2.1: Example of turbulent boundary layer [Craft et al., 2001].

Conventionally, the near-wall region is divided into these different zones (FIG. 2.1 [Craft et al., 2001]):

- the region very close to the wall or **viscous or linear sublayer** where molecular phenomena play a dominant role in mass, energy and momentum transfers. Turbulent phenomena are neglected.

- the **inner region** furthest from the wall where, on the contrary, turbulent phenomena are dominant and molecular phenomena can be neglected. The mean velocity profile is characterized by a logarithmic law.

- an intermediate zone where it is difficult to discriminate between the two phenomena. This is generally called the **buffer zone**.

- the **outer zone** where the relevant scales are the external flow velocity U_e or U_∞ and the boundary layer thickness δ.

To characterise the thicknesses of the different inner zones, a length scale must be

used. For this purpose, the wall shear τ_w is expressed:

$$\tau_w = \mu \left. \frac{\partial U}{\partial y} \right|_w \tag{2.16}$$

and we express the friction velocity u_τ by:

$$u_\tau = \sqrt{\frac{\tau_w}{\rho}}. \tag{2.17}$$

The ratio between the viscosity of the fluid and this velocity scale provides a length scale generally referred to as the wall unit $\delta_w = \nu / u_\tau$. From this scale and in terms of thickness for the different inner zones, Pope [Pope, 2000] mentions for an isothermal channel flow that:

- the viscous sublayer extends to $y^+ = y/\delta_w \approx 5$;
- the buffer zone is between $y^+ \approx 5$ and $y^+ \approx 30$;
- the logarithmic zone covers from $y^+ \approx 30$ to $y/\delta \approx 0.3$ with the thickness of the boundary layer δ defined from its point of origin situated in $x = 0$ by $\delta(x) \approx 0.37x/\left(\mathrm{Re}_x\right)^{1/5}$ [Kays, 1972] where $\mathrm{Re}_x = U_e x/\nu$ with U_e the external flow velocity;
- the outer zone is located beyond $y/\delta \approx 0.3$.

In a numerical simulation, the wall function approach avoids the use of a fine mesh in the vicinity of the wall in order to capture the strong gradients which take place there. In the historical approach introduced in 1974 by Launder and Spalding [Launder and Spalding, 1974], the reference scale for the velocities is u_τ and for lengths δ_w.

If we now write the momentum balance for a steady wall flow neglecting buoyancy, pressure gradient and suction or blowing we get:

$$\frac{\mathrm{d}}{\mathrm{d}y}\left[\left(\nu + \nu_t\right)\frac{\mathrm{d}U}{\mathrm{d}y}\right] = 0 \tag{2.18}$$

which is first integrated and written in dimensionless form:

$$\left(1+\nu_t^+\right)\frac{\mathrm{d}U^+}{\mathrm{d}y^+}=1 \tag{2.19}$$

with $U^+ = U/u_\tau$, $y^+ = y/\delta_w$ et $\nu_t^+ = \nu_t/\nu$.

Then, the classical method of resolution consists in separating the boundary layer into different zones. Close to the wall in the zone called 'viscous sub-layer', the turbulent effects are negligible $\nu_t \approx 0$ and the balance is reduced to:

$$\frac{\mathrm{d}U^+}{\mathrm{d}y^+}=1 \tag{2.20}$$

giving a linear profile $U^+ = y^+$ for the scaled velocity as a function of the scaled distance. Generally, this viscous sublayer is assumed to extend to $y^+ = 5$ in an incompressible, isothermal flow without longitudinal pressure gradient nor suction or blowing.

Far from the wall, molecular effects are negligible and to solve the equation (2.18) it is necessary to introduce a model for the eddy viscosity ν_t. The simplest model is a model of mixing length l_m proposed by Prandtl in 1908 by analogy with the molecular viscosity and the mean free path for a perfect gas in the kinetic theory of gases, for which, the viscosity is:

$$\nu_t = l_m^2\frac{\mathrm{d}U}{\mathrm{d}y}. \tag{2.21}$$

Durbin [Durbin and Petterson Reif, 2001] recalls that this analogy with the kinetic theory of gases has no basis in the very nature of the phenomena which are not comparable in the averaging process.

For flows in the vicinity of a wall, this mixing length, i.e. the coherence length for the transfer of momentum in a turbulent flow, is proportional to the distance to the wall $l_m = \kappa y$ with $\kappa \approx 0.41$ the Von Karman constant. Durbin adds here that this linear dependence is a priori valid only for the overlap zone between the logarithmic zone and the outer layer.

The dimensionless momentum balance then takes the form:

$$\kappa^2 \left(y^+\right)^2 \left(\frac{\mathrm{d}U^+}{\mathrm{d}y^+}\right)^2 = 1 \tag{2.22}$$

Finally, by integrating the equation (2.22) twice, we obtain the expression of the so-called 'logarithmic' law introduced earlier:

$$U^+ = \frac{1}{\kappa} \ln\left(y^+\right) + C \tag{2.23}$$

The value of the integration constant C depends on the location of the connection between the two boundary layer zones. Generally, the value given is close to 5, corresponding to a connection in the vicinity of $y^+ = 10$ (FIG. 2.2).

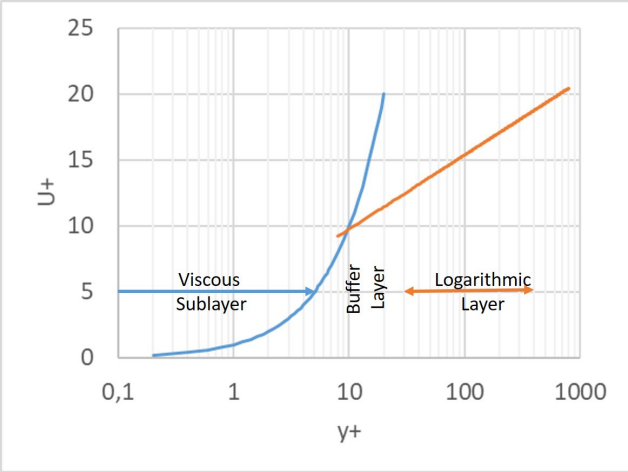

Figure 2.2: Wall function for an incompressible, isothermal flow with no pressure gradient.

For the mixing length, the models were then enriched. First of all, Van-Driest [Van Driest, 1956] proposed a model taking into account the damping due to the presence of the wall and the viscosity in order to have a smooth transition in the buffer layer. It takes the form of an exponential multiplying the original model of Prandtl:

$$l_m = \kappa y \left(1 - e^{-y^+/A^+}\right) \tag{2.24}$$

where $A^+ = 26$ is determined by the C constant of the logarithmic layer.

Finally, in the presence of suction, Cebeci [Cebeci, 1970] extended Van-Driest's work to the case of the presence of longitudinal pressure gradients and mass transfer. He came up with an expression of the form:

$$A^+ = 26 \left(-\frac{p^+}{V_w^+} \left[\exp\left(11.8 V_w^+\right) - 1 \right] + \exp\left(11.8 V_w^+\right) \right)^{-1/2} \tag{2.25}$$

with p^+ the acceleration parameter defined by $p^+ = -\frac{\mathrm{d}P}{\mathrm{d}x}\frac{\nu}{\rho u_\tau^3}$ and V_w^+ the wall transfer parameter defined by $V_w^+ = V_{wall}/u_\tau$. If we restrict ourselves to a boundary layer without acceleration, the effect of the suction at the wall increases A^+ which has the consequence of damping the Prandtl mixing length further away from the wall and thus thickening the viscous sublayer.

Additional improvements of the original Van-Driest model have been published in the literature and the most advanced model to take into account stress variation due to e.g. longitudinal pressure gradients, thermal effects or gas injection is written as [Patankar, 1967]:

$$l_m = \kappa y \left(1 - e^{-\frac{y^+}{A^+}\sqrt{\frac{\tau^+}{\rho^+}}} \right) \tag{2.26}$$

where $\tau^+ = \tau/\tau_w$ and $\rho^+ = \rho/\rho_w$.

For a flow where the temperature is important (exchange of a hot fluid with a cold wall or vice versa), it is also necessary to consider a wall function for the temperature because, here again, the gradients close to the wall are intense and therefore require a fine mesh to be captured by the numerical model. We proceed in the same way as above. In the absence of blowing or suction and species interdiffusion, the heat balance in the vicinity of the wall is written:

$$\frac{\mathrm{d}}{\mathrm{d}y}\left[\left(\alpha + \frac{\nu_t}{\mathrm{Pr}_t} \right) \frac{\mathrm{d}T}{\mathrm{d}y} \right] = 0 \tag{2.27}$$

which is integrated a first time in:

$$\left[\left(\alpha + \frac{\nu_t}{\mathrm{Pr}_t}\right)\frac{\mathrm{d}T}{\mathrm{d}y}\right] = \frac{\Phi_w}{\rho C_p} \tag{2.28}$$

and written in dimensionless form:

$$\frac{\partial \theta^+}{\partial y^+} = \frac{\mathrm{Pr}}{1 + \nu_t^+ \dfrac{\mathrm{Pr}}{\mathrm{Pr}_t}} \tag{2.29}$$

with $\theta^+ = (T - T_w)/T^*$, $T^* = \Phi_w/\rho C_p u_\tau$, Pr is the Prandtl number and Pr_t its turbulent analogue. As much as the former depends on the properties of the gas, the latter depends mainly on the flow.

To solve, we proceed in the same way as for the conservation of momentum, defining two more zones. In the viscous sub-layer, the resolution gives:

$$\theta^+ = y^+ \mathrm{Pr} \tag{2.30}$$

and in the area where turbulent transfers are dominant by introducing a mixing length $\nu_t^+ = \kappa y^+$:

$$\theta^+ = \frac{\mathrm{Pr}_t}{\kappa} \ln\left(y^+\right) + C_T \tag{2.31}$$

with the constant C_T to be determined according to the position of the connection between the two zones.

Finally, for the mass transfer, the calculation is again the same except that the Prandtl number is replaced by the Schmidt number $\mathrm{Sc} = \nu/D$ and θ^+ by Y^+ defined by $Y^+ = (Y - Y_w)/Y^*$ with $Y^* = \dot{m}''/\rho u_\tau$.

The wall functions we have just introduced for the three solved transport equations have been the subject of improvement to achieve greater generality. The first idea to improve the wall functions was proposed by Spalding (see [Launder and Spalding, 1974]).

He proposed to replace the velocity scale u_τ by $\sqrt{k}$ following his idea that for some flows, the wall shear disappears as for example in case of stagnant zone (impingement flow), separation zone or reattachment zone. Based on the logarithmic law, the wall shear stress can be expressed:

$$\tau_w/\rho = \left[\frac{\kappa U}{\ln\left[y\sqrt{\tau_w/\rho}\right] + C}\right]^2 \tag{2.32}$$

On the other hand, the wall shear stress is expressed by:

$$-\frac{\tau_w}{\rho} = \nu_t \frac{dU}{dy}. \tag{2.33}$$

By re-injecting the logarithmic law, we arrive at an expression for the eddy viscosity:

$$\nu_t = \kappa y \sqrt{\frac{\tau_w}{\rho}} \tag{2.34}$$

so if $\tau_w \longrightarrow 0$ then $\nu_t \longrightarrow 0$ which poses a problem in the attachment or impact zones. If we now use the value of the turbulent kinetic energy at the end of the viscous sublayer (subscript vi) as a scale for the velocity, we obtain by the same argument:

$$\nu_t = \kappa y_{vi} \sqrt{k_{vi}} \tag{2.35}$$

The problem remains the determination of the quantities at the end of the viscous sublayer from those in the center of the simulation grid point. In general, for the sake of simplicity, we assume that the two values are equal. Thus, the eddy viscosity is not zero if the wall shear stress tends towards zero.

This new scale is used by many CFD tools as a characteristic scale. For example, the standard wall function of the FLUENT code [ANSYS, Inc., 2013] where the wall length scale is $\nu/C_\mu^{1/4}k^{1/2}$. Other proposals exist, in particular that of Chieng and Launder. However, these models are often considered as not being completely independent of the mesh size in the near wall.

For his own part, Iacovides details a method for quantifying the weaknesses of the logarithmic law. He starts from the conservation of momentum in a pipe of radius R, thus for an internal flow, which is expressed by:

$$\frac{1}{r}\frac{\partial}{\partial r}\left[\mu\frac{\partial U}{\partial r}-\rho\overline{U'V'}\right]\approx\frac{1}{r}\frac{\partial\tau}{\partial r}\approx-\frac{\partial P}{\partial x} \tag{2.36}$$

This value is constant and therefore, from the boundary conditions, the solution is written:

$$\tau=\tau_w\frac{r}{R}=\tau_w\frac{R-y}{R} \tag{2.37}$$

If the Reynolds number of the flow $\mathrm{Re}=U_eD/\nu$ is large, the boundary layer is thin. There is no modification of the shear stress τ in this layer, the logarithmic law is valid. If, on the other hand, this Reynolds number is small, the logarithmic law is deviated from and the reduction of the shear stress in the boundary layer becomes more important. It is possible to determine an order of magnitude of the decrease of this shear stress leading to a deviation from the logarithmic law. By introducing $\tau^+=\tau/\tau_w$ and y^+, the decay of the dimensionless shear stress can be expressed as:

$$\frac{d\tau^+}{dy^+}=-\frac{2}{\mathrm{Re}}\left[\frac{\tau_w}{\rho U_e^2}\right]^{-0.5}. \tag{2.38}$$

By introducing Blasius' empirical law for wall friction:

$$\frac{\tau_w}{\rho U_D^2}=0.04\mathrm{Re}^{-1/4} \tag{2.39}$$

we finally obtain:

$$\frac{d\tau^+}{dy^+}=-10\mathrm{Re}^{-7/8}. \tag{2.40}$$

If we now assume that for $\mathrm{Re}>10000$ the logarithmic law starts to be valid, we conclude that the critical decay is of the order of -0.003. The author then analyses the phenomena

that can lead to these decay values, such as the acceleration of the flow:

$$\frac{d\tau^+}{dy^+} = \frac{\nu}{\rho u_\tau^3}\frac{dP}{dx}, \tag{2.41}$$

an intense heat exchange which will decrease the density in the near wall and thus cause an acceleration, the suction which results in:

$$\frac{d\tau^+}{dy^+} = V_w^+\frac{dU^+}{dy^+} \tag{2.42}$$

and finally, natural convection which also creates a local acceleration. All these phenomena can be of sufficient intensity to affect the logarithmic law. It can therefore be seen that this logarithmic zone is not universal and it is therefore important to improve the wall functions by considering alternatives to this law.

In this improvement, the aim is to ensure a more relevant wall connection at a lower cost than the low Reynolds number turbulent model. Two strategies have generally been followed by researchers on this subject: either a better description of the analytical law on the different layers and in particular the transition zone between the viscous sub-layer and the logarithmic zone, or a numerical resolution of local balance equations.

In the first category, we can cite a model entitled “Enhanced wall functions” implemented in the ANSYS/FLUENT code [ANSYS, Inc., 2013]. This is a mixing function between the laminar and turbulent zones of the type used by Kader [Kader, 1981]:

$$U^+ = e^{\Gamma}U_{lam}^+ + e^{1/\Gamma}U_{turb}^+ \tag{2.43}$$

with the function Γ defined by:

$$\Gamma = -0.01\left(y^+\right)^4 / \left(1 + 5y^+\right). \tag{2.44}$$

Deriving with respect to y^+, we obtain:

$$\frac{dU^+}{dy^+} = e^{\Gamma}\frac{dU^+_{lam}}{dy^+} + e^{1/\Gamma}\frac{dU^+_{turb}}{dy^+}. \tag{2.45}$$

The two derivatives are expressed as:

$$\frac{dU^+_{lam}}{dy^+} = 1 + \alpha y^+ = 1 + \frac{\mu}{\rho\left(U^+\right)^3}.\frac{dP}{dx}y^+ \tag{2.46}$$

and

$$\frac{dU^+_{turb}}{dy^+} = \frac{1}{\kappa y^+}\sqrt{\left[S\left(1 - \beta U^+ - \gamma\left(U^+\right)^2\right)\right]} \tag{2.47}$$

with $S = 1 + \alpha y^+$ if $y^+ < 60$ otherwise $S = 1 + 60\alpha$, $\beta = \sigma_t \dot{q}_w / \rho C_p u_\tau T_w$ and $\gamma = \sigma_t \left(u_\tau\right)^2 / 2C_p T_w$ two thermal coefficients (FIG. 2.3) For this model, the FLUENT user guide mentions to refine the model to $y^+ \approx 1$ with at least 10 meshes in the area up to $\mathrm{Re}_y = 200$ (see definition in EQ. 2.48).

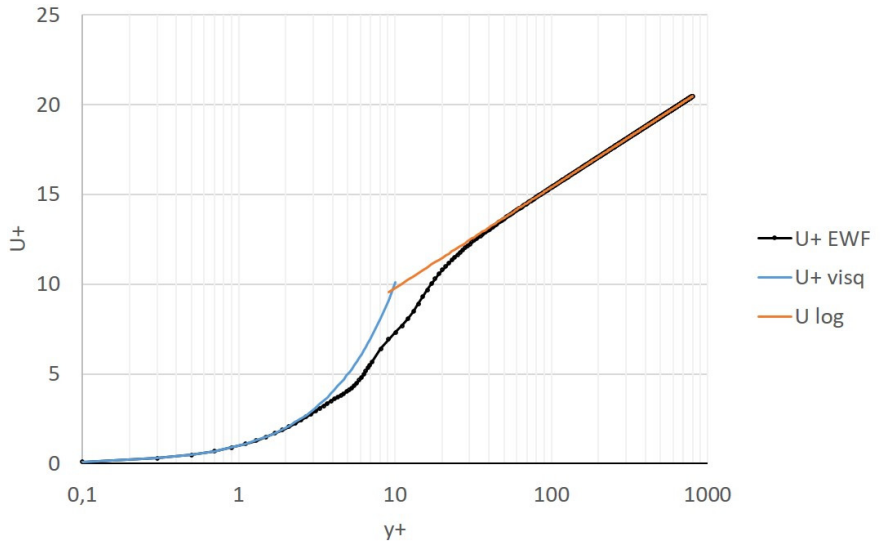

Figure 2.3: Example of a wall function including the buffer zone for an incompressible, isothermal flow without pressure gradient.

In the same kind of approach, Kalitzin et al. [Kalitzin et al., 2005] find that if the function $\nu_t^+ = \nu_t/\nu$ is known then the dimensionless momentum balance (equation 2.19) can be integrated and provide a law for $U^+\left(y^+\right)$. By expressing the Reynolds number for the grid

point g in the vicinity of the wall $\mathrm{Re}_y = y_g U_g/\nu = y_g^+ U^+\left(y_g^+\right) = \mathrm{F}\left(y_g^+\right)$ and inverting this law, we obtain directly the friction velocity $u_\tau = \nu/y_g \mathrm{F}^{-1}\left(y_g^+\right)$. Thus, tabulating this inverse function for the different turbulence models allows to directly obtain the friction velocity required for all boundary conditions. The authors even extend this approach with tables to classical one or two equations turbulence models.

In the second category, the ANSYS/FLUENT "enhanced wall treatment" model, firstly proposes to define a Reynolds number taking into account the distance y to the wall with the velocity scale corresponding to $\sqrt{k}$.

$$\mathrm{Re}_y = \frac{\rho y \sqrt{k}}{\mu} \tag{2.48}$$

If this number is greater than a threshold value, usually 200, a k-ε turbulence model for high Reynolds numbers is used. Otherwise, a single-equation k-l transport model is used. The length scale for viscosity is defined by:

$$l_\mu = y\kappa C_\mu^{-0.75}\left(1 - \exp\left(-\mathrm{Re}_y/70\right)\right) \tag{2.49}$$

and the viscosity in the near wall zone is then written from k:

$$\mu_{t,2} = \rho C_\mu l_\mu \sqrt{k}. \tag{2.50}$$

To smooth the transition between models, the FLUENT code uses the hyperbolic tangent function to define an effective turbulent viscosity:

$$\mu_{t,eff} = \Phi \mu_{t,k\varepsilon} + (1 - \Phi)\,\mu_{t,2} \tag{2.51}$$

with the mixing function Φ defined by:

$$\Phi = \frac{1}{2}\left(1 + \tanh\left(\frac{\mathrm{Re}_y - 200}{Z}\right)\right) \tag{2.52}$$

with $Z = 200a/\tanh(0.98)$ and a being 5 to 20%. Finally, the turbulent dissipation is defined near the wall by:

$$\varepsilon_2 = k^{3/2}/l_\varepsilon \tag{2.53}$$

with a length scale l_ε defined as for viscosity except that the value of 70 is replaced by $2\kappa C_\mu^{-0.75} \approx 4.9$. Then, between the two models, the same mixing function Φ is used.

In the early 2000s, the University of Manchester in England launched an ambitious research project with the objective of improving the wall functions in industrial CFD tools to deal with complex turbulent flows. Two lines of research were pursued: the first based on an analytical approach UMIST-A and the second on a numerical sub-mesh approach UMIST-N. We only detail the first one in this dissertation.

The initial idea comes from Gerasimov's work in 2003 [Gerasimov, 2003]. The momentum balance equation to be solved is divided into two terms:

$$\frac{\partial}{\partial y}\left((\mu + \mu_t)\frac{\partial U}{\partial y}\right) = -\frac{dP}{dx} + C_u + G_u \tag{2.54}$$

where C_u represents the convection term and G_u the buoyancy. Then, if we suppose that the right-hand side member is estimated at the center of the mesh in the near wall (in g), it becomes locally a constant noted A_g. And, if we suppose a variation of the turbulent viscosity μ_t or ν_t on this mesh, we can then integrate analytically this equation.

If we assume for example in a two-layer hypothesis that the eddy viscosity is given by:

$$\nu_t = 0 \tag{2.55}$$

if $y < y_v$ and:

$$\nu_t = C_\mu C_l \nu \left[y^+ - y_v^+\right] = \kappa\nu \left[y^+ - y_v^+\right] \tag{2.56}$$

otherwise. For the latter case, there are various possibilities for expressing this turbulent viscosity profile and we can cite, for example, the work of Cabot and Moin [Cabot and Moin, 2000] giving:

$$\nu_t = \nu\kappa y^+ \left(1 - \exp\left(-\frac{y^+}{A^+}\right)\right)^2 \tag{2.57}$$

with $A^+ \approx 26$ the Van-Driest coefficient, or the work of Duprat et al [Duprat et al., 2011]:

$$\nu_t = \nu\kappa y^+ \left(\alpha + y^+ (1-\alpha)^{3/2}\right)^\beta \left(1 - \exp\left(-\frac{y^+}{(1 + A^+\alpha^3)}\right)\right)^2. \tag{2.58}$$

With this profile, the velocity profile $U(y)$ in both zones can then be solved and expressed. For the viscous sub-layer, the momentum equation is written as:

$$\frac{\partial}{\partial y}\left(\mu \frac{\partial U}{\partial y}\right) = A_g \tag{2.59}$$

and outside:

$$\frac{\partial}{\partial y}\left(\mu \left(1 + C_\mu C_l \left[y^+ - y_v^+\right]\right) \frac{\partial U}{\partial y}\right) = A_g \tag{2.60}$$

The calculation using y_v^+ and y_e^+ gives us:

- for the zone $0 < y^+ < y_v^+$:

$$U^+\left(y^+\right) = C_u \frac{\left(y^+\right)^2}{2} + B_u y^+ \tag{2.61}$$

- and outside $y_v^+ < y^+ < y_e^+$:

$$U^+\left(y^+\right) = \frac{C_u}{\alpha}\left(y^+ - y_v^+\right) + y_v^+\left(B_u - \frac{C_u y_v^+}{2}\right) + \left[\frac{B_u}{\alpha} - \frac{C_u}{\alpha^2} + \frac{y_v^+ C_u}{\alpha}\right] \ln\left(1 + \alpha\left(y^+ - y_v^+\right)\right) \tag{2.62}$$

with $C_u = A_g \nu^2/\mu$ and

$$B_u = \frac{U_e^+ - C_u \left(y_v^+\right)^2/2 - C_u/\alpha \left(y_e^+ - y_v^+\right) + C_u/\alpha^2 \ln\left(1 + \alpha\left(y_e^+ - y_v^+\right)\right)}{\frac{1}{\alpha}\ln\left(1 + \alpha\left(y_e^+ - y_v^+\right)\right) + y_v^+}. \tag{2.63}$$

From this velocity profile, we can determine the wall shear stress τ_w and calculate the integrated turbulent kinetic energy production term on the near wall mesh:

$$\bar{P_k} = \frac{1}{y_e}\int_0^{y_e} \mu_t \left[\frac{\partial U}{\partial y}\right]^2 dy \tag{2.64}$$

For the ε dissipation, we introduce a mixing length model and we obtain in the mesh:

$$\varepsilon = \frac{k_g^{3/2}}{C_l y} \tag{2.65}$$

This profile is maintained until a distance y_d from which the dissipation is constant and equal to:

$$\varepsilon = \frac{2\nu k_g}{y_d^2} \tag{2.66}$$

From these data, y_d can be determined and $y_d^+ = 5.1$ is found, i.e. a sub-layer of lesser thickness than y_v.

Craft and Iacovides [Craft et al., 2002b] detail special cases to account for acceleration, variation in wall properties, the effect of large Prandtl numbers, the impact of roughness [Suga et al., 2006]. If, for example, we are interested in the effect of buoyancy, the coupling can be treated in different ways: either analytically by expressing the buoyancy term from the analytical solutions of temperature and/or concentration from the conservation of energy or species transport, or in an integrated way by adding the contribution of buoyancy averaged over the last mesh as for example by assuming a temperature effect according to the Boussinesq hypothesis:

$$F_g = \frac{1}{y_e}\int_{y=0}^{y=y_e} \rho_{ref} g_x \beta \left(T - T_{ref}\right) dy. \tag{2.67}$$

In the previous analysis, the conservation of momentum equation is integrated twice to obtain an analytical solution. More recently, Utyuzhnikov [Utyuzhnikov, 2006] proposed to integrate a first time to get :

$$\tau_w = (\mu + \mu_t) \frac{dU}{dy} - A_g y \tag{2.68}$$

from which we express:

$$\frac{dU}{dy} = \frac{\tau_w}{\mu^*(y)} + \frac{A_g y}{\mu^*(y)} \tag{2.69}$$

which is then integrated to obtain:

$$U(y) - U(0) = \tau_w \int_0^y \frac{d\xi}{\mu^*(\xi)} + A_g \int_0^y \frac{\xi}{\mu^*(\xi)} d\xi \tag{2.70}$$

The idea then is to express the last two equations at a particular well-chosen point, i.e. the centre of the last mesh (the g point) and to combine the two equations into a single one in order to eliminate τ_w as:

$$U(y_g) - U(0) = \left.\frac{dU}{dy}\right|_g \int_0^{y_g} \frac{\mu + \mu_t(y_g)}{\mu + \mu_t(\xi)} d\xi + A_g \int_0^{y_g} \frac{\xi - y_g}{\mu + \mu_t(\xi)} d\xi. \tag{2.71}$$

If one has an analytical form of the eddy viscosity profile $\mu_t(y)$, one transfers the wall problem to an algebraic form relating the variable and its gradient at the center of the mesh. This type of condition is a mixture of Dirichlet and Neumann boundary conditions known as the mixed Robin condition. This work can easily be extended to the case where A_g depends on y and can be applied to the different phenomena considered by Craft et al. Finally, from the conditions in g, it is then possible to calculate the wall shear stress using equation (2.68).

2.2.4 Near-wall treatment in case of filmwise condensation of steam in steam/non condensable gases mixture

In filmwise condensation, the wall functions were studied in detail by Leduc in 1995 [Leduc, 1995]. We briefly recall the reasoning, the assumptions and the equations obtained. In his work, in addition to using a Prandtl mixing length, Leduc makes the following assumptions:

- density is supposed to have small variations (Boussinesq approximation);
- species interdiffusion in the conservation of energy is neglected;
- buoyancy and longitudinal pressure gradient are neglected.

In the general case with transpiration, Leduc starts from the expression of the shear stress τ in the presence of the liquid/gas interface velocity U_i:

$$\tau = \rho u_\tau^2 \left[1 + V_w^+ \left(U^+ - U_i^+\right)\right] \tag{2.72}$$

if the liquid film shear velocity is neglected, it writes:

$$\tau = \rho u_\tau^2 \left[1 + V_w^+ U^+\right] \tag{2.73}$$

Then, Leduc introduces the Prandtl mixing length model:

$$\tau = \rho \overline{U'V'} = \rho l_m^2 \left(\frac{\partial U}{\partial y}\right)^2 = \rho \kappa^2 y^2 \left(\frac{\partial U}{\partial y}\right)^2 \tag{2.74}$$

And in dimensionless form:

$$\frac{dU^+}{dy^+} + \kappa^2 y^{+2} \left(\frac{dU^+}{dy^+}\right)^2 = 1 + V_w^+ U^+ \tag{2.75}$$

Then, he integrates this equation over the thickness of the viscous sublayer neglecting

turbulence (between 0 and $y_v^+ = 10.8$) and obtains a first equation:

$$\frac{1}{V_w^+} \ln\left(1 + V_w^+ U^+\right) = y^+ \tag{2.76}$$

Then, integration over the inertial zone (between y_v^+ and y^+) provides a second equation:

$$\int_{y_v^+}^{y^+} \frac{dU^+}{\sqrt{1 + V_w^+ U^+}} = \frac{1}{\kappa} \ln\left(\frac{y^+}{y_v^+}\right) \tag{2.77}$$

Combining these two equations, he expresses U^+ as a function of y^+ by:

$$U^+ = \frac{1}{V_w^+} \left[\left(\frac{V_w^+}{2\kappa} \ln\left(\frac{y^+}{10.8}\right) + \exp\left(\frac{10.8 V_w^+}{2}\right) \right)^2 - 1 \right] \tag{2.78}$$

with the parameter V_w^+. For the temperature, Leduc obtains in the same way:

$$T^+ = \frac{1}{V_w^+} \left[\left(\frac{V_w^+}{2\kappa} \ln\left(\frac{y^+}{10.8}\right) \exp\left(-\frac{10.8 V_w^+}{2}\right) + 1 \right)^{2\mathrm{Pr}_t} \exp\left(13.2 \mathrm{Pr} V_w^+\right) - 1 \right] \tag{2.79}$$

and for the mass fraction:

$$Y_v^+ = \frac{1}{V_w^+} \left[\left(\frac{V_w^+}{2\kappa} \ln\left(\frac{y^+}{10.8}\right) \exp\left(-\frac{10.8 V_w^+}{2}\right) + 1 \right)^{2\mathrm{Sc}_t} \exp\left(13.2 \mathrm{Sc} V_w^+\right) - 1 \right]. \tag{2.80}$$

These three wall functions are valid for $y^+ > 10.8$. Below this value, they take the form:

$$U^+ = \frac{1}{V_w^+} \left[\exp\left(y^+ V_w^+\right) - 1 \right] \tag{2.81}$$

$$T^+ = \frac{1}{V_w^+} \left[\exp\left(\mathrm{Pr} y^+ V_w^+\right) - 1 \right] \tag{2.82}$$

$$Y_v^+ = \frac{1}{V_w^+} \left[\exp\left(\mathrm{Sc} y^+ V_w^+\right) - 1 \right] \tag{2.83}$$

A work similar to that of Leduc was published by Zaichik et al [Zaichik et al., 1997] but

with the hypothesis of weak aspiration which allows to express:

$$\exp\left(\frac{10.8V_w^+}{2}\right) \approx 1 + \frac{10.8V_w^+}{2} \tag{2.84}$$

Travis in 2007 [Travis, 2007] conducted the same argument as Zaichik and arrived at the same expression. Oh et al. [Oh and Revankar, 2005] took into account suction in the wall functions to model the condensation of steam inside a tube of radius R in the presence of non-condensable gases and taking into account the liquid film. The model used contains several assumptions to deal with the mixing length l_m according to the model introduced by Prandtl. They are based on the principle that suction acts as a damping factor ($l_m * \mathrm{DF}$) of this mixing length and study four models:

- the Schlichting model without taking into account the suction ($\mathrm{DF} = 1$) :

$$\frac{l_m}{R} = 0.4\frac{y}{R} - 0.44\left(\frac{y}{R}\right)^2 + 0.24\left(\frac{y}{R}\right)^3 - 0.06\left(\frac{y}{R}\right)^4 \tag{2.85}$$

- the Schlichting model with the Van-Driest damping coefficient:

$$\mathrm{DF} = 1 - \exp\left[-\frac{y^+}{26}\right] \tag{2.86}$$

- the Schlichting model with the Kinney damping coefficient:

$$\mathrm{DF} = 1 - \exp\left[-\frac{y^+V_w^+}{2} - \frac{1}{\sqrt{2}}\sqrt{\sqrt{\left(\frac{y^+V_w^+}{2}\right)^4 + 4\left(\frac{y^+}{A^+}\right)^4} + \left(\frac{y^+V_w^+}{2}\right)^2}\right] \tag{2.87}$$

- the Schlichting model with the Kayes damping coefficient:

$$\mathrm{DF} = 1 - \exp\left[-\frac{y^+\left(1 - 9V_w^+\right)}{26}\right] \tag{2.88}$$

- the Reichardt model giving directly the value of the turbulent viscosity as a function of y^+:

$$\frac{\mu_t}{\mu} = \frac{y^+}{2.5}.\frac{1}{6}\left[1+\frac{r}{R}\right]\left[1+2\left(\frac{r}{R}\right)^2\right] \tag{2.89}$$

It should also be mentioned that the film thickness is subtracted from y^+. In their validation work, they observed that the turbulence model is dominant when the non-condensable gases concentration is low. Of the five models presented, the use of the Reichardt analytical formula represents the best compromise. Finally, it should be noted that the authors verify the thickness of the velocity boundary layer against the expression of Kays et al. [Kays, 1972] (equation (2.25)):

$$\delta_M(z) = 0.371z\left(\frac{U_\infty z}{\nu}\right)^{-0.2} \tag{2.90}$$

and the laminar character of the liquid film with respect to the correlations of [Rohsenow, 1956] and [Mudawwar and El-Masri, 1986]. Finally, more recently Lehmkuhl et al [Lehmkuhl et al., 2016] proposed to extend the previous work by using the Van-Driest model but modifying the constant A^+ according to the work of Cebeci et al [Cebeci, 1970]:

$$A_c^+ = 26\left[\exp\left(V_w^+\delta_v^+\right)\right]^{-1/2} \tag{2.91}$$

and by proposing that δ_v^+ is influenced by suction with:

$$\delta_v^+ = 27\exp\left[-\frac{V_w^+ - 0.09}{0.09}\right] \tag{2.92}$$

In his work, Lehmkuhl simply focused on the wall function for velocity with consideration of suction. Other publications by the Aachen/Julich research group [Hundhausen et al., 2017] propose to refer to the wall function of chemical species proposed by [Kader, 1981]

which is written as

$$Y_v^+ = \frac{\rho u_\tau}{\dot{m}''}\left(Y_v - Y_{v,w}\right) = \mathrm{Sc} y^+ e^{-\Gamma} + \left(\frac{Sc_t}{\kappa}\ln\left(y^+\right) + \beta\left(\mathrm{Sc}\right)\right) e^{-1/\Gamma} \tag{2.93}$$

They point out that this type of wall function does not take into account certain effects which take place in our case of interest such as the development of the boundary layer, the effect of suction towards the wall which decreases the thickness of this boundary layer and thus increases the transfers and the buoyancy effects. In this same publication, some ideas are proposed such as the addition of a $1/\Phi$ term in front of the logarithmic part of the previous wall function to add convection in this logarithmic zone and the determination of an adequate β function. The effect of buoyancy suggests the introduction of another dimensionless quantity to describe the deformation of the wall velocity profile. On the Φ term, Muller et al. [Muller et al., 2016] describe the approach. With suction, the local transport balance of chemical species is no longer zero but equal to the convection term due to suction. Then, they assume that this term is constant and equal to C_y and proceed in a classical way with the wall functions to write :

$$Y_v^+ = \frac{\rho u_\tau}{\dot{m}''}\left(Y_v - Y_{v,w}\right) = \left[y^+\mathrm{Sc} + \frac{C_y \nu \mathrm{Sc}}{u_\tau \dot{m}''}\left(y^+\right)^2\right] e^{-\Gamma} + \frac{1}{\Phi}\left(\frac{Sc_t}{\kappa}\ln\left(y^+\right) + \beta\left(\mathrm{Sc}\right)\right) e^{-1/\Gamma} \tag{2.94}$$

with Φ:

$$\Phi = 1 + \frac{\mathrm{Sc}_t \mu C_y y^+}{\kappa \rho^2 u_\tau^2 \left(Y_{v,\infty} - Y_{v,w}\right)}. \tag{2.95}$$

Finally, the most recent approach of Julich's team was the publication by Kelm et al [Kelm et al., 2019]. They introduced an unbalanced or pre-factor to account for the change in standard wall functions in the presence of wall condensation. These factors (there is one for each wall function) depend on two new scales: the condensation rate $\dot{q}^+$ and the buoyancy F_g^+ defined by:

$$\dot{q}^+ = \frac{1}{u_\tau}\frac{\dot{q}_w}{H_{lat}\rho_w} \tag{2.96}$$

$$F_g^+ = \left(\frac{\partial p}{\partial x} - \rho_w g \right) \frac{\mu_w}{\rho_w^2 u_\tau^3} \tag{2.97}$$

At present, only the velocity factor has been extracted from experimental results, the other two have been constructed from low Reynolds number calculations of the same tests.

Finally, two recent works are worth mentioning, those of Lee et al [Lee et al., 2018] and Li et al [Li et al., 2019]. In the first one, a film model is present and a wall function on the temperature associated with an assumption of analogy between heat transfer and mass transfer allow to solve the problem. Nothing is mentioned about the wall function for velocity. The wall function on temperature chosen is:

$$T^+ = 5 \left[\mathrm{Pr} + \ln\left(1 + 5\mathrm{Pr}\right) + \frac{1}{5\kappa} \ln\left(\frac{y^+}{30} \right) \right]. \tag{2.98}$$

In the second reference, the three wall functions are specified. For the velocity, the authors simply use the classical logarithmic law without taking into account the suction. Then, for the other functions Θ^+ and Y_v^+, the authors use the work on natural convection of Holling et al. [Holling and Herwig, 2005]. The latter have proposed characteristic quantities to consider wall functions in velocity and temperature. They introduce a reference temperature T_{fc}:

$$T_{fc} = \left(\frac{\alpha^2}{g\beta} \left| \frac{\partial T}{\partial y} \right|_w \right)^{1/4} \tag{2.99}$$

and use it to express Θ^+ now denoted $\Theta^x = \left(T - T_w\right)/T_{fc}$. The wall functions are then derived by mixing the expressions for forced and natural convection to cover all flow regimes. Nevertheless, the suction velocity is not included in these expressions.

In an attempt to summarise this literature review, we summarise in TAB. 2.1 the approaches chosen by [Leduc, 1995], [Li et al., 2019] and [Kelm et al., 2019] for the three wall functions assuming that the interface velocity U_i^+ is neglected.

The information in the TAB. 2.1 provides the following remarks and comments:

Function	[Leduc, 1995]	[Li et al., 2019]	[Kelm et al., 2019]
$U^+ = \frac{U}{u_\tau}$	$\frac{1}{V^+}\left[\exp\left(y^+V^+\right)-1\right]$ if $y^+ < 10.8$ $\frac{1}{V^+}\left[\left(\frac{V^+}{2\kappa}\ln\left(\frac{y^+}{10.8}\right)+\exp\left(\frac{10.8V^+}{2}\right)\right)^2-1\right]$ otherwise.	y^+ if $y^+ = \frac{u_\tau y}{\nu} < 10.8$ $\frac{1}{\kappa}\ln y^+ + 5.5$ otherwise.	$\Psi_u\left(y^+, F_g^+, \dot{q}^+\right)\sqrt[4]{\left(1/\left(U_l^+\right)^4 + 1/\left(U_t^+\right)^4\right)^{-1}}$ $U_l^+ = y^+$ $U_t^+ = \frac{1}{\kappa}\ln y^+ + 5.2$
$\Theta^+ = \frac{T_w - T}{T_c}$ $T_c = \frac{\dot{q}_{conv}}{\rho C_p u_\tau}$	$\frac{1}{V^+}\left[\exp\left(\mathrm{Pr}y^+V^+\right)-1\right]$ if $y^+ < 10.8$ $\frac{1}{V^+}\left[\left(\frac{V^+}{2\kappa}\ln\left(\frac{y^+}{10.8}\right)\right.\right.$ $\left.\left.\exp\left(-\frac{10.8V^+}{2}\right)+1\right)^{2\mathrm{Pr}_t}\exp\left(13.2\mathrm{Pr}V^+\right)-1\right]$ otherwise.	$\Theta^+ = \phi\Theta^+_{nat} + (1-\phi)\Theta^+_{for}$ $\phi = \frac{1}{\pi}\arctan 10\ln \mathrm{Ri}_x + 0.5$ $\mathrm{Ri}_x = \mathrm{Gr}_x/\mathrm{Re}_x^2$ $\mathrm{Gr}_x = g\beta\Delta T x^3/\nu^2\ \mathrm{Re}_x = Ux/\nu$ $\Theta^+_{for} = \mathrm{Pr}y^+$ if $y^+ < y_p^+$ $\Theta^+_{for} = \mathrm{Pr}_t\left(u^+ + \mathrm{Pr}_f\right)$ if $y^+ \geq y_p^+$ $\mathrm{Pr}_f = 9.24\left[\left(\frac{\mathrm{Pr}}{\mathrm{Pr}_t}\right)^{1/4}-1\right]\left[1+0.28\exp\left(-0.007\frac{\mathrm{Pr}}{\mathrm{Pr}_t}\right)\right]$ $\Theta^+_{nat} = \left(\frac{1}{\left(\Theta^+_{nat,l}\right)^{3.5}} + \frac{1}{\left(\Theta^+_{nat,t}\right)^{3.5}}\right)^{-2/7}$ $\Theta^+_{nat,l} = \mathrm{Pr}y^+$ $\Theta^+_{nat,t} = \frac{1.724}{\mathrm{Pr}}\left[C\left(\ln y^+ - \ln\left(\frac{1.724}{\mathrm{Pr}^2}\right)\right)+D\right]$ $C = 0.488 + \frac{0.101}{\xi}, D = 1.77 - \frac{0.1328}{\xi}$ $\xi = 3.51\times10^{-3}\mathrm{Gr}_x\mathrm{Pr}/10^6$	$\Psi_T\left(y^+, F_g^+, \dot{q}^+\right)\sqrt[4]{\left(1/\left(\Theta_l^+\right)^4 + 1/\left(\Theta_t^+\right)^4\right)^{-1}}$ $\Theta_l^+ = \mathrm{Pr}y^+$ $\Theta_t^+ = 2.12\ln y^+ + f(\mathrm{Pr})$ $f(\mathrm{Pr}) = \left(3.85\mathrm{Pr}^{1/3}-1.3\right)^2 + 2.12\ln(\mathrm{Pr})$
$Y^+ = \frac{Y_w - Y}{Y_c}$ $Y_c = -\frac{\dot{m}_v}{\rho u_\tau}$	$\frac{1}{V^+}\left[\exp\left(\mathrm{Sc}y^+V^+\right)-1\right]$ if $y^+ < 10.8$ $\frac{1}{V^+}\left[\left(\frac{V^+}{2\kappa}\ln\left(\frac{y^+}{10.8}\right)\right.\right.$ $\left.\left.\exp\left(-\frac{10.8V^+}{2}\right)+1\right)^{2\mathrm{Sc}_t}\exp\left(13.2\mathrm{Sc}V^+\right)-1\right]$ otherwise.	$Y^+ = \phi Y^+_{nat} + (1-\phi)Y^+_{for}$ $Y^+_{for} = \mathrm{Sc}y^+$ if $y^+ < y_p^+$ $Y^+_{for} = \mathrm{Sc}_t\left(u^+ + \mathrm{Sc}_f\right)$ if $y^+ \geq y_p^+$ $\mathrm{Sc}_f = 9.24\left[\left(\frac{\mathrm{Sc}}{\mathrm{Sc}_t}\right)^{1/4}-1\right]\left[1+0.28\exp\left(-0.007\frac{\mathrm{Sc}}{\mathrm{Sc}_t}\right)\right]$ $Y^+_{nat} = \left(\frac{1}{\left(Y^+_{nat,l}\right)^{3.5}} + \frac{1}{\left(Y^+_{nat,t}\right)^{3.5}}\right)^{-2/7}$ $Y^+_{nat,l} = \mathrm{Sc}y^+$ $Y^+_{nat,t} = \frac{1.724}{\mathrm{Sc}}\left[C\left(\ln y^+ - \ln\left(\frac{1.724}{\mathrm{Sc}^2}\right)\right)+D\right]$	$\Psi_Y\left(y^+, F_g^+, \dot{q}^+\right)\sqrt[4]{\left(1/\left(Y_l^+\right)^4 + 1/\left(Y_t^+\right)^4\right)^{-1}}$ $Y_l^+ = \mathrm{Sc}y^+$ $Y_t^+ = 2.12\ln y^+ + f(\mathrm{Sc})$ $f(\mathrm{Sc}) = \left(3.85\mathrm{Sc}^{1/3}-1.3\right)^2 + 2.12\ln(\mathrm{Sc})$

Table 2.1: Comparison of the selected wall functions during filmwise condensation according to [Leduc, 1995], [Li et al., 2019] and [Kelm et al., 2019].

- In the approach proposed by Kelm et al, all the effects are contained in the pre-factors Ψ;

- In the approach of Li et al, we note that the suction V_w^+ is not explicitly taken into account (it is assumed to be weak, which simplifies the Leduc expressions), that the local Grashof number Gr_x only takes into account thermal effects and not mass effects and that the geometrical dimension x is not clearly defined (in general it is the distance to the origin of the boundary layer but the text is ambiguous because it seems that the length scale is taken as unitary). For the constants, the references are given in the original article.

The analysis of these different formulations is conducted in the Chapter 5 in comparison with simplified modeling.

2.3 Data available for the validation of local models

For steam condensation in the presence of non-condensable gases, there are few experimental results with detailed measurements in the boundary layer for a channel flow. To our knowledge, only the work of Legay-Desesquelles et al. [Legay-Desesquelles and Prunet-Foch, 1985], the COPAIN tests [Bazin and Castelli, 2000] and the recent SETCOM tests [Hundhausen et al., 2017] have addressed this type of measurement, the first with point measurements of velocity with a Pitot tube, the second with point measurements of temperature and concentration and the last with measurements of velocity by Laser Doppler Velocimetry (LDV) and Particle Image Velocimetry (PIV).

The first tests by Legay et al were carried out in a wind tunnel of 0.8 m in length and 0.2×0.4 m^2 in cross-section. At atmospheric pressure, a saturated air/steam mixture was injected at a velocity of 5.3 m/s and a temperature of about 85° C. Two velocity profiles

measured with a Pitot tube are provided in the article for a wall temperature equal to the injection temperature and a wall cooled to 70° C.

The test section of the COPAIN facility consists of a vertical rectangular channel with a cross section of 0.6 m by 0.5 m. A condensation plate is on one sidewall of the channel with an area of 0.6 m by 2.0 m (FIG. 4.7 center). For the COPAIN tests with local measurements, a mobile probe was equipped with two thermocouples and a sampling capillary (FIG. 4.7 right). Measurements of normal temperature profiles and saturation temperatures were made at three heights in a series of dedicated COPAIN tests ($n = 2$ corresponds to $z = 0.75$ m, $n = 3$ to $z = 1.25$ m and $n = 4$ to $z = 1.75$ m). It should be added that Bucci conducted an analysis of these tests in his thesis work [Bucci, 2009] and identifies that the fluid sampling velocities (0.1 to 0.2 m/s), in the tests, are much higher than the suction velocities, therefore, this measurement probably disturbs the boundary layer which may explain the differences observed with the numerical results.

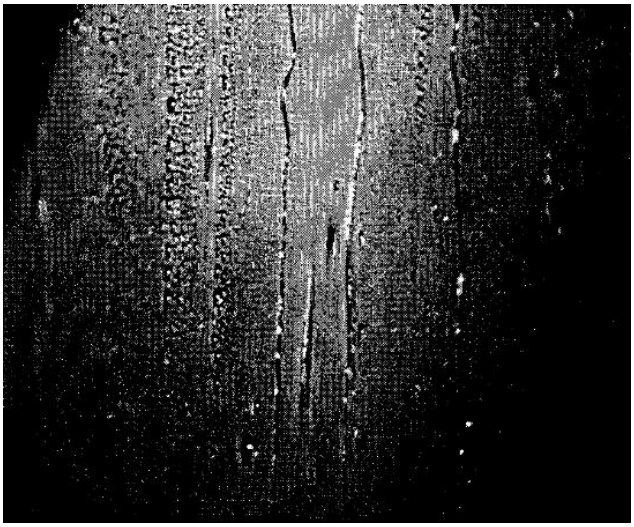

Figure 2.4: Picture of Filmwise condensation with rivulets – COPAIN Experiments

The SETCOM test section consists of a rectangular flow channel (0.44 mx0.44 m) with three adiabatic walls and a 6 m long cooling plate. For the SETCOM tests, the measurement campaigns began with the validation of the PIV and LDV systems on isothermal flows. The laser measurements do not systematically allow to measure the velocity profile up to the viscous sub-layer in order to determine the u_τ velocity necessary to scale the

profiles. Therefore, in some cases, numerical simulations using low Reynolds turbulence model carried out in parallel with the tests provided this value. The condensation measurements were first carried out in forced convection and they observed that the change in velocity had no effect on the profile and the change in driving force i.e. $X_{v,\infty} - X_{v,w} / (1 - X_{v,w})$ has only a marginal effect. Then they decreased the injection speed to increase the buoyancy effect. The change in the profile is very noticeable in the mixed convection regime. Most of the available results are only qualitative and until recently the uncertainties in the measured fluxes were too large. Finally, attempts to measure temperature and concentration profiles by Raman spectrometry had not yet been successful due to severe light reflection problems. Very recently, Kelm et al introduced an imbalance factor Ψ to account for the change in standard wall functions in the presence of wall condensation.

To conclude this bibliographical review, it is also necessary to mention the measurements carried out in the TOSQAN facility [Malet et al., 2010, 2012] in the near wall. The measurements mainly concern velocity profiles by particle image velocimetry. The geometry of the installation makes the interpretation with numerical tools more complex than in the case of rectangular channels. Consequently, we will not consider these results in our analyses.

The COPAIN tests are our most important database for the validation of our numerical work. However, the velocity profile was not measured during the tests and therefore we have to use the detailed calculations with the low Reynolds number model to have all the information needed to elaborate dimensionless profiles (especially the friction velocity u_τ). In order to characterise these different tests from a convection flow point of view, it is important to provide some dimensionless numbers. The Richardson number defined by:

$$\mathrm{Ri} = \frac{\mathrm{Gr}}{\mathrm{Re}^2} = \frac{\rho_w - \rho_{in}}{\rho_{in}} \frac{g L}{U_{in}^2} \tag{2.100}$$

is used by [Kelm et al., 2019] and [Bucci, 2009]. L represents a length scale which usually

corresponds to the distance x to the origin of the boundary layer, Gr the Grashof number defined by :

$$\mathrm{Gr} = \frac{\rho_w - \rho_{in}}{\rho_{in}} \frac{g L^3}{\nu_{in}^2} \tag{2.101}$$

and Re the Reynolds number written as:

$$\mathrm{Re} = \frac{\rho_{in} U_{in} L}{\mu_{in}}. \tag{2.102}$$

It is also interesting to consider the Rayleigh number Ra $=$ GrPr where Pr is the Prandtl number defined by Pr $= \nu_{in}/\alpha_{in}$ with α_{in} representing the thermal diffusivity of the gas mixture at injection. In our analysis, we have chosen the physical properties of the mixture at the inlet rather than a 'film' condition usually constructed from a weighting between the inlet and the wall.

For our analysis in Chapter 5, we select five tests to cover the different convection regimes for the simulations: P064 and P070 for forced convection, P074 for natural convection, P066 and P071 for mixed convection with the effect of total pressure. The boundary conditions corresponding to the five tests and used for the numerical calculations are summarised in Tab. 2.2. They correspond to the outermost level ($n = 4$) of the inlet to ensure full development of the boundary layers. The measured boundary layers for four of these five tests are plotted in FIG. 2.5.

The experimental uncertainties for the measurements are $+/-20$ mbar for pressure, $+/-0.6$ K for temperature, $+/-0.04$ m/s for velocities and $0.06\Phi + 100$ for total heat fluxes.

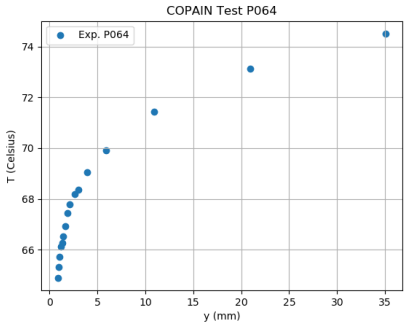

(a) P064 $Z = 1.75$ m Temperature

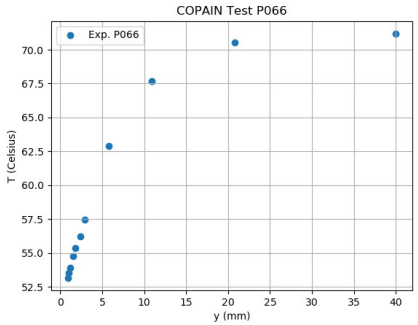

(b) P066 $Z = 1.75$ m Temperature

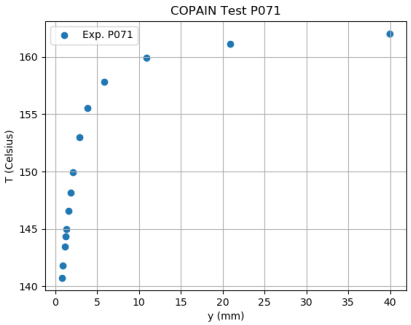

(c) P071 $Z = 1.75$ m Temperature

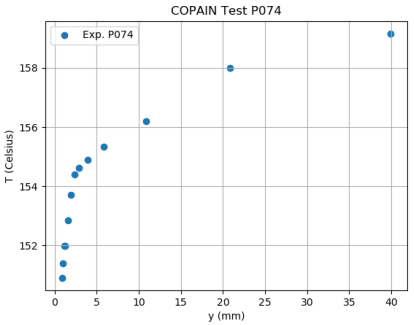

(d) P074 $Z = 1.75$ m Temperature

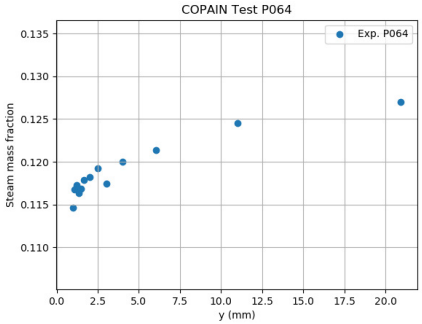

(e) P064 $Z = 1.75$ m Mass fraction

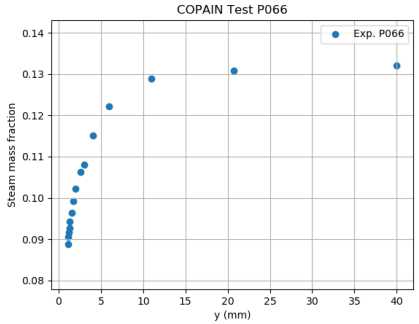

(f) P066 $Z = 1.75$ m Mass fraction

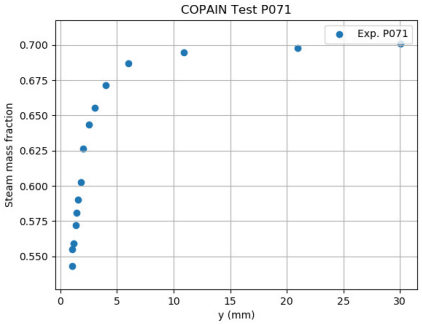

(g) P071 $Z = 1.75$ m Mass fraction

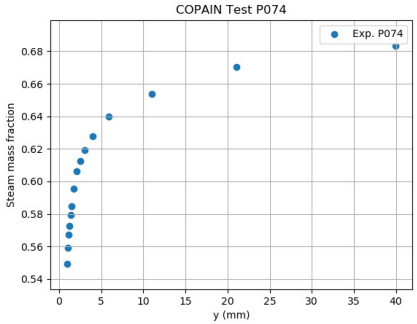

(h) P074 $Z = 1.75$ m Mass fraction

Figure 2.5: Selected COPAIN test results with local measurements compared to simulations.

Test	T_{bulk} (°C)	$Y_{v,bulk}$	u_{bulk} (m/s)	P_{bulk} (bar)	T_w (°C)	$Y_{v,w}$
P064_4	75.5	0.127	3.0	1.203	56.5	0.093
P066_4	71.5	0.128	1.0	1.208	47.7	0.059
P070_4	162,5	0.701	2.02	6.605	140,52	0,446
P071_4	162.6	0.702	1.0	6.608	130.5	0.312
P074_4	160.1	0.698	0.2	6.479	142.8	0.496
Test	Re	Gr	Ri	Ra	Φ [W/m^2	Flow Regime
P064_4	313234.	1.42E+10	0.14490	1.04E+10	1175.	Forced
P066_4	107287.	2.24E+10	1.9505	1.64E+10	835.	Mixed
P070_4	806474.	4.56E+11	0.7009	4.48E+11	22416	Forced
P071_4	399311.	7.87E+11	4.9352	7.74E+11	18976.	Mixed
P074_4	79188.	3.45E+11	55.000	3.39E+11	26740.	Free

Table 2.2: COPAIN: Initial and boundary conditions for the five calculated tests.

2.4 Conclusions of the chapter

In the literature review on wall condensation, we have seen that terms in the balance equations are often neglected without any real theoretical and practical justification. This is particularly true for:

- the Soret or thermodiffusion effect in water vapour transport;
- the interdiffusion of species in the energy equation;
- the Dufour effect in the energy equation;
- large density variations in general.

In the first chapter (chapter 3), an analysis of the effect of these different hypotheses is carried out on the model problem of the doubly diffusive square cavity with condensation and evaporation in the wall.

Then, the limited experimental data available for the validation of local tools dealing with wall condensation leads us to perform numerical experiments to generate data for scaling up to wall functions. We have chosen this last approach because it is the only one achievable today to perform numerical field calculations at the scale of a reactor building.

In chapter 4, low Reynolds number turbulent models associated with the solution of the conservation equations are used to recalculate the most relevant experiments. This provides all the data necessary to generate the scaled profiles that form the baseline for the wall functions. Our validation approach is progressive, starting with an isothermal turbulent channel before adding the suction effect and finally the heat mass transfers associated with condensation.

In the literature review, different approaches were followed to derive wall functions. Each of these methods requires an eddy viscosity profile in the boundary layer usually in the form of a mixing length. Van Driest introduces first the damping factor for a pure dynamic boundary layer. Then, the effect of different phenomena acting on film condensation (suction, variables properties...) have been proposed but they are not systematically taken into account in the derivation of a wall function suitable for our phenomenon of interest. Consequently, With the validation data, we discuss in Chapter 5 the improvement of the wall functions by taking into account important effects that are usually neglected. We detail the chosen method as well as the validation on cases similar to the analysis with low Reynolds number turbulent models.

Finally, all the work in this dissertation is carried out with a single-phase approach. Therefore, we do not take into account the possibility of condensation of steam in the core of the flow as it approaches the wall, nor the creation and transport of the film or drops created by the phase change. As already mentioned, we place ourselves in the case where the resistance of the non-condensable layer in the vicinity of the wall constitutes the dominant resistance to all transfers.

Chapter 3

Interdiffusion, Soret and Dufour effects for coupled heat and mass transfer in a square cavity: laminar model

3.1 Introduction

In this chapter we construct a model for coupled heat and mass transfer in the laminar case. As we will show below, coupling effects are generally not addressed or addressed incorrectly in many scientific studies. Our goal is to determine under which conditions coupling effects can safely be neglected, which may not always be possible inside boundary layers. As a first step, we derive and test our model for a two-dimensional, differentially heated square cavity containing air and water vapor, as depicted on the FIG. 3.1.

At the hot wall of the cavity, which corresponds to the left wall in FIG. 3.1, water evaporation takes place at a constant temperature T_H. A constant concentration of water vapor Y_v is taken at saturation condition at temperature T_H. At the cold wall, located on the right side of the picture, water condensation occurs at constant temperature T_C. The value for

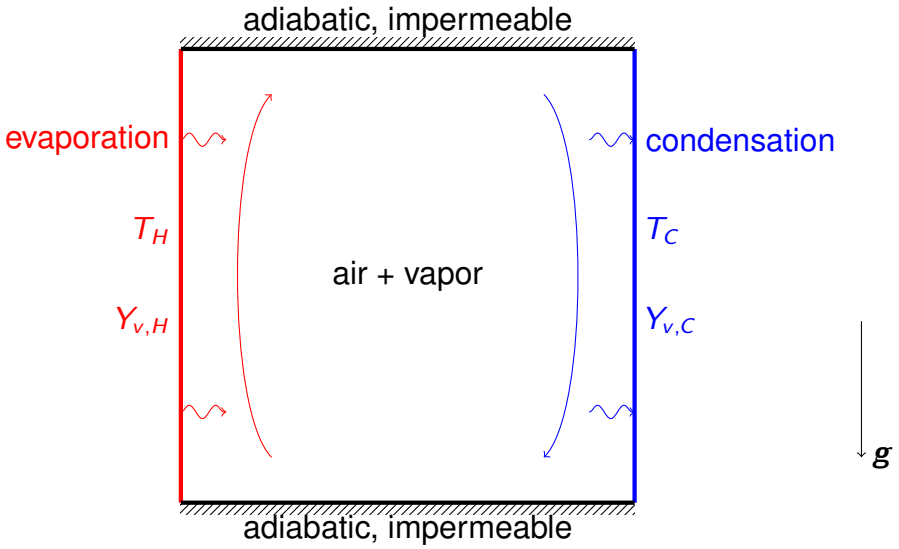

Figure 3.1: Natural convection in binary gases with horizontal temperature and concentration gradients in a square cavity.

the mass fraction of vapor $Y_{v,C}$ is determined, as before, at saturation condition at T_C. The boundary values at the hot (resp. cold) wall will be denoted in this paper with a subscript $._H$ (resp. $._C$).

A considerable number of papers has been devoted to pure thermal natural convection inside a two-dimensional square cavity. The Boussinesq model and the low Mach number models have been applied which resulted in a number of well-established reference solutions. For example, Virendeels in [Vierendeels et al., 1999] gives a reference solution corresponding to large temperature-difference case. We shall use these results to validate the purely thermal part of our model.

We now give a brief review of the literature for coupled heat ad mass transfer. For binary mixtures involving a condensation effect, Weaver and Viskanta [Weaver and Viskanta, 1991a] proposed to solve a double-diffusive system for temperature and concentration variables inside a square cavity. In their work, the density varies with the temperature and concentration, while the total pressure of the system is assumed to be constant and equal to the initial value. The authors neglected all coupling effects apart from the mass diffusion obeying the Fick's law and the heat diffusion obeying the Fourier's law. This double-

diffusive model fails in cases where condensation or evaporation effects are initially strong [Sun et al., 2010], and, as we shall show in this work, this model does not guarantee the energy conservation law. In the second part of their work [Weaver and Viskanta, 1991b] the authors investigated the influence of species interdiffusion on the numerical solutions. The conclusions of their work are, however, questionable for the reasons given above.

Sun et al. applied the low Mach number model to a similar problem [Sun et al., 2010] and the effect of the total pressure variation was taken into account. The dimensionless form of their system of equations does not allow to consider a mixture of two gases having different specific heat ratios, which is an essential shortcoming. Moreover, the authors neglected the species interdiffusion phenomenon meaning that the model remains double-diffusive. In order to enforce the energy conservation inside the computational domain, the authors redefined the Nusselt number and Sherwood number according to the mathematical form of their energy transport equation. This modification enables them to balance the total Nusselt numbers on the left and right sides of the cavity at steady state, but the physical meaning of these numbers is lost.

Weaver and Viskanta [Weaver and Viskanta, 1991b] investigated the influence of species interdiffusion under small heat capacity variation, alongside with Soret and Dufour effects. But the formulation of their Dufour effect heat flux is not consistent and more development is needed. A simplified model, as recently applied by Kefayati [Kefayati, 2015, 2016a,b], takes into account these effects. However the study is carried out in a square cavity without condensation or evaporation.

In the next sections we construct a low-Mach number model which satisfies the energy conservation law. The definition of the total Nusselt number involve all coupling effects in accordance to the solved equations. Moreover, the model allows having different specific heat ratios for each component of the binary mixture. Comparison of the Nusselt numbers on both cavity sides shows that energy is conserved and that definitions are consistent.

The model is derived in section 3.2. Non-dimensional parameters are defined in section 3.3. The numerical algorithm used to compute the transfer is described in section 3.4. Validation and comparison with reference results is given in section 3.5. New results for an air-steam mixture are presented in section 3.6.

3.2 Analysis

We consider a gas mixture of density ρ , pressure P , temperature T. Let Y_k be the mass fraction of a component k, c_p (c_v respectively) the specific heat at constant pressure (at constant volume respectively), h the specific enthalpy, $\boldsymbol{U}$ the velocity, $\boldsymbol{\phi}$ the mass flux, $\boldsymbol{g}$ the gravitational acceleration and m the total mass of gas in the cavity. The partial quantity s of component $k \in \{a, v\}$ will be indexed with a suffix k.

The binary mass diffusion coefficient D and the kinetic viscosity ν are supposed to be constant.

The gas mixture satisfies the Navier-Stokes equations:

$$\frac{\partial \rho}{\partial t} + \nabla \cdot \rho \boldsymbol{U} = 0, \tag{3.1}$$

$$\frac{\partial \rho Y_k}{\partial t} + \nabla \cdot \rho Y_k \boldsymbol{U} = -\nabla \cdot \boldsymbol{j}_k, \tag{3.2}$$

$$\frac{\partial \rho \boldsymbol{U}}{\partial t} + \nabla \cdot \rho \boldsymbol{U} \otimes \boldsymbol{U} = -\nabla P + \nabla \cdot \boldsymbol{\tau} + \rho \boldsymbol{g}, \tag{3.3}$$

$$\frac{\partial \rho h_t}{\partial t} + \nabla \cdot \rho \boldsymbol{U} h_t = -\nabla \cdot (\boldsymbol{q} + \boldsymbol{U} \cdot \boldsymbol{\tau}) + \frac{\partial P}{\partial t}, \tag{3.4}$$

where $\boldsymbol{j}_k = \boldsymbol{j}_{k,F} + \boldsymbol{j}_{k,S}$ and $\boldsymbol{q} = \boldsymbol{q}_F + \boldsymbol{q}_I + \boldsymbol{q}_D$. Fick's law and Fourier's law are applied

$$\boldsymbol{j}_{k,F} = -\rho D \nabla Y_k, \tag{3.5}$$

$$\boldsymbol{q}_F = -\lambda \nabla T. \tag{3.6}$$

In addition, (3.1) and (3.2) lead to

$$\sum_k \boldsymbol{j}_k = \boldsymbol{0}. \tag{3.7}$$

3.2.1 Partial velocities

From (3.2), one identifies the partial mass flux of k-th component

$$\boldsymbol{\phi}_k = Y_k \boldsymbol{\phi} + \boldsymbol{j}_k \tag{3.8}$$

and one defines the k-th component partial velocity as

$$\boldsymbol{U}_k = \boldsymbol{U} + \frac{\boldsymbol{j}_k}{\rho Y_k} \tag{3.9}$$

3.2.2 Gas properties

We consider the ideal gas model for the gas mixture. To simplify the work, we make several assumptions. We consider a mixture of two gases with following properties:

- the two gases obey separately the ideal gas law

$$\rho_k = \frac{P_k}{r_k T} \tag{3.10}$$

where we define $r_k = R/M_k$ the specific gas constant;

- for each gas, the specific heat ratio $\gamma_k = c_{p,k}/c_{v,k}$ is constant;
- the internal energy of the mixture is equal to the sum of the partial internal energies: $\rho e = \sum_k \rho_k e_k$.

These assumptions lead to the following properties of the binary gas mixture:

- $c_{p,k}$ and $c_{v,k}$ are constant;
- the mixture satisfies the ideal gas law

$$\rho = \frac{P}{rT}; \tag{3.11}$$

- the enthalpy of the mixture is equal to the sum of the partial enthalpies: $\rho h = \sum_k \rho_k h_k$;
- the specific gas constant r and the specific heats of the mixture c_v and c_p are independent of temperature and equal to the weighted average of the each substance weighted by their mass fraction: $s = \sum_k Y_k s_k$ where $s = r$, c_v or c_p;
- the specific heat ratio γ is independent of temperature and function only to the composition;
- the Mayer's relation holds:

$$r = c_p - c_v. \tag{3.12}$$

3.2.3 Species interdiffusion

The enthalpy per unit volume of the mixture is the sum of partial enthalpies per unit volume of each component: $\sum_k \rho Y_k h_k = \rho h$. However, the enthalpy flux per unit volume is not

equal to the sum of partial fluxes per unit volume, i.e.

$$\sum_k \rho_k h_k \boldsymbol{U}_k = \sum_k h_k \left(\rho_k \boldsymbol{U} + \boldsymbol{j}_k\right) = \rho h \boldsymbol{U} + \sum_k h_k \boldsymbol{j}_k. \tag{3.13}$$

The term $\sum_k h_k \boldsymbol{j}_k$ shows that there exists a heat flux induced by the concentration transport, which we call species interdiffusion flux or simply interdiffusion flux, noted

$$\boldsymbol{q}_I = \sum_k h_k \boldsymbol{j}_k. \tag{3.14}$$

Note that the interdiffusion flux is independent of the transport of specific heat induced by the transport of concentration.

In the case of a binary mixture, (3.14) yields

$$\boldsymbol{q}_I = \left(c_{p,v} - c_{p,a}\right) T \boldsymbol{j}_v \tag{3.15}$$

which means that the intensity of species interdiffusion is proportional to the specific heat capacity difference of two components.

3.2.4 Soret and Dufour effects

According to [Bird et al., 2006], Soret and Dufour effects appear in the case of simultaneous mass and heat transfer as a result of chemical potential, with the following expressions:

$$\boldsymbol{j}_{v,\text{Soret}} = \alpha_d \rho D Y_v \left(1 - Y_v\right) \frac{1}{T} \nabla T \tag{3.16}$$

$$\boldsymbol{q}_{\text{Dufour}} = \alpha_d R T \frac{M}{M_a M_v} \boldsymbol{j}_v \tag{3.17}$$

where α_d is the thermal diffusion ratio for vapour in air. According to [Bird et al., 2006], in a binary mixture, it is nearly independent of temperature and mass fractions of the constituents.

Note that $\boldsymbol{j}_v = \boldsymbol{j}_{v,\text{Fick}} + \boldsymbol{j}_{v,\text{Soret}}$ and that $\boldsymbol{q}_I$ and $\boldsymbol{q}_D$ depend both on $\boldsymbol{j}_v$. We define respectively the interdiffusion heat flux and the Dufour effect heat flux originated from Fick's law mass flux and Soret effect mass flux, noted as $\boldsymbol{q}_{IF}$, $\boldsymbol{q}_{IS}$, $\boldsymbol{q}_{DF}$ and $\boldsymbol{q}_{DS}$.

Soret effect and Dufour effect are usually neglected, which makes the system simpler [Leduc, 1995; Sun et al., 2010; Weaver and Viskanta, 1991a], but it is not clear that this is always justified. Weaver and Viskanta [Weaver and Viskanta, 1991b] investigated the influence of these two effects, but due to an apparent inconsistency in their definition of the Dufour effect (which can be found with dimension analysis) it appears that some further examination may be necessary.

3.2.5 Velocity boundary conditions modelling wall condensation and evaporation

The evaporation and condensation effects are modelled by the velocity boundary condition on the vertical walls.

In the case of binary mixed gas of air and vapour, one obtains by noticing $Y_a = 1 - Y_v$ and $\boldsymbol{j}_v = -\boldsymbol{j}_a$,

$$\boldsymbol{U}_a = \boldsymbol{U} - \frac{1}{\rho(1 - Y_v)}\boldsymbol{j}_v \tag{3.18}$$

which shows that the partial velocity of a substance is the sum of convective velocity and diffusive velocity.

On the vertical walls, because air is not condensable, the air mass flux through the

boundary is zero, i.e. $U_{a,n} = 0$. This leads to

$$U|_{\text{wall},n} = \frac{j_{v,n}}{\rho(1 - Y_v)} \tag{3.19}$$

on these walls.

When Soret effect is neglected, the mass flux is only constituted by Fick's law mass flux and (3.19) becomes

$$U|_{\text{wall},n} = -\frac{D}{(1 - Y_v)} \frac{\partial Y_v}{\partial n} \tag{3.20}$$

which is called Stefan's velocity.

3.2.6 Low Mach number model

The low Mach number model is based on the acoustic wave filtering introduced by Paolucci [Paolucci, 1982]. The idea is, with a low Mach number of the flow, to separate the pressure into a thermodynamic pressure P_{th} and a dynamic one p_d. The calculation of the thermodynamic pressure is based on the total mass conservation in the volume, and it can be calculated by

$$P_{\text{th}} = m \left(\int_{\Omega} \frac{1}{rT} \mathrm{d}V \right)^{-1} \tag{3.21}$$

Furthermore, the assumption of low Mach number enables us to neglect certain terms.

One shall obtain the following system in dimensional and conservative form with $\boldsymbol{\phi} = \rho \boldsymbol{U}$:

$$\frac{\partial \rho}{\partial t} + \nabla \cdot \boldsymbol{\phi} = 0 \tag{3.22}$$

$$\frac{\partial}{\partial t}(\rho \boldsymbol{U}) + \nabla \cdot (\phi \boldsymbol{U}) = \nabla \cdot \tau + \rho \boldsymbol{g} - \nabla p_d \tag{3.23}$$

$$\frac{\partial}{\partial t}(\rho Y_v) + \nabla \cdot (\boldsymbol{\phi} Y_v) = \nabla \cdot (\rho D \nabla Y_v - \boldsymbol{j}_{v,S}) \tag{3.24}$$

$$\frac{\partial}{\partial t}(\rho c_p T) + \nabla \cdot (\boldsymbol{\phi} c_p T) = \nabla \cdot (\lambda \nabla T - \boldsymbol{q}_{IS} - \boldsymbol{q}_D) + \frac{\mathrm{d}P_{\mathrm{th}}}{\mathrm{d}t} + (c_{p,v} - c_{p,a}) \nabla \cdot (\rho D T \nabla Y_v) \tag{3.25}$$

where $\boldsymbol{\tau}$ is the viscosity stress tensor.

3.3 Scaling analysis

3.3.1 Non-Dimensional equations

In the square cavity problem, we have $Y_{v,H}$ and $Y_{v,C}$ as the highest and lowest vapour mass fractions at the walls, and we define $Y_{v,0} = \frac{1}{2}(Y_{v,H} + Y_{v,C})$, $\Delta Y_v = Y_{v,H} - Y_{v,C}$ and dimensionless parameter Y^* varying from -0.5 to $+0.5$: $Y_v = Y_{v,0} + \Delta Y_v Y^*$. The same for dimensional T^*. Similarly, we set $T = T_0 + \Delta T T^*$, where T is the dimensionless temperature varying from -0.5 to $+0.5$. The reference state defining ρ_0, r_0 and $c_{p,0}$ with index 0 of the gas is taken at the initial pressure $P_{\mathrm{th},0}$ and at T_0 and $Y_{v,0}$.

Here we take $U_0 = \sqrt{gL(\varepsilon_T + \varepsilon_m)}$ so that $\mathrm{Re} = \sqrt{\mathrm{Ra}/\mathrm{Pr}}$. One may define several important dimensionless numbers, see TAB. 3.1.

The non-Boussinesq factors are introduced: $\varepsilon_T = \Delta T / T_0$ and $\varepsilon_m = \Delta r / r_0$, where $\Delta r = r_H - r_C$.

Notation	Name	Definition
Ra	Rayleigh number	$\frac{gL^3(\varepsilon_T+\varepsilon_m)}{\nu\alpha_0}$
Pr	Prandtl number	ν/α_0
Sc	Schmidt number	ν/D
Re	Reynolds number	U_0L/ν
Fr	Froude number	$U_0/\sqrt{gL}$

Table 3.1: Definition of dimensionless numbers

We solve the non-dimensional low-Mach equations:

$$\frac{\partial}{\partial t^*}\rho^* + \nabla^* \cdot \boldsymbol{\phi}^* = 0 \tag{3.26}$$

$$\frac{\partial}{\partial t^*}(\rho^* \boldsymbol{U}^*) + \nabla^* \cdot (\boldsymbol{\phi}^* \boldsymbol{U}^*) = \nabla^* \cdot \boldsymbol{\tau}^* + \frac{\rho^* - 1}{\varepsilon_T + \varepsilon_m}\frac{\boldsymbol{g}}{\|g\|} - \nabla^* p_d^* \tag{3.27}$$

$$\begin{aligned}\frac{\partial}{\partial t^*}\left(\rho^* c_p^* T^*\right) + \nabla^* \cdot \left(\boldsymbol{\phi}^* c_p^* T^*\right) = {} & \nabla^* \cdot \left(\frac{1}{\mathrm{Re}\,\mathrm{Pr}}\nabla T^*\right) + \frac{\gamma - 1}{\gamma \varepsilon_T}\frac{\mathrm{d}P_{\mathrm{th}}^*}{\mathrm{d}t^*} \\ & + \frac{1}{\mathrm{Re}\,\mathrm{Sc}}\frac{\Delta c_p}{c_{p,0}}\nabla^* \cdot (\rho^* T^* \nabla Y^*) \\ & + \frac{\alpha_d}{\mathrm{Re}\,\mathrm{Sc}}\frac{\Delta c_p}{c_{p,0}}\nabla^* \cdot \left(\rho^* \frac{Y_v(1-Y_v)}{\Delta Y_v}\frac{\varepsilon_T T^*}{1+\varepsilon_T T^*}\nabla^* T^*\right) \\ & + \frac{\alpha_d}{\mathrm{Re}\,\mathrm{Sc}}\frac{1}{c_{p,0}}\frac{R^2}{M_a \cdot M_v}\nabla^* \cdot \left(\rho^* \frac{1+\varepsilon_T T^*}{\varepsilon_T}\frac{1}{r}\nabla^* Y^*\right) \\ & + \frac{\alpha_d^2}{\mathrm{Re}\,\mathrm{Sc}}\frac{1}{c_{p,0}}\frac{R^2}{M_a \cdot M_v}\nabla^* \cdot \left(\rho^* \frac{Y_v(1-Y_v)}{\Delta Y_v}\frac{1}{r}\nabla^* T^*\right)\end{aligned} \tag{3.28}$$

$$\frac{\partial}{\partial t^*}(\rho^* Y^*) + \nabla^* \cdot (\boldsymbol{\phi}^* Y^*) = \nabla^* \cdot \left(\frac{\rho^*}{\mathrm{Re}\,\mathrm{Sc}}\nabla^* Y^* + \alpha_d \frac{\rho^*}{\mathrm{Re}\,\mathrm{Sc}}\frac{Y_v(1-Y_v)}{Y_{v,H}-Y_{v,C}}\frac{\varepsilon_T}{1+\varepsilon_T T^*}\nabla^* T^*\right) \tag{3.29}$$

where

$$\boldsymbol{\tau}^*(\boldsymbol{U}^*) = \frac{1}{\mathrm{Re}}\left(\nabla^* \boldsymbol{U}^* + (\nabla^* \boldsymbol{U}^*)^T\right) - \frac{2}{3}\frac{1}{\mathrm{Re}}\nabla^* \cdot \boldsymbol{U}^* \boldsymbol{I} \tag{3.30}$$

and the thermodynamic pressure is

$$P_{\mathrm{th}}^* = m^* \left(\int_\Omega (1+\varepsilon_T T^*)^{-1}(1+\varepsilon_m Y^*)^{-1}\mathrm{d}V\right)^{-1} \tag{3.31}$$

subject to the following boundary conditions:

$$\begin{aligned} U_x^* &= U_{\text{wall},n}^* \quad x^* = 0,1 \\ U_y^* &= 0, \quad x^* = 0,1 \\ U_x^* &= 0, \quad y^* = 0,1 \\ U_y^* &= 0, \quad y^* = 0,1 \end{aligned} \tag{3.32}$$

and

$$\begin{aligned} T^* &= 0.5, \quad x^* = 0 \\ T^* &= -0.5, \quad x^* = 1 \\ Y^* &= 0.5, \quad x^* = 0 \\ Y^* &= -0.5, \quad x^* = 1 \end{aligned} \tag{3.33}$$

The first equation in (3.32) is due to the evaporation or condensation on the wall, which will be investigated in following section. It is obtained by supposing the air mass flux on the wall is zero.

Part of the interdiffusion term cancels with part of the advection term, so that the remaining contribution of interdiffusion is $\frac{1}{\text{Re}\,\text{Sc}}\frac{\Delta c_p}{c_{p,0}}\nabla^* \cdot (\rho^* T^* \nabla Y^*)$.

3.3.2 Definition of Nusselt and Sherwood number

The Nusselt number is the ratio of the heat flux non-dimensionalized by the (fictitious) heat flux due to conduction alone across the cavity: $k(T_H - T_C)/L$. It contains contributions due to: advection (a), diffusion (d), interdiffusion (with a mass flux effect which can be split into a diffusive part (id) and into a Soret effect (iS)), and Dufour effect (which can also be split into diffusive (Dd) and Soret (DS) effects). The total Nusselt number is therefore the sum of six components:

Hence, their local definitions are given as following:

$$\mathrm{Nu}_a = \mathrm{Re}\,\mathrm{Pr}\,\rho^* c_p^* \left(\frac{1}{\varepsilon_T} + T^*\right) \boldsymbol{U}^* \cdot \boldsymbol{e}_n \tag{3.34}$$

$$\mathrm{Nu}_d = -\nabla^* T^* \cdot \boldsymbol{e}_n \tag{3.35}$$

$$\mathrm{Nu}_{id} = -\frac{\mathrm{Pr}}{\mathrm{Sc}} \frac{\Delta c_p}{c_{p,0}} \left(\frac{1}{\varepsilon_T} + T^*\right) \rho^* \nabla^* Y^* \cdot \boldsymbol{e}_n \tag{3.36}$$

$$\mathrm{Nu}_{iS} = -\frac{\mathrm{Pr}}{\mathrm{Sc}} \frac{\Delta c_p}{c_{p,0}} \frac{Y_v(1-Y_v)}{Y_{v,H} - Y_{v,C}} \alpha_d \rho^* \nabla^* T^* \cdot \boldsymbol{e}_n \tag{3.37}$$

$$\mathrm{Nu}_{Dd} = -\frac{\mathrm{Pr}}{\mathrm{Sc}} \frac{\alpha_d R^2}{r c_{p,0} M_a M_v} \left(\frac{1}{\varepsilon_T} + T^*\right) \rho^* \nabla^* Y^* \cdot \boldsymbol{e}_n \tag{3.38}$$

$$\mathrm{Nu}_{DS} = -\frac{\mathrm{Pr}}{\mathrm{Sc}} \frac{\alpha_d^2 R^2}{r c_{p,0} M_a M_v} \frac{Y_v(1-Y_v)}{Y_{v,H} - Y_{v,C}} \rho^* \nabla^* T^* \cdot \boldsymbol{e}_n \tag{3.39}$$

In the same way, we define the Sherwood number to be the mass flux of vapour compared to the fictitious diffusion mass flux which is $\rho_0 D(Y_{v,H} - Y_{v,C})/L$. Thus, using dimensionless parameters, the different contributions to the Sherwood number, which are due to advection, diffusion and Soret effect, are identified as follows:

$$\mathrm{Sh}_a = \mathrm{Re}\,\mathrm{Sc}\,\rho^* \left(\frac{Y_{v,0}}{Y_{v,H} - Y_{v,C}} + Y^*\right) \boldsymbol{U}^* \cdot \boldsymbol{e}_n \tag{3.40}$$

$$\mathrm{Sh}_d = -\rho^* \nabla^* Y^* \cdot \boldsymbol{e}_n \tag{3.41}$$

$$\mathrm{Sh}_S = -\alpha_d \rho^* \frac{Y_v(1-Y_v)}{Y_{v,H} - Y_{v,C}} \frac{\varepsilon_T}{1 + \varepsilon_T T^*} \nabla^* T^* \cdot \boldsymbol{e}_n \tag{3.42}$$

In the following sections, we calculate the average values of the nondimensional heat and mass transfer along each vertical wall.

3.4 Numerical resolution

3.4.1 Definition of a velocity boundary condition

As seen in the previous section, the system is characterized by non-zero velocity boundary conditions given by Stefan's velocity (equation (3.20)) calculated from the vapour distribution at current time step. However, direct implementation of this boundary condition may cause instability of the algorithm.

Our solution to this problem is to build a decomposition of $\boldsymbol{U}$ as $\boldsymbol{U}_{\text{int}} + \boldsymbol{U}_b$, where $\boldsymbol{U}_{\text{int}} = 0$ on each wall (no matter if there is a phase change or not) and $\boldsymbol{U}_b$ is a partial velocity indicating the boundary condition of $\boldsymbol{U}$.

In the physical scenario we consider, there exists two types of walls: with or without phase changes.

- In the case of an adiabatic and impermeable wall, the boundary condition is $\boldsymbol{U} = 0$.
- In the case of a wall with evaporation or condensation, the normal velocity $U_n = \rho^{-1}(1 - Y_v)^{-1}\boldsymbol{j}_v \cdot \boldsymbol{e}_n$ (Stefan's velocity) and the tangential velocity $U_t = 0$, where the indexes n and t mean normal and tangential components. In our present case of a square cavity, $n = x$, $t = y$.

We consider the following splitting: $\boldsymbol{U} = \boldsymbol{U}_{\text{int}} + \boldsymbol{U}_b$, where $\boldsymbol{U}_b$ corresponds to the physical, non-homogeneous boundary conditions and $\boldsymbol{U}_{\text{int}}$ obeys homogeneous Dirichlet boundary conditions on the boundary. When the wall is adiabatic and no phase change occurs, $\boldsymbol{U}_{\text{int}} = \boldsymbol{U}$ and $\boldsymbol{U}_b = 0$. When phase changes occur on a wall characterized by a normal unity vector $\boldsymbol{e}_n$, one shall have $\boldsymbol{U}_b = (\rho^{-1}(1 - Y_v)^{-1}\boldsymbol{j}_v \cdot \boldsymbol{e}_n)\boldsymbol{e}_n$ and $\boldsymbol{U}_{\text{int}} = \boldsymbol{U} - \boldsymbol{U}_b$ on the wall.

One can define a phase-change factor f_k for each wall k so that we have for the bound-

ary condition velocity

$$\boldsymbol{U}_b = -\sum_k f_k(\rho^{-1}(1-Y_v)^{-1}\boldsymbol{j}_v \cdot \boldsymbol{e}_{n,k})\boldsymbol{e}_{n,k}.$$

f_k satisfies the following Dirichlet-type boundary conditions:

- if $\boldsymbol{x}$ is on the wall k and at the wall k phase changes occur, then $f_k(\boldsymbol{x}) = 1$;

- if $\boldsymbol{x}$ is on other walls or on the wall k and the wall k is adiabatic-impermeable, then $f_k(\boldsymbol{x}) = 0$.

We now have to define a value for f_k inside the domain. The simplest possible definition, which consists in taking $f_k = 0$ in the interior of the domain, is actually equivalent to the Stefan's-velocity-type boundary condition and causes the discontinuity of U_b . We therefore need f_k to be "smoother" and display some regularity properties.

An appropriate choice appears to be

$$\nabla^2 f_k = 0 \tag{3.43}$$

In practice, we solve the factors f_k at the initialization step of the algorithm.

The nondimensional air diffusive velocity writes:

$$\boldsymbol{U}^*_{a,d} = \frac{1}{\mathrm{Re}\,\mathrm{Sc}}\frac{Y_{v,H}-Y_{v,C}}{1-Y_v}\left(\nabla^* Y^* + \alpha_d \frac{Y_v(1-Y_v)}{Y_{v,H}-Y_{v,C}}\frac{\varepsilon_T}{1+\varepsilon_T T^*}\nabla^* T^*\right) \tag{3.44}$$

As a result, in the low Mach model, the equation (3.27) is replaced with

$$\begin{aligned}\frac{\partial}{\partial t^*}\left(\rho^* \boldsymbol{U}^*_{\text{int}}\right) + \nabla^* \cdot \left(\boldsymbol{\phi}^* \boldsymbol{U}^*_{\text{int}}\right) \;=\; & \nabla^* \cdot \boldsymbol{\tau}^*(\boldsymbol{U}^*_{\text{int}}) + \frac{\rho^* - 1}{\varepsilon_T + \varepsilon_m}\frac{\boldsymbol{g}}{\|g\|} - \nabla^* p^*_d \\ & - \left(\frac{\partial}{\partial t^*}\left(\rho^* \boldsymbol{U}^*_b\right) + \nabla^* \cdot \left(\boldsymbol{\phi}^* \boldsymbol{U}^*_b\right) - \nabla^* \cdot \boldsymbol{\tau}^*(\boldsymbol{U}^*_b)\right)\end{aligned} \tag{3.45}$$

and the system (3.26), (3.45), (3.28) and (3.29) is subject to the boundary conditions (3.33) and

$$U^*_{\text{int}} = 0, \quad x^* = 0, 1 \text{ or } y^* = 0, 1 \tag{3.46}$$

For the computation of $\boldsymbol{U}^*_{\text{int}}$ and p^*_d, we apply the Pressure Implicit Splitting of Operators (PISO) algorithm based on OpenFOAM framework, which is described in the Appendix C.

3.4.2 Adjustment of thermodynamic pressure

Mass conservation is enforced through a Poisson equation. In an incompressible system, the only way to keep the mass conservation is to balance the inlet and outlet of mass. However, in a low Mach system, mass can be adjusted in a constant volume by increasing or decreasing the density of the fluid. This corresponds to adjusting the thermodynamic pressure P_{th}.

In order to adjust P_{th} to enforce mass conservation we calculate first the mass flux $\frac{\mathrm{d}m^*}{\mathrm{d}t^*} = \int^*_\Omega \nabla^* \cdot \boldsymbol{\phi}^* \mathrm{d}V^*$ and thus we define at time $t^* + \Delta t^*$:

$$P^*_{\text{th}}(t^* + \Delta t^*) = \frac{m^*(t^*) + \frac{\mathrm{d}m^*}{\mathrm{d}t^*}\Delta t^*}{\int_{\Omega^*} \frac{1}{(1+\varepsilon_T T^*)(1+\varepsilon_m Y^*)}\mathrm{d}V^*} \tag{3.47}$$

This updated value $P^*_{\text{th}}(t + \Delta t)$ is used to calculate the physical parameters in the following iterations within the time step. Once the internal iteration is finished, the total

mass is updated by

$$m(t^* + \Delta t^*) = \frac{m_a^* \int_{\Omega^*} \frac{1}{(1+\varepsilon_T T^*)(1+\varepsilon_m Y^*)} \mathrm{d}V^*}{\int_{\Omega^*} \frac{1-Y_{v,0}-\Delta Y_v Y^*}{(1+\varepsilon_T T^*)(1+\varepsilon_m Y^*)} \mathrm{d}V^*} \tag{3.48}$$

where we use the fact that the air mass is constant.

3.5 Validation and comparisons

3.5.1 Pure thermal convection validation

We first validate our model on a pure natural convection case, corresponding to to $Y_{v,H} = Y_{v,C} = 0$). Natural convection of air in a two-dimensional square cavity has been extensively studied. Two models have been used. When the temperature variation is assumed to be small, one typically applies Boussinesq's approximation [De Vahl Davis, 1983a,b]. The variation of density by dilatation is only considered in the buoyancy term appearing in the momentum conservation equations and the flow is otherwise assumed to be incompressible. As a consequence, the temperature, velocity and pressure fields in the cavity obey centro-symmetric (or anti-centro-symmetric) properties.

In order to deal with higher temperature differences, the low Mach model has to be introduced. Low Mach model allows variation of density and thermodynamic pressure. A benchmark problem has been proposed with high temperature difference ($\varepsilon_T = 1.2$) [Vierendeels et al., 1999; Le Quéré et al., 2005; Paillère, 2005] It was found that the solution of the Low Mach model is not centro-symmetric for large temperature differences. Here we compare calculation results of current model with Virendeels' results, which were obtained with an advection upstream splitting method (AUSM) with constant properties [Vierendeels et al., 1999].

Case	Ra	Pr	Sc	M_a	M_v	γ_a	γ_v	T_H	T_C	$Y_{v,H}$	$Y_{v,C}$	α_d
t1	10^6	0.71	—	29	—	1.4	—	480	120	0	0	0
w1	10^5	1	1	20	100	1.4	1.056	320.85	283.15	0.3	0	0
w0	10^5	1	1	20	100	1.4	1.4	320.85	283.15	0.3	0	0
s1	5.63×10^6	0.71	0.71	29	7.25	1.4	1.4	352	288	0.074	0	0
e1	4.05×10^5	1.32	0.66	29	18	1.4	1.29	393.15	353.15	0.29	0.06	0
e2	4.05×10^5	1.32	0.66	29	18	1.4	1.29	393.15	353.15	0.29	0.06	-0.0059
e3	4.05×10^5	1.32	0.66	29	18	1.4	1.29	393.15	353.15	0.29	0.06	0.4

Table 3.2: Values of parameters in different cases computed in this paper (M_a and M_v are in g/mol, T_H and T_C are in K); initial condition of each case is $T^* = 0$ and $Y^* = 0$ apart from s1 where initially $T^* = -0.5$ and $Y^* = -0.5$.

Mesh	40×40	80×80	160×160	320×320	ref.
P_{th}	0.8539	0.8557	0.8562	0.8563	0.856338
$\overline{\text{Nu}_H}$	8.9028	8.8737	8.8636	8.8608	8.85978
$\overline{\text{Nu}_C}$	8.8708	8.8690	8.8630	8.8607	8.85978

Table 3.3: Validation from benchmark of natural convection with large temperature difference (case t1), reference solution (ref.) given by Virendeels [Vierendeels et al., 1999] and established as reference in [Paillère, 2005] with a mesh of 2048×2048.

The input data correspond to test T1 in [Paillère, 2005] which we call case t1 in TAB. 3.2. In order to establish convergence, calculations with meshes of different sizes were performed. The mesh size varies from 40×40 to 320×320. Results are shown in TAB. 3.3.

TAB. 3.3 shows that the value of P_{th} approaches the reference result within less than 0.1% for a mesh of 80×80. The Nusselt number is close to less than 0.5% of difference for a mesh of 160×160. All results presented in the remainder of this chapter are computed using a mesh of 320×320.

3.5.2 Heat and mass transfer under nearly constant thermodynamic pressure

Case description

We now validate our model for a double-diffusive heat and mass transfer case, which was considered by Weaver and Viskanta in [Weaver and Viskanta, 1991a] (case w_1 in the table). In Weaver and Viskanta's model, the thermodynamic pressure is *a priori* supposed to be constant (as in the Boussinesq approximation). However, unlike Boussinesq's model, variation of physical properties (density and specific heat capacity) is allowed. Moreover, in both heat transport and mass transport equations, only diffusion and advection are taken into account. This physical model is called the double-diffusive model. Species

interdiffusion is therefore not taken into account in heat transfer.

In our calculation, we first neglect the interdiffusion term together with Soret and Dufour effects which makes our model similar to Weaver and Viskanta's approach (double-diffusive case). However, we stress out that our model always allows the thermodynamic pressure to vary whereas it is fixed in Weaver and Viskanta's model. We then compare the results with our model when interdiffusion is taken into account.

Comparison of results

In TAB. 3.4, a comparaison based on case w1 (defined in TAB. 3.2) is shown between the reference result from [Weaver and Viskanta, 1991a] and our calculation results with double diffusion model and the full model with species interdiffusion (but without Soret and Dufour effect). γ_v is set to 1.0559 in order to match the condition $h_v/h_a = 1.08$ in [Weaver and Viskanta, 1991a].

First of all, we observe that P_{th}^* in both double diffusive and full model calculations are close to 1 and vary extremely slightly, which validates *a posteriori* Weaver and Viskanta's hypothesis of constant pressure.

A good agreement is found for the diffusive mass flux between the reference and the double-diffusive results. Both convective and diffusive heat fluxes are also well estimated with less than 2% of relative difference.

As a result of the energy conservation, total heat fluxes at the hot and cold walls should be equal at steady state. However, in both reference result and current double-diffusive calculation where mesh convergence has already been reached, there is still a difference between the total heat fluxes on each side.

Adding the interdiffusion effect in the system (`full`) leads to a slight change in the

	ref.	dd	full
P^*_{th}	1.0000	1.0074	1.0078
		left	
$\overline{\text{Sh}_a}$	—	1.69	1.69
$\overline{\text{Sh}_d}$	3.97	3.94	3.94
$\overline{\text{Sh}}$	—	5.63	5.63
$\overline{\text{Nu}_a}$	14.45	14.55	14.55
$\overline{\text{Nu}_d}$	3.97	3.90	3.85
$\overline{\text{Nu}_i}$	—	—	0.80
$\overline{\text{Nu}}$	18.42	18.44	19.20
		right	
$\overline{\text{Sh}_a}$	—	0.00	0.00
$\overline{\text{Sh}_d}$	5.69	5.63	5.63
$\overline{\text{Sh}}$	—	5.63	5.63
$\overline{\text{Nu}_a}$	12.81	12.54	12.54
$\overline{\text{Nu}_d}$	5.69	5.58	5.65
$\overline{\text{Nu}_i}$	—	—	1.00
$\overline{\text{Nu}}$	18.51	18.12	19.20

Table 3.4: Results for case w1: reference result from [Weaver and Viskanta, 1991a] which uses a mesh of 55×55 (`ref.`) and our calculations with double-diffusive model (`dd`) and low-Mach model with interdiffusion (`full`) both using a mesh of 320×320.

diffusion heat fluxes, and more importantly, to small but non-negliglible interdiffusion heat fluxes. The total heat fluxes on each wall are then equal when interdiffusion effects are accounted for. It should be pointed out that for this case interdiffusion is small because of the small specific heat capacity difference of two components ($c_{p,v}/c_{p,a} = 1.08$).

Larger specific heat capacity difference

To examine the relative weight of species interdiffusion heat flux, the specific heat capacity difference should be large enough. Here we consider the same case as above but set $\gamma_v = \gamma_a = 1.4$ (case w0 in TAB. 3.2). As in the previous case we carry out two low-Mach calculations: the double-diffusive model (`dd`) and the model with interdiffusion (`full`).

In this case, $c_{p,v}/c_{p,a} = 0.2$, which represents a significant difference in the heat capacities. As a result, we do observe not only a significant interdiffusion heat flux in full model

	dd	full
P^*_{th}	1.0077	1.0040
	left	
$\overline{\text{Sh}_a}$	1.69	1.68
$\overline{\text{Sh}_d}$	3.94	3.93
$\overline{\text{Sh}}$	5.63	5.61
$\overline{\text{Nu}_a}$	12.40	12.36
$\overline{\text{Nu}_d}$	3.93	4.45
$\overline{\text{Nu}_i}$	—	-9.11
$\overline{\text{Nu}}$	16.33	7.71
	right	
$\overline{\text{Sh}_a}$	0.00	0.00
$\overline{\text{Sh}_d}$	5.62	5.60
$\overline{\text{Sh}}$	5.62	5.60
$\overline{\text{Nu}_a}$	14.40	14.35
$\overline{\text{Nu}_d}$	5.61	4.84
$\overline{\text{Nu}_i}$	—	-11.48
$\overline{\text{Nu}}$	20.01	7.70

Table 3.5: Results for case w0: calculations with double-diffusive model (`dd`) and low-Mach model with interdiffusion (`full`)

but also an obvious non-equilibrium of total heat fluxes.

From TAB. 3.5 we can see that the prediction of the mass transfer is the same for the two models. Though differences between advection heat fluxes and differences between thermodynamic pressures are slight, the addition of interdiffusion significantly modifies the diffusion heat fluxes. The interdiffusion heat fluxes, which are negative here because $c_{p,v} < c_{p,a}$, contribute greatly to the total heat transfer. It is also observed that the equality of the total heat fluxes on each wall is not enforced in the double-diffusive calculation while it is the case in the full model calculation, which guarantees energy conservation.

3.5.3 Heat and mass transfer under large thermodynamic pressure variation

In the last validation case, the low Mach approximation is applied to the double-diffusive model described in the work of Sun and Lauriat [Sun et al., 2010] in 2010. In their study, a case of large thermodynamic pressure variation is examined.

Case description

Since the dimensionless heat transport equation in the double-diffusive model can be written in conservative form, conservative heat fluxes may be reconstructed. In their paper [Sun et al., 2010], the definition of the Sherwood and Nusselt numbers are given by such reconstruction, which shall be translated in our notations as:

$$\mathrm{Sh} = \mathrm{Re}\,\mathrm{Sc}\,\rho^* Y^* \boldsymbol{U}^* \cdot \boldsymbol{e}_n - \rho^* \nabla^* Y^* \cdot \boldsymbol{e}_n \tag{3.49}$$

$$\mathrm{Nu} = \mathrm{Re}\,\mathrm{Pr}\,\rho^* T^* \boldsymbol{U}^* \cdot \boldsymbol{e}_n - \rho^* \nabla^* T^* \cdot \boldsymbol{e}_n \tag{3.50}$$

It is clear that these definitions, which will be called the reconstructed definitions in the following to be differentiated from the physical definitions, do not take into account neither the reference mass fraction nor the reference temperature in advection and therefore are not equivalent to the physical definitions of advection Sherwood and Nusselt number (Eq. 3.40, 3.34).

The transport properties of case 1 in Table 5 in [Sun et al., 2010] correspond to case s1 in TAB. 3.2. In addition, in the initial conditions, the dimensionless temperature and concentration are set to be -0.5 in order to reinforce the evaporation and to increase the thermodynamic pressure variation. Since the amount of steam in the cavity is expected to increase from its initial value, the thermodynamic pressure is supposed to be bigger than

	ref.	ddR	dd	full
P_{th}^{*}	1.255	1.257	1.257	1.261
		left		
$\overline{Sh_a}$	—	0.71	1.42	1.41
$\overline{Sh_d}$	—	17.72	17.72	17.72
$\overline{Sh}$	18.40	18.43	19.13	19.13
$\overline{Nu_a}$	—	0.78	8.56	8.56
$\overline{Nu_d}$	—	15.53	15.53	13.88
$\overline{Nu_i}$	—	—	—	19.46
$\overline{Nu}$	16.34	16.31	24.09	41.90
		right		
$\overline{Sh_a}$	—	-0.71	0.00	0.00
$\overline{Sh_d}$	—	19.12	19.12	19.12
$\overline{Sh}$	18.40	18.42	19.12	19.12
$\overline{Nu_a}$	—	-0.64	5.73	5.73
$\overline{Nu_d}$	—	16.93	16.93	18.93
$\overline{Nu_i}$	—	—	—	17.20
$\overline{Nu}$	16.34	16.30	22.67	41.86

Table 3.6: Results for case s1: reference from [Sun et al., 2010] (`ref.`) using a 512×512 mesh, double-diffusive calculation post-treated with reconstructed definitions (`ddR`) and with physical definitions (`dd`) and full model with interdiffusion with physical definitions (`full`), all of the last 3 results use a 320×320 mesh

1.

Results

TAB. 3.6 compares results from the reference [Sun et al., 2010] with results from the double-diffusive approach, using equivalent (incorrect) reconstructed fluxes (ddR). Correct fluxes for the double-diffusive approach were also computed (dd) and can be confronted with those obtained for the full model (full). One first notices that the reference result and the double diffusive result with reconstructed post-treatment are in very good agreement. This validates our low-Mach calculation without species interdiffusion.

Comparison of specific contributions for the two double-diffusive cases, which are based on the same calculation, illustrates the difference in the definition of the Nusselt

numbers. While the contributions to diffusion are the same, the advective contributions are totally different. Since the reconstructed definitions do not take into account the reference values, it is possible to obtain negative values on the cold wall as the two dimensionless fields take negative values there. The double-diffusive case with the correct definition does not lead to matching Nusselt numbers on each side of the cavity.

In contrast, our calculation with our full model accounting for species interdiffusion leads to equal Nusselt numbers on each side. Since the specific heat capacity difference is large ($c_{p,v}/c_{p,a} = 4$), interdiffusion heat fluxes make a major contribution to the total heat transfer (46.50% of the total heat flux on the hot wall and 41.10% on the cold wall).

FIG. 3.2 compares the fields T^* and Y^* calculated using the two models. FIG. (3.2b) and (3.2d) show that the concentration field is not significantly modified. FIG. (F.1a) and (F.1b) show that the gas mixture is globally hotter in full model than in double diffusive model, which is confirmed by the comparison of thermodynamic pressure in TAB. 3.6. More specifically, we see that with interdiffusion, the cold tongue on the hot wall is stronger, thus we have a stronger gradient on the hot wall and the the hot tongue on the cold wall is weaker thus the gradient is weaker on the cold wall. This fact is also verified with the comparison of diffusive Nusselt numbers of each case on each wall.

In particular, the fluid is hotter in the top portion of the cavity and less cold in the bottom portion compared with the double diffusive model. As a result, the upper hot fluid gets closer to the cold wall in the full model, which results in a greater temperature gradient and higher diffusion heat flux. Similarly, the thermal diffusion flux is lower at the hot wall in the full model than in the double diffusive model because of the reduced extent of the cold intrusion.

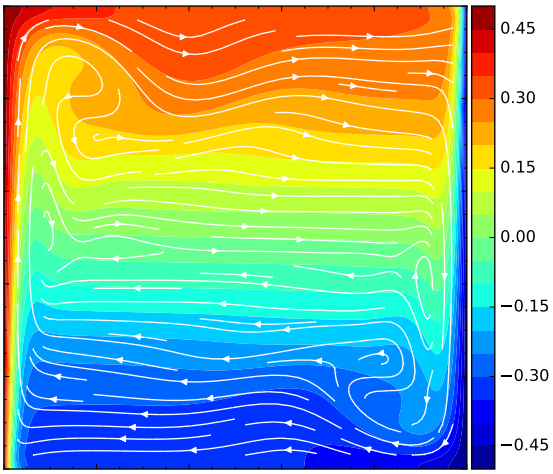

(a) T^* using the double-diffusive approach `dd`

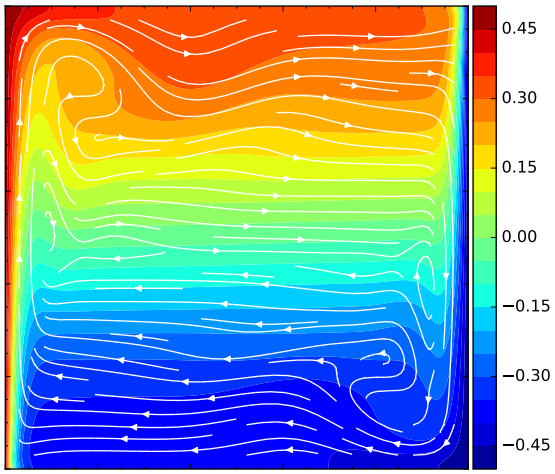

(b) Y^* using the double-diffusive approach `dd`

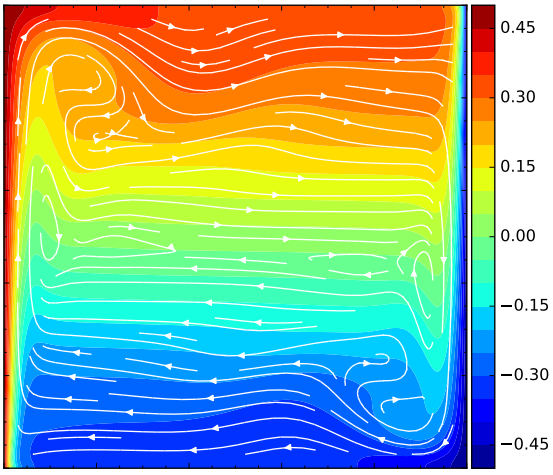

(c) T^* using the full model `full`

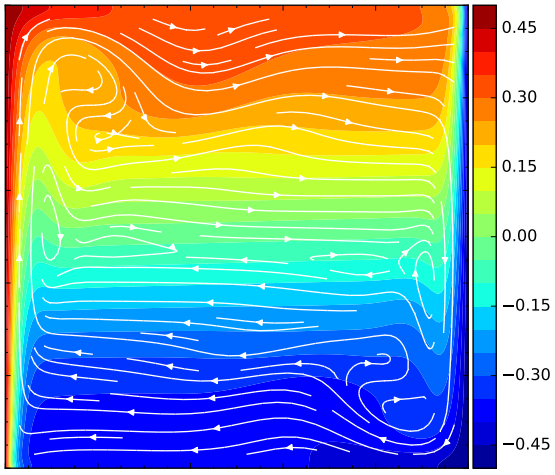

(d) Y^* using the full model `full`

Figure 3.2: Illustrations of dimensionless fields T^* and Y^* with the streamlines of velocity field of the calculation results of the case s1 using `dd` and `full` models.

3.5.4 Conclusions of the validation

We have investigated three cases with different natures: pure heat transfer with high temperature difference, simultaneous heat and mass transfer with slight thermodynamic pressure variation and simultaneous heat and mass transfer with large thermodynamic pressure variation.

A striking result is that in the two last cases, the double-diffusive model fails to guarantee energy conservation and it is necessary to account for species interdiffusion in order to enforce conservation.

3.6 Calculations for air and steam mixture

Since the current model is validated for simultaneous heat and mass transfer, we investigate the influence of species interdiffusion together with Soret effect and Dufour effect.

We now consider a square cavity, side length of which is 2 cm, with an initial pressure of 5 bar. The Rayleigh number for this case is $\mathrm{Ra} = 4.05 \times 10^5$. We take $\mathrm{Pr} = 1.32$ and $\mathrm{Sc} = 0.66$. The temperature of the hot wall is $T_H = 120\ ^\circ\mathrm{C}$ and that of the cold wall is $T_C = 80\ ^\circ\mathrm{C}$. Assuming the steam is saturated on both walls, we take $Y_{v,H} = 0.29$ and $Y_{v,C} = 0.06$. The initial state of the interior is set as the reference state.

3.6.1 Values of the thermal diffusion ratio

The intensity of Soret and Dufour effects is a function of the thermal diffusion ratio α_d, which depends on the composition of mixture, but is approximately independent to temperature and concentration of components [Bird et al., 2006].

When $\alpha_d = 0$, all the terms due to Soret and Dufour effects are canceled. We therefore use this value to set up a reference result without Soret and Dufour effects, which is denoted as case e1 in TAB. 3.2.

According to [Monchick and Mason, 1961; Mason, 1957], a realistic value $\alpha_d = -0.0059$ is found for the air-steam mixture and it is applied for the case e2. In [Bird et al., 2006], we find that α_d can reach 0.4 in a mixture of $Ne - He$ or $N_2 - H_2$. This value is applied for the case e3 in order to assess to a maximal influence of Soret and Dufour effects.

Consequently, we consider the following values of α_d in the calculations: 0 (e1), -0.0059 (e2), 0.4 (e3).

3.6.2 Results

First of all, according to comparison between the results of e1 and e2 (TAB. 3.7), the influence of Soret and Dufour effects remains slight with $\alpha_d = -0.0059$. The mass fluxes are mostly the same in the two cases and the Soret effect is negligible in the case e2. The heat fluxes are pratically not affected by the Dufour effect heat flux, which is negligible compared to the total heat flux. However, the Dufour effect shows a more important contribution to the total heat transfer (-0.31% / -0.42%) compared to that of Soret effect to the total mass transfer (-0.04% / -0.03%).

In the case e3, Soret and Dufour effects are amplified. A large difference with the case e1 ($\alpha_d = 0$) is observed for both mass and heat transfer. Compared to e1, e3 shows that a positive α_d may intensify the mass transfer and the evaporation-condensation rate (see the comparison of $\overline{Sh_a}$).

It is also necessary to point out that for this case the Dufour effect contributes significantly to the total heat transfer. However the Soret effect does not contribute a lot to the mass transfer even with a rather large value of α_d.

case	e1	e2	e3
α_d	0	-0.0059	0.4
P^*_{th}	0.9988	0.9989	0.9915
		hot wall	
$\overline{\text{Sh}_a}$	1.85	1.85	2.05
$\overline{\text{Sh}_d}$	4.53	4.52	4.93
$\overline{\text{Sh}_S}$	0.00	0.00	0.08
$\overline{\text{Sh}}$	6.38	6.36	7.06
$\overline{\text{Nu}_a}$	31.65	31.57	35.04
$\overline{\text{Nu}_d}$	5.03	5.08	2.49
$\overline{\text{Nu}_{id}}$	18.05	18.01	19.66
$\overline{\text{Nu}_{iS}}$	0.00	-0.01	0.32
$\overline{\text{Nu}_{Dd}}$	0.00	-0.17	12.80
$\overline{\text{Nu}_{DS}}$	0.00	0.00	0.21
$\overline{\text{Nu}}$	54.73	54.47	70.52
		cold wall	
$\overline{\text{Sh}_a}$	0.39	0.39	0.43
$\overline{\text{Sh}_d}$	5.99	5.97	6.58
$\overline{\text{Sh}_S}$	0.00	0.00	0.05
$\overline{\text{Sh}}$	6.38	6.36	7.06
$\overline{\text{Nu}_a}$	23.20	23.13	25.68
$\overline{\text{Nu}_d}$	10.07	10.17	3.55
$\overline{\text{Nu}_{id}}$	21.45	21.40	23.59
$\overline{\text{Nu}_{iS}}$	0.00	-0.01	0.16
$\overline{\text{Nu}_{Dd}}$	0.00	-0.23	17.43
$\overline{\text{Nu}_{DS}}$	0.00	0.00	0.12
$\overline{\text{Nu}}$	54.72	54.46	70.53

Table 3.7: Comparison of results of the air-steam tests with different α_d (e1, e2, e3), using a mesh of 320×320

In FIG. 3.3, (3.3c) and (3.3d) show the distribution of the temperature and the concentration fields in the cavity along the velocity streamlines. No visible difference is observed between cases e1 (3.3a and 3.3b) and e2 (3.3c and 3.3d), which agrees with the results in TAB. 3.7.

FIG. 3.3e and 3.3f show that the fluid is hotter and less rich in steam in the top portion while it is colder and richer in steam in the bottom portion. Moreover, the thermal boundary layers appear to be thicker on both vertical walls in FIG. 3.3e, which is consistent with the reduced diffusion fluxes noted in TAB. 3.7. It is also observed that the velocity field is characterized by larger recirculation zones.

3.7 Conclusion of the chapter

In this chapter, we have presented a low Mach number model for the binary mixture of condensable and non-condensable gases with constant thermophysical properties. The model was applied to the case of a two-dimensional, differentially heated square cavity in the laminar regime. A boundary condition treatment strategy based on the air partial velocity was implemented in the solver and was found to improve the robustness of the PISO algorithm. Application of the model for different test cases showed that the contribution of interdiffusion to the Nusselt number was significant on both side walls of the cavity. Consideration of species interdiffusion is therefore essential to guarantee the energy conservation in the domain. The influence of Soret and Dufour effects was also examined. For a mixture of air and vapour, we established that these two effects are negligible. However, we found that Dufour effects may become important when the thermal diffusion ratio gets sufficiently large.

Now that we have developed a model for laminar flow, we focus on turbulent effects, which are generally present in a real-life configuration.

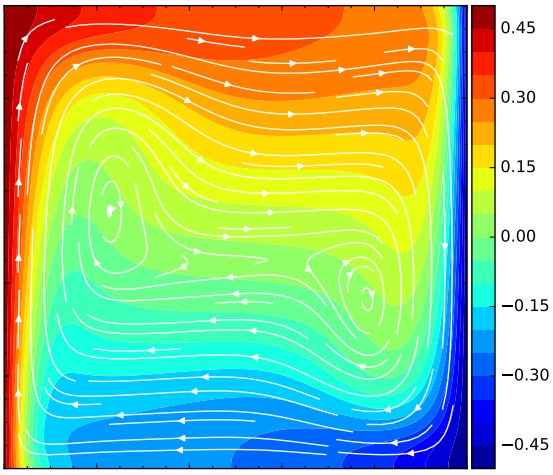

(a) T^* for the case e1 ($\alpha_d = 0$)

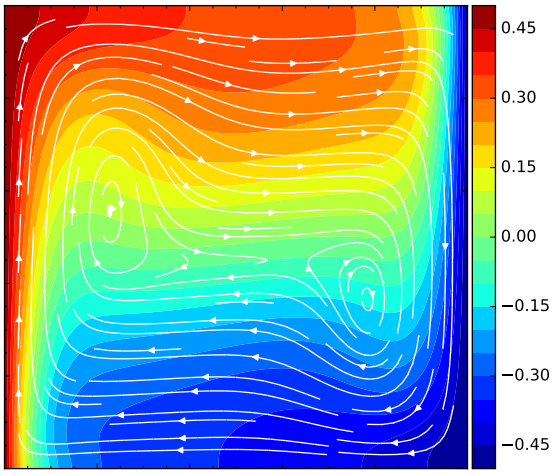

(b) Y^* for the case e1 ($\alpha_d = 0$)

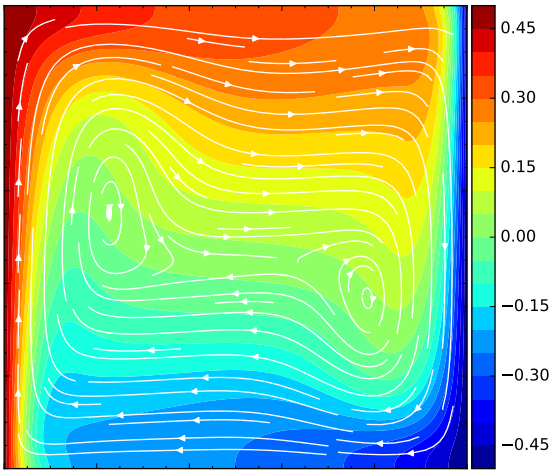

(c) T^* for e2($\alpha_d = -0.0059$)

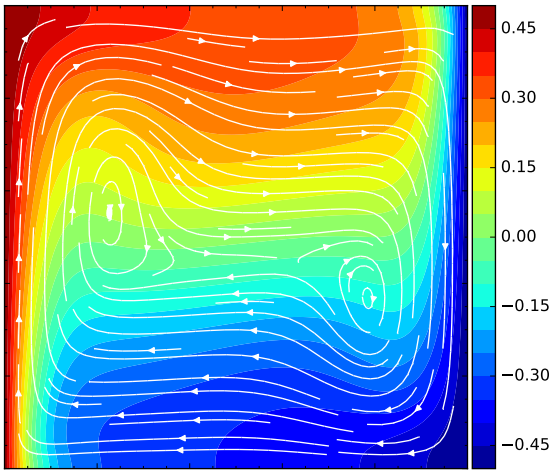

(d) Y^* for the case e2 ($\alpha_d = -0.0059$)

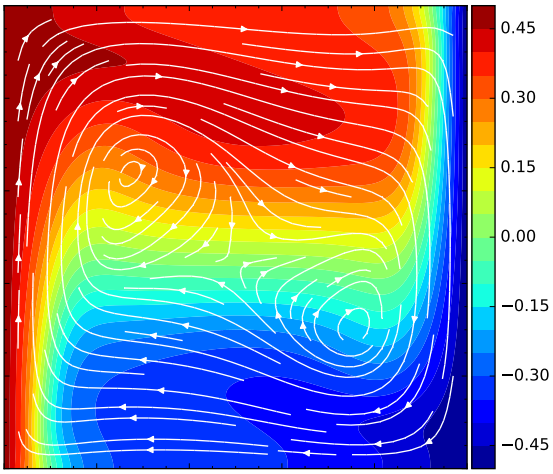

(e) T^* for the case e3

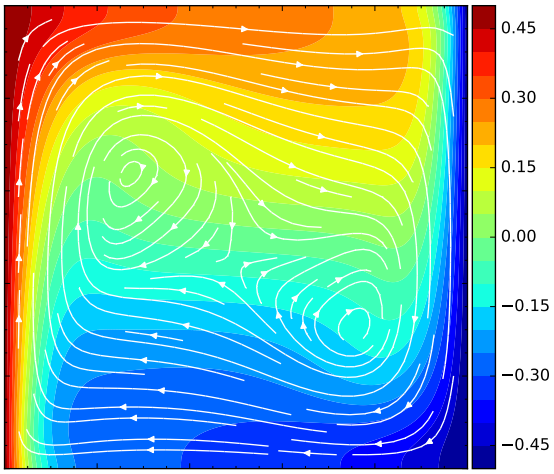

(f) Y^* for the case e3 ($\alpha_d = 0.4$)

Figure 3.3: Illustrations of dimensionless fields T^* and Y^* with the streamlines of velocity field of the calculation results of e2($\alpha_d = -0.0059$) and e3 ($\alpha_d = 0.4$).

Chapter 4

Low Reynolds turbulence models for filmwise condensation

In this chapter, we will detail the low Reynolds number turbulence model that we use in our numerical simulations. Then, we conduct a verification process of this model using test cases of increasing complexity. The first one concerns a dynamic turbulent boundary layer simulated in direct numerical simulation. The second one adds the suction effect from experimental data. The last one ends with the heat and mass transport effect in condensation with the COPAIN experimental data.

4.1 The low Reynolds number turbulence model

In this thesis, for low Reynolds number turbulence models, we follow the approach of [Patel et al., 1985] [Launder and Sharma, 1974] [Chien, 1982] [Jones and Launder, 1972] [Sarkar and So, 1997] considering a weakly compressible flow and using the concept of

eddy viscosity for which the Reynolds tensor is written:

$$-\widetilde{\rho u_\alpha'' u_\beta''} = 2\mu_t \left(\frac{\partial U_\alpha}{\partial x_\beta} + \frac{\partial U_\beta}{\partial x_\alpha} \right) - \frac{2}{3}\rho k \delta_{\alpha\beta} - \frac{2}{3}\mu_t \frac{\partial U_\gamma}{\partial x_\gamma}\delta_{\alpha\beta} \tag{4.1}$$

and the eddy viscosity:

$$\mu_t = C_\mu f_\mu \rho \frac{k^2}{\epsilon}. \tag{4.2}$$

We restrict our analysis to models with two $k-\epsilon$ equations and consider the following system of equations for all these models:

$$\rho \frac{\partial k}{\partial t} + \rho \mathbf{U}\boldsymbol{\nabla} \cdot k = \nabla \left(\left(\mu + \frac{\mu_t}{\sigma_k} \right) \boldsymbol{\nabla} \cdot k \right) + P_k - \rho\epsilon + \xi \tag{4.3}$$

$$\rho \frac{\partial \epsilon}{\partial t} + \rho \mathbf{U}\boldsymbol{\nabla} \cdot \epsilon = \nabla \left(\left(\mu + \frac{\mu_t}{\sigma_\epsilon} \right) \boldsymbol{\nabla} \cdot \epsilon \right) + C_{\epsilon,1} f_1 \frac{1}{T_t} P_k - C_{\epsilon,2} f_2 \rho \frac{\hat{\epsilon}}{T_t} + \phi. \tag{4.4}$$

The different terms involved in these equations are described in TAB. 4.1 and 4.2 for the most classical models (CH [Chien, 1982], LB [Lam and Bremhorst, 1981], LS [Launder and Sharma, 1974] YS [Shih and Yang, 1993]). We have added the wall condition for the dissipation of turbulent kinetic energy ϵ_w. Apart from y^+ already defined, we have to introduce the wall Reynolds number $\mathrm{Re}_y = \sqrt{k}y/\nu$ and the turbulent Reynolds number $\mathrm{Re}_t = k^2/\nu\epsilon$.

In addition, the definition of the turbulence production term P_k is written in three dimensions:

$$\begin{aligned} P_k \;=\; & \mu_t \left[2\left(\frac{\partial u}{\partial x}\right)^2 + 2\left(\frac{\partial v}{\partial y}\right)^2 + 2\left(\frac{\partial w}{\partial z}\right)^2 \right. \\ & \left. + \left(\frac{\partial u}{\partial y} + \frac{\partial v}{\partial z}\right)^2 + \left(\frac{\partial u}{\partial z} + \frac{\partial w}{\partial x}\right)^2 + \left(\frac{\partial v}{\partial z} + \frac{\partial w}{\partial y}\right)^2 \right] \\ & -\frac{2}{3}\mu_t \left(\boldsymbol{\nabla} \cdot \mathbf{u}\right)^2 - \frac{2}{3}\rho k \left(\boldsymbol{\nabla} \cdot \mathbf{u}\right) \end{aligned}$$

In his paper, Sarkar [Sarkar and So, 1997] conducts a detailed analysis of different low-

Name	C_μ	f_μ	σ_k	ξ	σ_ϵ	$C_{\epsilon,1}$
CH	0.09	$1-\exp(-0.0115\,y^+)$	1.0	$-2\mu k/y^2$	1.3	1.35
LB	0.09	$[1-\exp(-0.0165\mathrm{Re}_y)]\times\left(1+\frac{20.5}{\mathrm{Re}_t}\right)$	1.0	0	1.3	1.44
LS	0.09	$\exp\left(-\frac{3.4}{\left(1+\mathrm{Re}_{t/50}\right)^2}\right)$	1.0	$-2\mu\left(\frac{\partial\sqrt{k}}{\partial y}\right)^2$	1.3	1.44
YS	0.09	$\sqrt{1-\exp\left[-\left(1.5\times10^{-4}\mathrm{Re}_y+5\times10^{-7}\mathrm{Re}_y^3+1\times10^{-10}\mathrm{Re}_y^5\right)\right]}$	1.0	0	1.3	1.44

Table 4.1: Low Reynolds number turbulence models: Description

Name	f_1	T_t	$C_{\epsilon,2}$	f_2	$\hat{\epsilon}$	ϕ	ϵ_w
CH	1	k/ϵ	1.8	$1-0.3\exp\left[-\left(\mathrm{Re}_t/6\right)^2\right]$	ϵ	$2\mu\epsilon\exp\left(-y^+/2\right)/y^2$	0
LB	$1+\left(0.05/f_\mu\right)^3$	k/ϵ	1.92	$1-\exp\left[-\left(\mathrm{Re}_t\right)^2\right]$	ϵ	0	$\mu\left(\frac{\partial^2 k}{\partial y^2}\right)_w$
LS	1	k/ϵ	1.92	$1-0.3\exp\left[-\left(\mathrm{Re}_t\right)^2\right]$	ϵ	$2\nu\mu_t\left(\frac{\partial^2 U}{\partial y^2}\right)^2$	0
YS	1	$k/\epsilon+\sqrt{\nu/\epsilon}$	1.92	1.0	ϵ	$\nu\mu_t\left(\frac{\partial^2 U}{\partial y^2}\right)^2$	$2\mu\left(\frac{\partial\sqrt{k}}{\partial y}\right)_w^2$

Table 4.2: Low Reynolds number turbulence models: Description (continued)

Reynolds turbulence models for the treatment of turbulent flows with walls. He concludes that the main quality of the model must be its accurate asymptotic behaviour in the near wall. This behaviour for the main variables has been studied in detail in [Patel et al., 1985] and is recalled in TAB. 4.3.

Variable	k	ϵ	$\epsilon - \phi$	ν_t	$\overline{u'_\alpha u'_\beta}/k$	P_k/ϵ
Comportement	$O(y^2)$	$O(1)$	$O(y^2)$	$O(y^2)$	$O(y)$	$O(y^3)$

Table 4.3: Asymptotic behaviour of the main variables in the near wall (y normal distance to the wall).

In Patel's studies, there were no clear conclusions about the performance of the LS, CH and LB models, but the latter had the advantage of giving the best asymptotic results. From Sarkar's analysis, it appears that for the channel calculations compared to DNS results:

- On the $k^+ = k/u_\tau^2$ profile, the YS model has a good behaviour whereas LS shows bad results in the inner zone ($y^+ < 60$) and CH finds it difficult to find results close to the central zone of the channel.
- On the ε^+ profile, all models behave well above $y^+ = 25$. However, below this, only the YS model performs well.
- On the U^+ profile, the recalculation of the Von-Karman constant κ gives errors of more than 30% for the LS and CH models.
- On the f_μ profile, only the YS model shows a good behaviour, LS tends to grow too fast while CH grows too slowly.

In 2008, Bucci et al. [Bucci et al., 2008] conducted an analysis of different low Reynolds number turbulence models to deal with wall condensation. From their analysis, it emerges that two models out of the five studied show satisfactory behaviour, that of YS and that of Abe et al [Abe et al., 1994].

In this context, it is not straightforward to select a relevant model to all issues. We propose to use two available models to conduct our analyses:

- the low-Reynolds turbulence model of Chien (CH) implemented in the CAST3M [Cast3M, 2019] platform of the CEA with the NLIN operator. The chosen discretization is based on quadratic finite elements for velocities and scalars and linear finite elements for pressure. The steady state is obtained as an asymptotic limit of a transient for which the residuals on all variables are lower than a threshold set at 10^{-8}. The model also includes two turbulence limiters:
  1. the production P_k of local turbulence is limited to ten times the turbulent dissipation ε.
  2. the turbulent kinetic energy is limited near the stagnation points [Durbin, 2009] [Park and Park, 2005].
- the Launder-Sharma model (LS) available in the OpenFOAM software tool.

Before dealing with wall condensation, we have applied these models to increasingly complex cases. First, we treat a turbulent boundary layer from the DNS work of Mansour et al. [Mansour et al., 1988]. Then, the effect of suction, which is an important part of wall condensation, is studied separately with the experiments of Favre et al. [Favre et al., 1966]. Finally, the calculations of COPAIN filmwise condensation experiments [Bazin and Castelli, 2000] with local measurements are performed. This last point is only addressed with the CH model.

4.2 Channel Flow

The first validation of our models was done against a direct numerical simulation (DNS) calculation described in [Moser et al., 1999]. This is a fully developed turbulent flow in a 2D

plane channel. We have selected the case where the Reynolds number Re_τ, calculated from the friction velocity u_τ, has the value 395.

To address this case with our models, the mesh and boundary conditions are shown in FIG. 4.1. The pressure difference $\Delta P = P_{up} - P_{down}$ has been iteratively adjusted to obtain the correct Reynolds number Re_τ. The geometrical data are as follows: width of the half channel $y = 0.5$ m, height of the channel $x = 0.2$ m (two meshes in the height are sufficient) and size of the first mesh 0.2 mm. The fluid is air at ambient pressure and temperature and the driving pressure is $\Delta P = 7.10^{-5}$ Pa.

The calculations were performed on different meshes until convergence. From a minimum value of y^+ of 0.1, the calculations are converged.

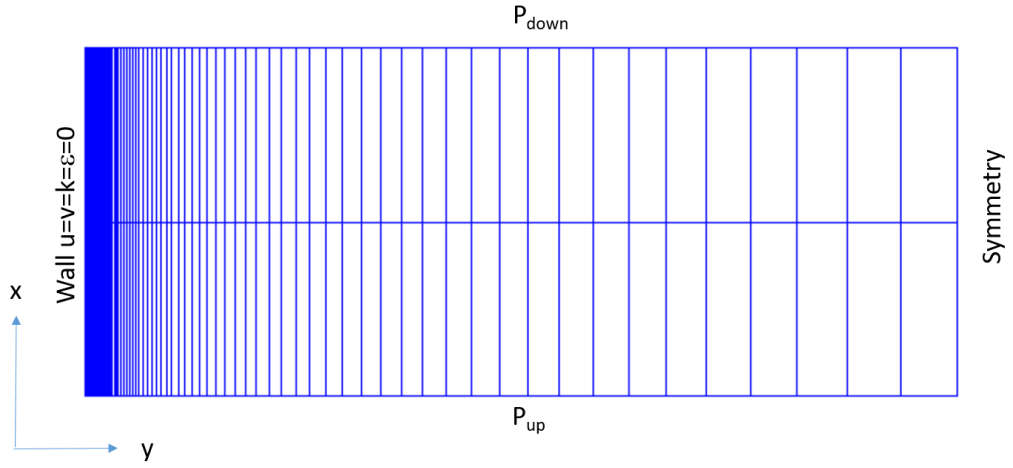

Figure 4.1: Mesh size and boundary conditions for the [Moser et al., 1999].

For the comparison between the calculations and the DNS data [Yang et al., 1991] [Hwang and Lin, 1998], we look at the profiles of four dimensionless quantities:

- the turbulent kinetic energy $k^+ = k/u_\tau^2$;
- the turbulent dissipation $\varepsilon^+ = \nu/u_\tau^4$;
- the velocity $U^+ = U/u_\tau$;

- the damping function of the viscosity f_μ.

The results are presented in FIG. 4.2. They are in accordance with what the literature reports on this calculation case, namely, the too slow decay of the damping function f_μ, the wall condition on ε which is forced to 0 using the variable $\hat{\epsilon}$ while the DNS tends towards a constant at the wall, the difficulty in fitting the values of k^+ towards the centre of the channel and finally, the slightly too small slope of U^+ in the logarithmic zone which leads to a large error on the Von-Karman constant.

From this work, we conclude that our implementation of the Chien and the Launder-Sharma low Reynolds number turbulence model is correct and we will therefore be able to use it to study filmwise condensation boundary layers.

4.3 Channel flow with suction

Many scientific papers in the literature on the validation of low Reynolds number k-ε models in flat channels assume an impermeable wall. However, for a condensation boundary layer, if the wall (or the film) is indeed impermeable for non-condensable gases, steam condenses and creates a flow towards the wall, like a suction, which results in a decrease in the thickness of the boundary layer. This phenomenon, studied experimentally and theoretically by Favre in 1966 [Favre et al., 1966], has since had numerous industrial applications, particularly in turbine blades, to make the fluid adhere and thus improve efficiency. With this suction, the momentum balance is modified by adding a convective transport by the normal velocity V and is written:

$$\rho U \frac{\partial U}{\partial x} + \rho V \frac{\partial U}{\partial y} - \frac{\partial}{\partial y}\left[(\mu + \mu_t)\frac{\partial U}{\partial y}\right] + \frac{\partial P}{\partial x} + g_x = 0 \tag{4.5}$$

We will therefore validate in our numerical models the inclusion of wall suction. For

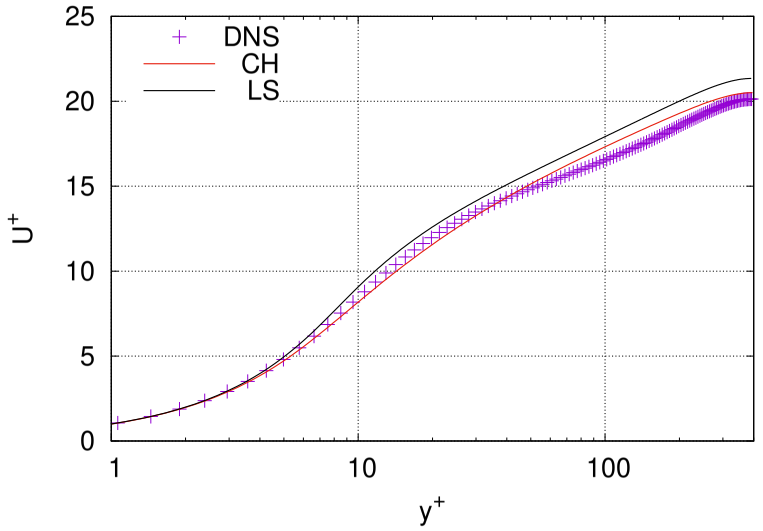

(a) Velocity $U^+ = U/u_\tau$

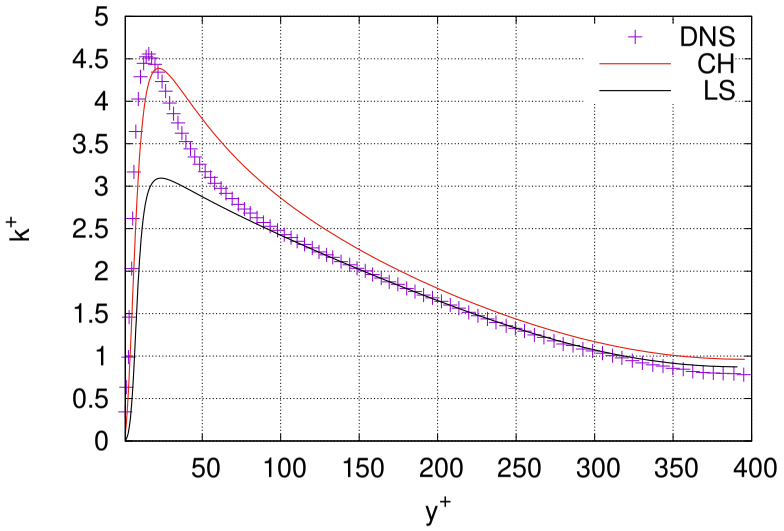

(b) Turbulent kinetic energy $k^+ = k/u_\tau^2$

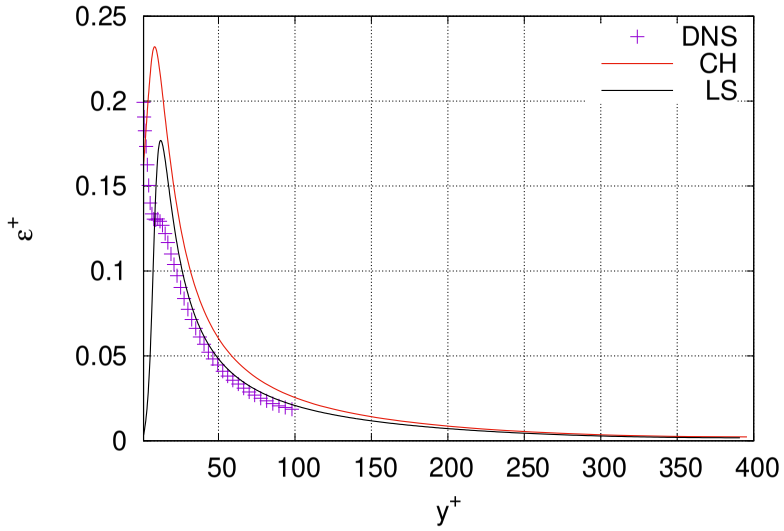

(c) Turbulent dissipation $\varepsilon^+ = \varepsilon\nu/u_\tau^4$

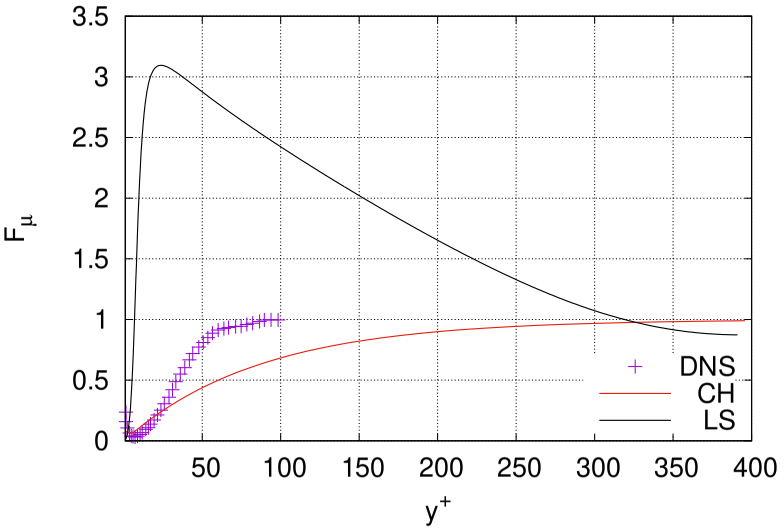

(d) Damping function f_μ

Figure 4.2: Channel flow results at $\mathrm{Re}_\tau = 395$.

this purpose, we have at our disposal the well-detailed Favre tests [Favre et al., 1966] of boundary layer with suction without pressure gradient. The experimental set-up is schematically reproduced in FIG. 4.3. As already mentioned, the experimental results

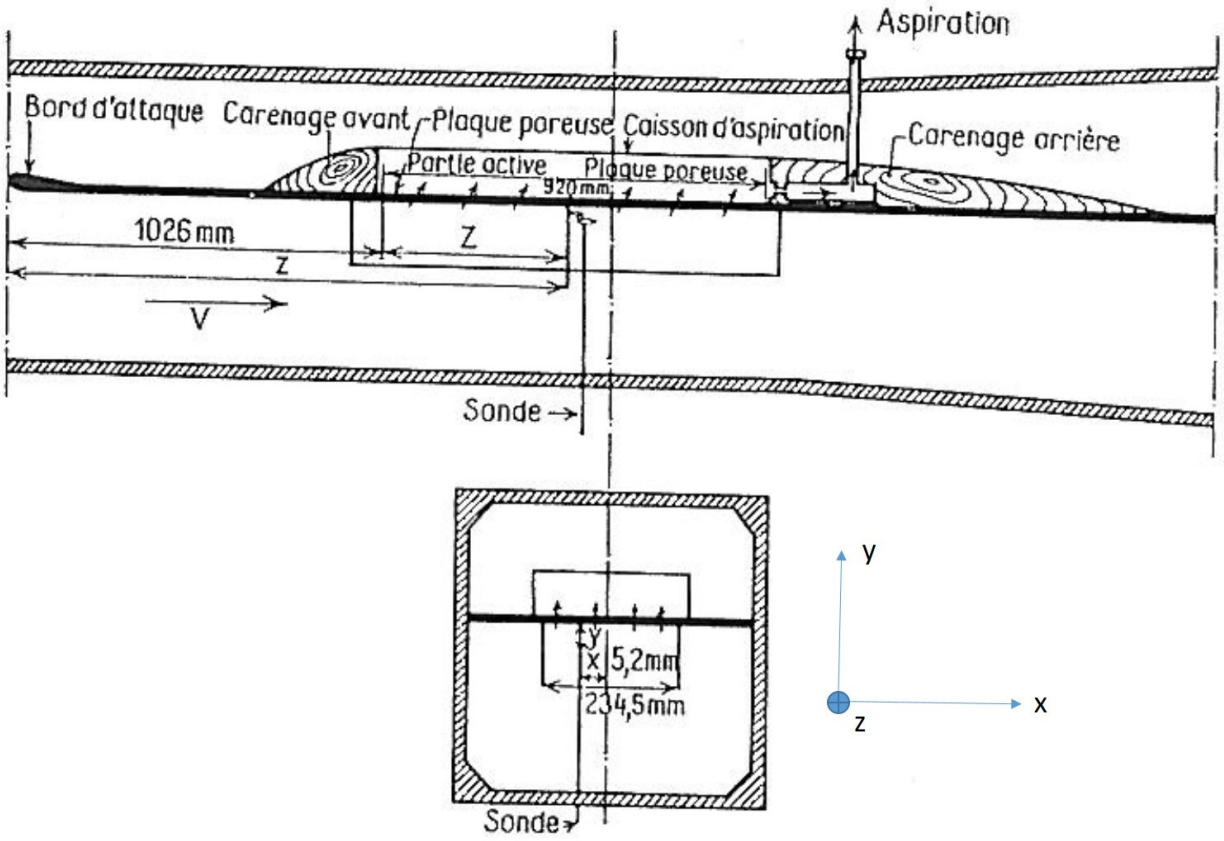

Figure 4.3: Wind channel used in the testing of [Favre et al., 1966].

show a decrease in the thickness of the turbulent boundary layer as the suction increases (FIG. 4.4a). These tests were also used in [Bucci, 2009; Lehmkuhl et al., 2016] as a first validation of low-Reynolds wall turbulence models with suction.

It is possible to compare the results of simulations with different experimental sources for low suction rates (around $A = \|V_w\|/U_\infty = 0.0025$) as in the results of [Favre et al., 1966] [Simpson, 1968] [Ferro, 2017]. The results from these three sources are consistent (FIG. 4.4b). The last author also points out that the boundary layers remain turbulent for suction rates lower than $\|V_w\|/U_\infty = 0.0037$, above which there is relaminarisation of the boundary layer and that the laws correspond well to an asymptotic turbulent state.

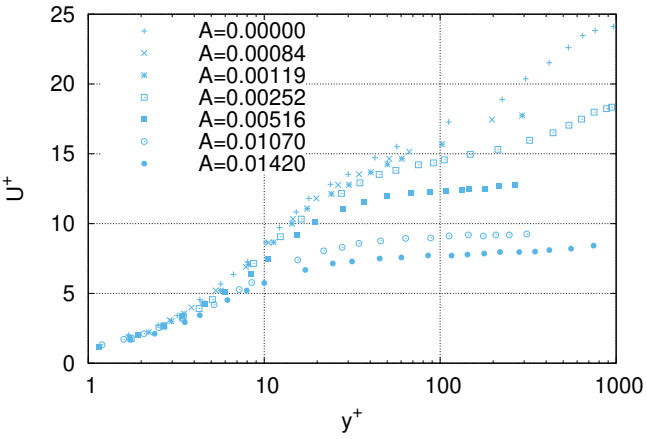

(a) Wall law measured in [Favre et al., 1966] with different suction rate.

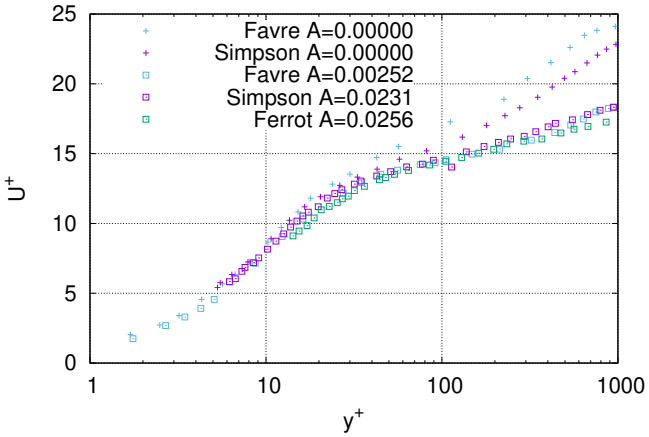

(b) Wall law measured in [Favre et al., 1966; Simpson, 1968; Ferro, 2017] for similar suction rates.

We will now compare the calculations with the results of Favre's experiments for different wall suction rates. The numerical model for the fluid and turbulence described in the previous paragraph is carried over into these calculations. We assume that the fluid is air at ambient temperature and pressure. The mesh used and the boundary conditions are described in the FIG. 4.5.

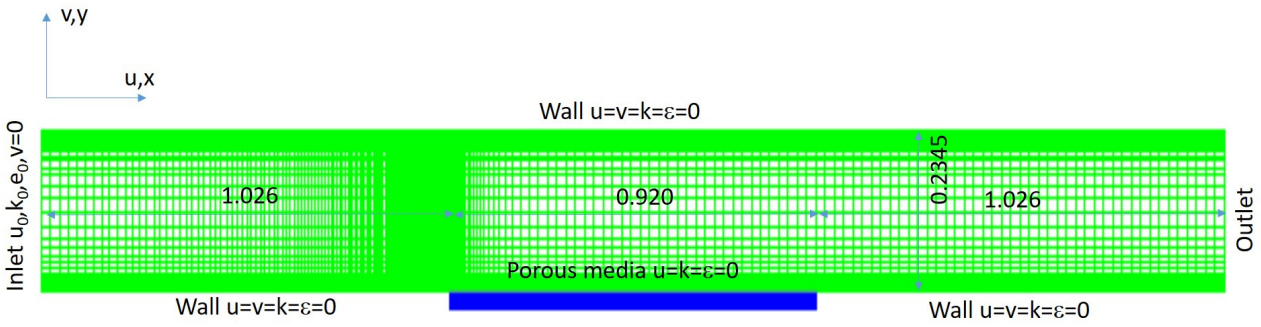

Figure 4.5: Mesh and boundary conditions for the calculation of [Favre et al., 1966].

The injection velocity is chosen according to the experiment $u_0 = 10.95$ m/s and for the values of the turbulent quantities we have chosen a turbulence intensity of 2% and a length scale of 1 mm. For the mesh size, we imposed to reach wall sizes such that $y^+ \approx 1$. The calculations, to obtain the steady state, are carried out until the residuals on all variables are less than 10^{-8}.

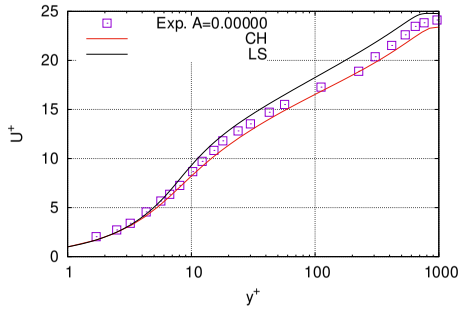

(a) $A = 0.00000$

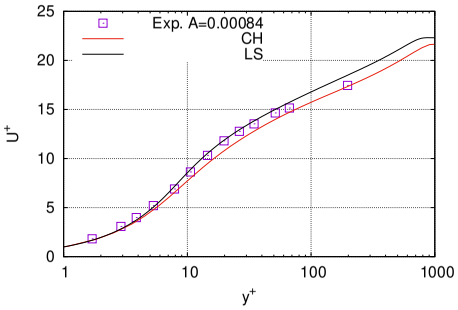

(b) $A = 0.00084$

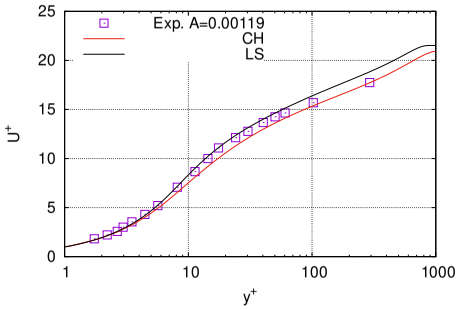

(c) $A = 0.00119$

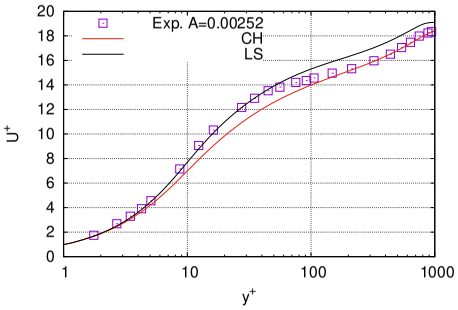

(d) $A = 0.00252$

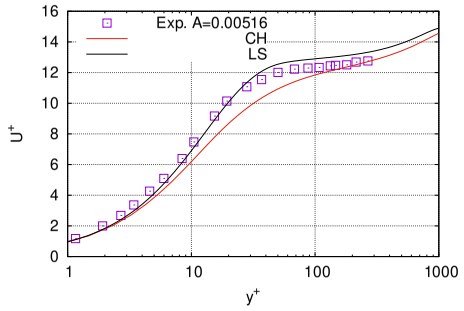

(e) $A = 0.00516$

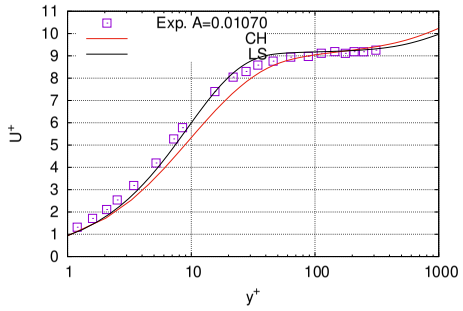

(f) $A = 0.01070$

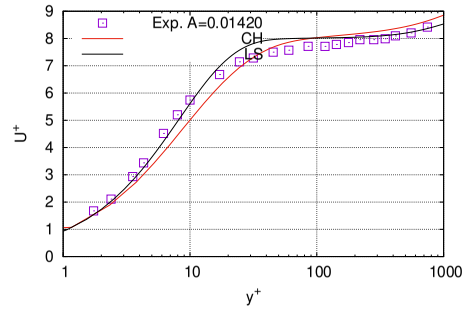

(g) $A = 0.01420$

Figure 4.6: Experiment with Suction: Comparison of Low Reynolds turbulent results (lines) and experimental results (points) from [Favre et al., 1966].

The comparison between the results obtained with the model and the experimental data is provided in Fig. Qualitatively, the effect of the suction is accurately predicted by the models, as was also concluded by [Bucci, 2009], and this for all suction rates. It can be noted that the largest differences are obtained in the $10 \leq y^+ \leq 100$ zone, i.e. the connection between the transition zone and the so-called logarithmic zone (without suction) for moderate suction rates. When the suction is strongest, this zone of deviations tends to be located for lower values of y^+, located in the transition zone. A possible reason for these deviations may still be the growth of the damping function f_μ of the Chien model.

In conclusion, the behaviour of the numerical models is relatively satisfactory in this validation case. Improvements can be envisaged in particular to see the impact of a f_μ function which decreases more slowly.

4.4 Channel flow with filmwise condensation

Four COPAIN tests with local measurements were selected to be calculated with the purely diffusive condensation model and the Chien model for low Reynolds number turbulence. We could not carry out the same exercise with the Launder-Sharma model of OpenFOAM due to time constraints. Nevertheless both models give similar results on the two previous cases. The mesh is constructed as in the Favre experiment, but with the COPAIN channel geometry (FIG. 4.7).

For the boundary conditions of the calculation, we have added the thermal treatment in the wall thickness and we impose the temperature on the face in contact with the secondary side ($T_{w,\text{external}}$). The properties of the aluminium plate are a thermal conductivity $\lambda_w = 12.2 + 26.51 \times 10^{-3} T_{\text{wall}} - 60.09 \times 10^{-6} T_{\text{wall}}^2 + 99.23 \times 10^{-9} T_{\text{wall}}^3$ and a thickness of 2.5 cm. As already mentioned, the liquid film is not simulated and there is temperature continuity between the fluid and the solid on the inside. For condensation, the mass fraction of steam

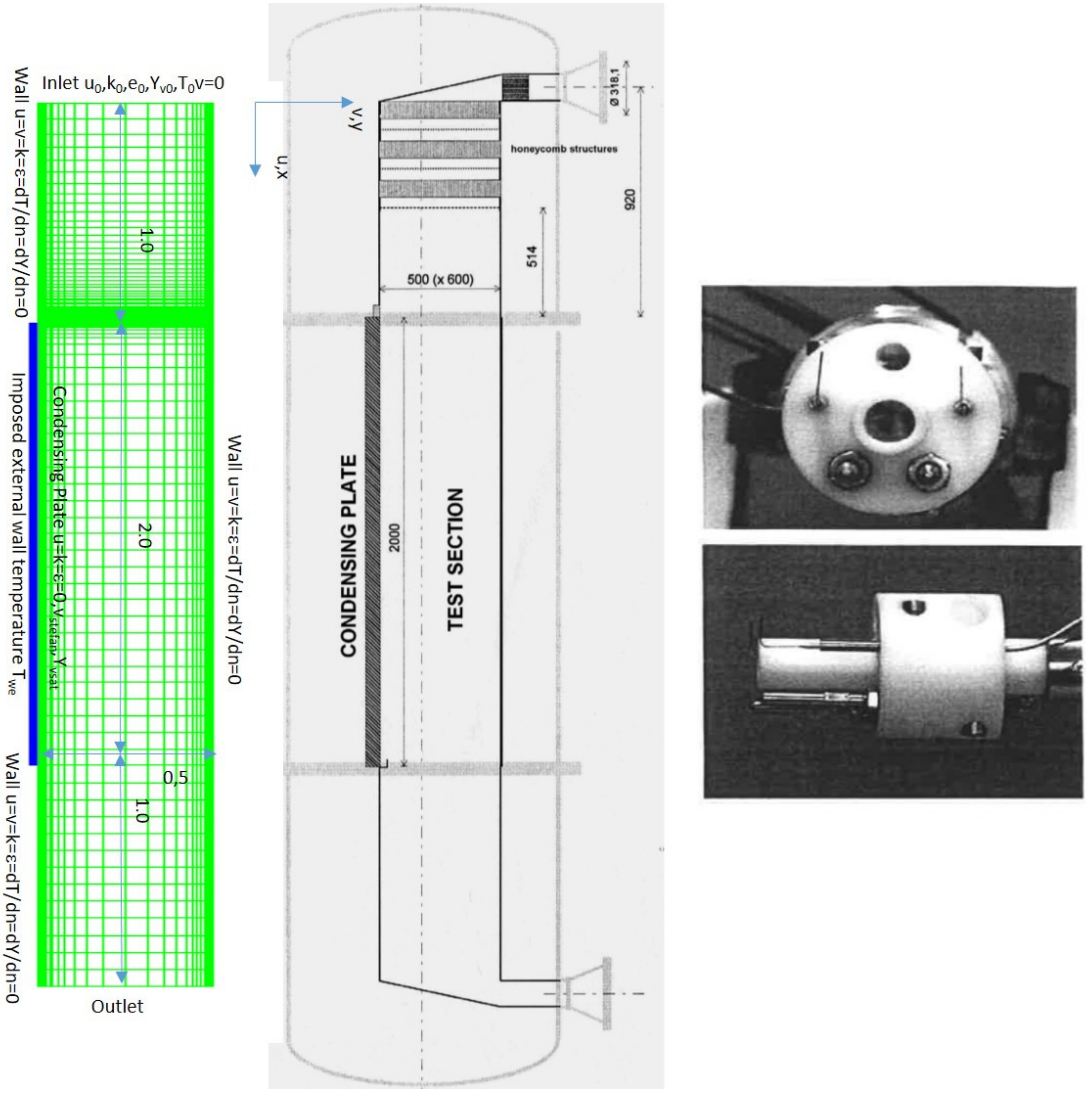

Figure 4.7: Mesh, boundary conditions for the calculation of the COPAIN experiments and views of the installation and the local probe.

on the inner side of the condensing wall is calculated by assuming saturation at the wall temperature $X_{v,interface} = P_{sat}(T_{\text{wall}})/P_{tot}$ and the velocity normal to the wall is estimated by the Stefan velocity:

$$U_{\text{Stefan}} = -D_{vm}\frac{1}{(1-Y_v)}\boldsymbol{\nabla}(Y_v). \tag{4.6}$$

For the physical properties of the air/steam mixture, the viscosity μ, the heat capacity C_p and the thermal conductivity λ of each of the gases depend on the temperature (CAST3M gas properties). The viscosity is (T in K and μ in kg/m/s):

$$\mu = \mu_{\text{ref}}\frac{T^{a_\mu}}{(T+b_\mu)} \tag{4.7}$$

For the thermal conductivity of each species, a similar law is adopted (T in K and λ in W/m/K):

$$\lambda = \lambda_{\text{ref}}\frac{T^{a_\lambda}}{(T+b_\lambda)} \tag{4.8}$$

Finally, the specific heats at constant pressure for non condensable gases follow a second order polynomial law (T in $^\circ$ C and C_p in J/kg/K):

$$C_p = C_{p,\text{ref}} + a_{C_p}T + b_{C_p}T^2 \tag{4.9}$$

The constants are provided in TAB. 4.4 for each gaseous species. The properties of air are deduced by a simple weighting of the ones of oxygen (20%) and the ones of nitrogen (80%). For steam, the heat capacity is calculated with the tables implemented in CAST3M (operator 'VARI' option 'DHVDT'). The latent heat H_{lat} is also estimated by the same tables (operator 'VARI' option 'LATEN'), as well as the saturation steam pressure P_{sat} (operator 'VARI' option 'PSATT').

Then, the values for the mixture are derived from a mixing law in accordance with the

Data	Nitrogen	Oxygen	Steam
μ_{ref}	1.791×10^{-6}	0.7406×10^{-6}	2.142×10^{-6}
a_μ	1.469	1.610	1.50
b_μ	140.812	48.16	890.
λ_{ref}	0.0417×10^{-3}	0.429×10^{-3}	-84.442×10^{-3}
a_λ	2.042	1.746	1.251
b_λ	-133.	41.27	-5827.1
$C_{p,ref}$	1030.9	917.	-
a_{C_p}	0.2044	0.1404	-
b_{C_p}	-3.3×10^{-5}	3×10^{-5}	-

Table 4.4: Gas species thermal and transport properties

law described in Wilke's article [Wilke, 1950] for μ and λ. On the other hand, for the heat capacity, the value for the mixture is derived from a simple weighting by the mass fraction. Wilke's formulation for viscosity is given below:

$$\mu = \sum_i \frac{X_i \mu_i}{\sum_j X_j \Phi_{ij}} \tag{4.10}$$

with X_i the molar fraction of each species and the coefficients Φ_{ij} given by :

$$\Phi_{ij} = \frac{\left[1 + \left(\frac{\mu_i}{\mu_j}\right)^{0.5} \left(\frac{M_j}{M_i}\right)^{0.25}\right]^2}{\left[8\left(1 + \frac{M_i}{M_j}\right)\right]^{0.5}} \tag{4.11}$$

Finally, for the steam diffusion coefficient in the air/steam mixture $D_{v,m}$, we use the binary coefficient from Marrero and Mason's publication [Marrero and Mason, 1972] with a dependence on temperature and total pressure.

$$p_{tot} D_{v,m} = A T^B \tag{4.12}$$

with A = 0.187 10^{-9} m^2/s.atm.K^{-B}, B = 2.0272 and p in atmosphere.

The balance equations are solved sequentially and the steady state is recovered as the asymptotic limit of a transient when the residuals for both velocity and temperature

components are less than 10^{-5}.

The boundary conditions corresponding to the four tests and used for the numerical calculations are summarised in TAB. 4.5. They correspond to averages over the different experimental stages.

Essai	T_{in} (°C)	$Y_{v,\text{in}}$	U_{in} (m/s)	P (bar)	$T_{w,\text{external}}$ (°C)
P064	75.5	0.127	3.0	1.203	54.4
P066	71.5	0.128	1.0	1.208	46.3
P071	162.6	0.702	1.0	6.608	97.2
P074	160.1	0.698	0.2	6.479	98.7

Table 4.5: Initial and boundary conditions for the 4 selected tests.

4.4.1 Mesh sensitivity for P064 test

On the first test, we studied the sensitivity of the result to the mesh size in the near wall region. The experimental uncertainties for the measurements are $+/-20$ mbar for the pressure, $+/-0.6$ K for the temperature, $+/-0.04$ m/s for the velocities and $0.06\Phi + 100$ for the fluxes. For the mass fractions that interest us in this paragraph, they are deduced from the temperatures.

To present the results (FIG. 4.8), we plot the flux transferred to the wall Φ and the temperature at the inner face T_{ws} as a function of the normalized size of the first mesh y^+ and this for the profile at $z = 1.75$ m obtained experimentally. The results are similar for the other profiles.

From this analysis, we deduce that when the normalised mesh size is less than 0.5, the obtained results no longer depend on the mesh size. This result is similar to the analysis made on the effect of suction. Moreover, this result is in line with the analyses of Bucci [Bucci, 2009]. We will therefore retain this criterion for the calculations of the various tests.

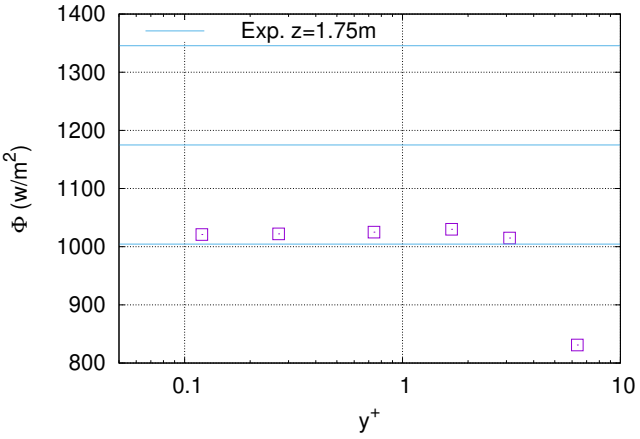

(a) Effect on the calculation of the total wall flux Φ.

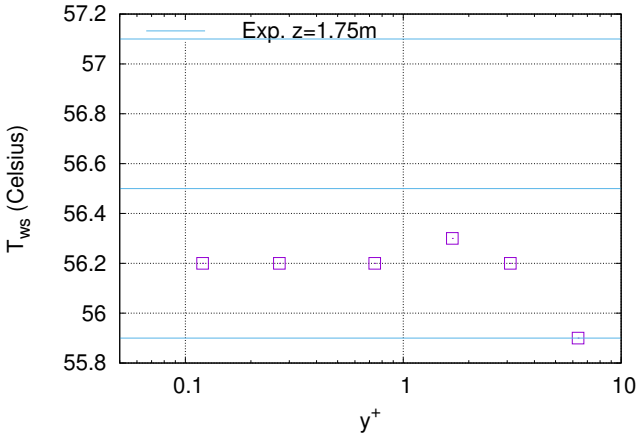

(b) Effect on the calculation of the wall temperature T_{ws}.

Figure 4.8: Effect of the size of the first wall mesh in the simulations of test P064.

4.4.2 Global results

The results in terms of total flux Φ and internal face temperature T_{ws} for the four tests are provided in TAB. 4.6. We also compare the calculated values with the measured values in FIG. 4.9. This work shows that the model approaches well the experimental results for forced and mixed convection conditions. However, in natural convection (Profiles P074_3 and P074_4), the model underestimates the total wall fluxes and thus the internal temperature. A possible explanation could be that buoyancy is not taken into account in the transport equations of the turbulence model. Generally, these additional terms at the production level involve the scalar product of the local density gradient with the gravity vector. We did not investigate this in this work.

Another possible explanation for this behavior of the model is that the liquid film is not taken into account. Currently, in the model, it is the inside temperature of the wall that is used to calculate the wall fluxes, which is a lower temperature than what has been estimated experimentally. Therefore, taking the liquid film into account would tend to make the numerical model even more far away from the experiment.

Test	T_{in} (°C)	$X_{v,in}$	U_{in} (m/s)	P (bar)	T_{we} (°C)	Φ_{exp} (W/m^2)	$T_{ws,exp}$ (°C)	Φ_{calc} (W/m^2)	$T_{ws,calc}$ (°C)
P064_2	75.5	0.190	3.0	1.203	54.4	1286.	55.6	1267.	56.5
P064_3	75.5	0.190	3.0	1.203	54.4	1283.	56.7	1179.	56.3
P064_4	75.5	0.190	3.0	1.203	54.4	1175.	56.6	1123.	56.2
P066_2	71.4	0.190	1.0	1.209	46.3	852.	47.9	900.	47.7
P066_3	71.4	0.190	1.0	1.209	46.3	853.	47.9	756.	47.5
P066_4	71.4	0.190	1.0	1.209	46.3	835.	47.7	680.	47.4
P071_2	162.6	0.783	1.0	6.615	97.2	21069.	132.1	24900.	131.0
P071_3	162.6	0.783	1.0	6.615	97.2	20057.	130.2	22000.	127.3
P071_4	162.6	0.783	1.0	6.615	97.2	18976.	128.4	20916.	125.8
P074_2	160.1	0.779	0.2	6.430	98.7	20453.	130.9	21411.	128.1
P074_3	160.1	0.779	0.2	6.430	98.7	26647.	142.5	23376.	130.6
P074_4	160.1	0.779	0.2	6.430	98.7	26740.	142.8	24880.	132.4

Table 4.6: Results for heat flux and temperature on the inside condensing wall.

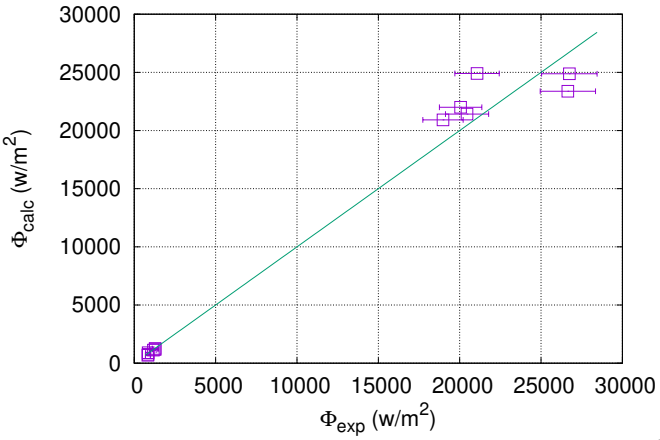

(a) Exp./Calc. comparison for total heat flux Φ.

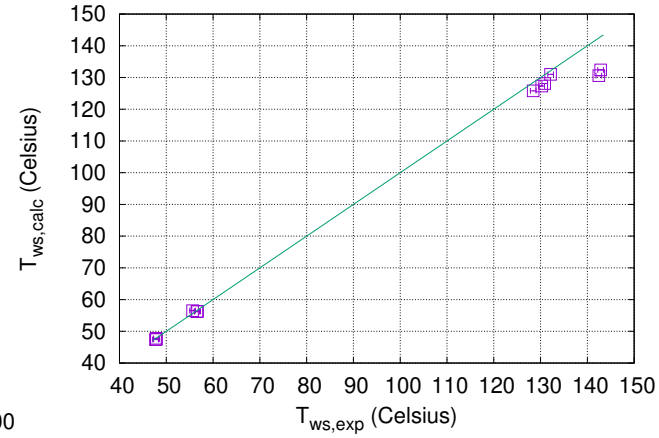

(b) Exp./Calc. comparison for wall temperature T_{ws}.

Figure 4.9: Comparison of Experiments/Calculations for the four simulated COPAIN tests.

4.4.3 Local results

For the four simulated tests, we compare the thermal and mass boundary layers at the three altitudes of the experimental measurements (FIG. 4.10 and 4.11). First of all, the prediction of the thermal boundary layers is relatively good for the different convection regimes. The observable differences on the edge and centre conditions arise from the fact that in the simulations we impose a uniform external temperature on the condensing wall and experimentally there must be some gradients. Taking into account the secondary side of the heat exchanger along the plate can be considered but there is no information in the experimental data to model this system.

For the mass boundary layers, the differences between calculation and experiment are larger. For natural convection (test P074), the wall condition probably has an important influence on the result. Generally, the calculated mass boundary layers are thicker than those measured. We recall here the fact that the sampling system used in the experiments is likely to affect these boundary layers because the sampling velocity is admittedly low compared to the flow velocity (except for P074) but high compared to the Stefan velocity. Let us also mention the fact that the simulations were conducted with a value of 0.7 for the

turbulent Schmidt number, whereas the turbulent Prandtl number was chosen at 0.85.

From these results, it is concluded that, for the thermal, the measurements and simulations are globally in agreement. Improving the low Reynolds model (especially the damping function f_μ), the value of the turbulent Prandtl number, the modeling of the temperature boundary condition on the external surface and taking into account a liquid film (1D for example) can perhaps reduce the gap between simulation and experiment. For mass boundary layers, one must also add the need to develop a non-intrusive measurement technique to access their characterisation in the experiments.

For the next chapter, it is relevant to build the dimensionless profiles of the experimental results and the numerical ones (at the location $z = 1.75$ m). The velocity profile was not measured in the experiments consequently the friction velocity can not be deduced from the experimental measurements. We propose to use the numerical value of the friction velocity as a reference velocity scale. Experimentally, the total heat flux Φ_{tot} is measured inside the aluminium plate and as explained in the thesis of Bucci, we can use the temperature measurements to extract the sensible heat flux $\dot{q}_{conv,w}$ and the local condensation mass flux $\dot{m}_{v,w}{}''$ according to the heat and mass transfer analogy.

$$\phi_{tot} = \dot{q}_{conv,w} + H_{lat,w}\dot{m}_{v,w}{}'' \tag{4.13}$$

$$\frac{\dot{q}_{conv,w}}{\dot{m}_{v,w}{}''} = \frac{C_p\left(T_{w,s} - T_{bulk}\right)}{\frac{Y_{v,w}-Y_{v,bulk}}{1-Y_{v,w}}}\left(\frac{\mathrm{Sc}}{\mathrm{Pr}}\right)^{2/3} \tag{4.14}$$

These data are then used to compute the reference temperature T^* and the reference steam mass fraction Y_v^* involved in the wall function.

The data from the experiments and the numerical analysis are provided in TAB. 4.7 and 4.8 and both profiles are plotted in FIG. 4.12. It is obvious that the scaled profiles from the experimental results are quite different from the calculated ones for those experiments with high total heat flux. The scaling of the experimental profiles depends on the value of the calculated friction velocity but also on the reconstruction of the partition of the total heat

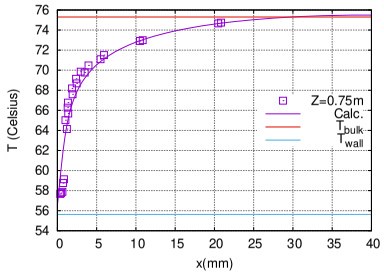

(a) P064 $Z = 0.75$ m

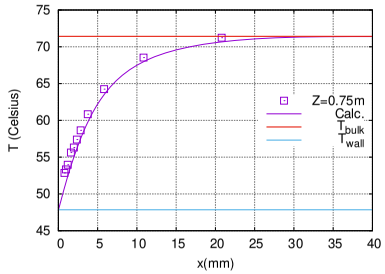

(b) P066 $Z = 0.75$ m

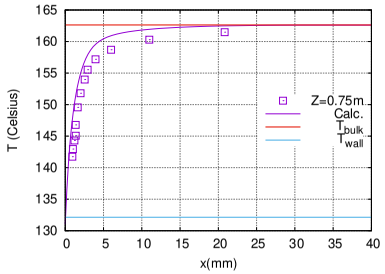

(c) P071 $Z = 0.75$ m

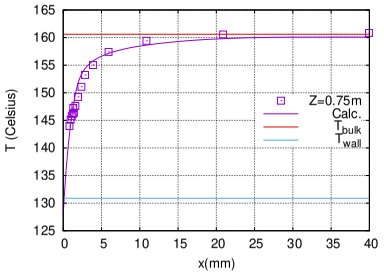

(d) P074 $Z = 0.75$ m

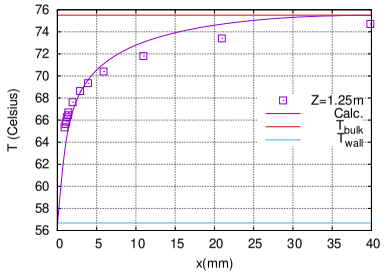

(e) P064 $Z = 1.25$ m

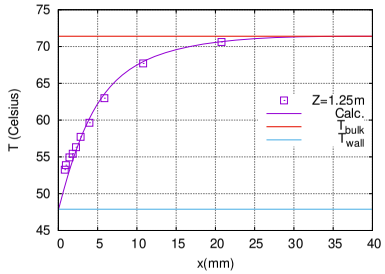

(f) P066 $Z = 1.25$ m

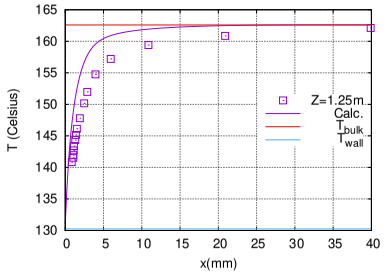

(g) P071 $Z = 1.25$ m

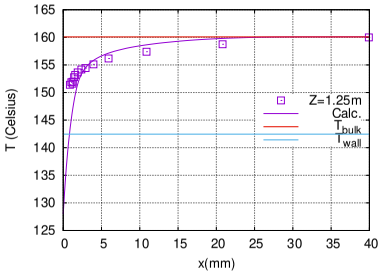

(h) P074 $Z = 1.25$ m

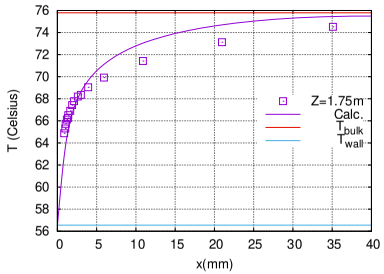

(i) P064 $Z = 1.75$ m

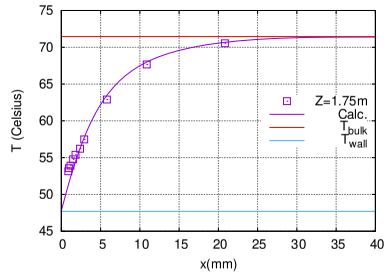

(j) P066 $Z = 1.75$ m

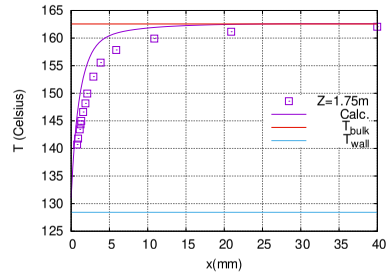

(k) P071 $Z = 1.75$ m

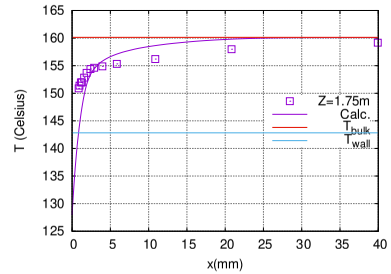

(l) P074 $Z = 1.75$ m

Figure 4.10: Thermal boundary layer: COPAIN test results with local measurements compared to simulations.

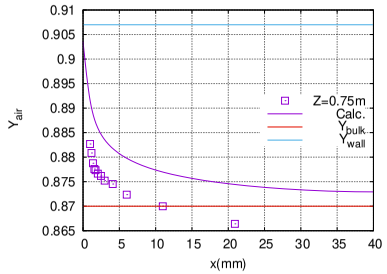

(a) P064 $Z = 0.75$ m

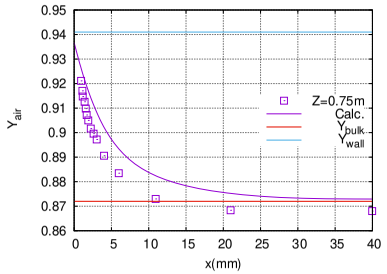

(b) P066 $Z = 0.75$ m

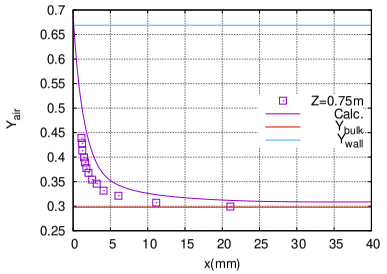

(c) P071 $Z = 0.75$ m

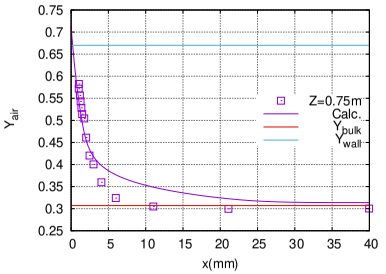

(d) P074 $Z = 0.75$ m

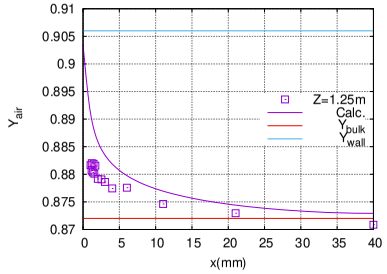

(e) P064 $Z = 1.25$ m

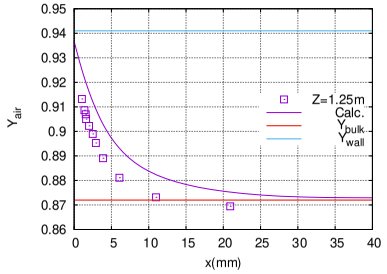

(f) P066 $Z = 1.25$ m

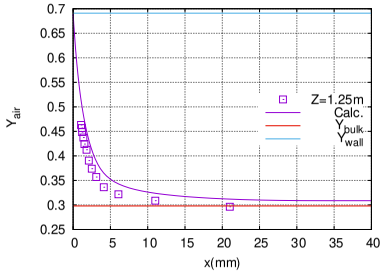

(g) P071 $Z = 1.25$ m

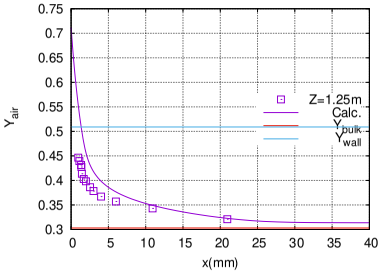

(h) P074 $Z = 1.25$ m

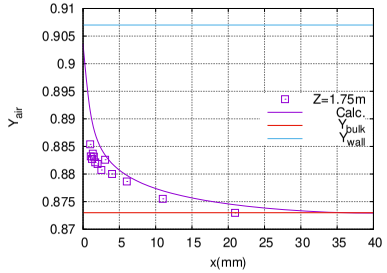

(i) P064 $Z = 1.75$ m

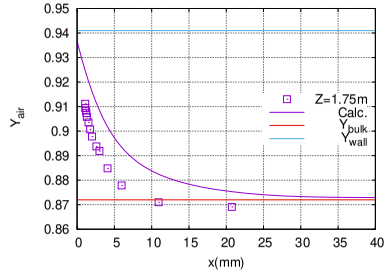

(j) P066 $Z = 1.75$ m

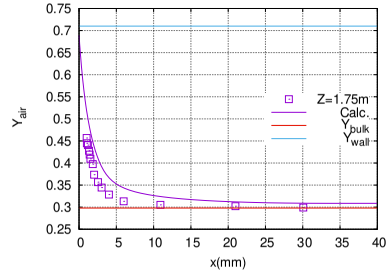

(k) P071 $Z = 1.75$ m

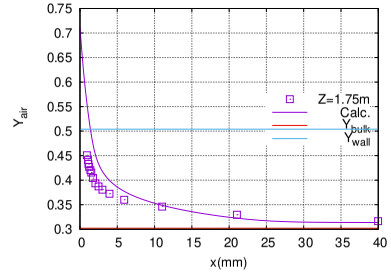

(l) P074 $Z = 1.75$ m

Figure 4.11: Mass Boundary Layer: COPAIN test results with local measurements compared to simulations.

flux into sensible and latent heat flux. The reasons for these discrepancies are analysed in Chapter 5 and proposals are evaluated to improve this point. Finally, these data are used in chapter 5 to check the accuracy of the wall functions.

Data	P064_4	P066_4	P071_4	P074_4
T_{ws} (°C)	56.2	47.4	125.8	132.5
ρ (kg/m^3)	1.16	1.20	4.43	4.23
C_p (J/kg/K)	1238.4	1207.9	1832.1	1883.3
$Y_{v,w}$	0.095	0.062	0.258	0.339
Pr	0.798	0.780	1.047	1.057
Sc	0.751	0.755	0.693	0.692
ν (m^2/s)	1.59E-5	1.53E-5	4.08E-5	4.19E-5
Gr_x	1.61E10	2.57E10	9.85E11	7.03E11
Re_x	3.17E5	1.08E5	3.71E5	0.75E5
Ri_x	0.15	1.98	5.35	101.00
u_τ (m/s)	0.140	0.073	0.075	0.061
V_i (m/s)	2.88E-4	1.76E-4	1.53E-3	2.00E-3
$\dot{q}_{conv}$ (W/m^2)	303.	149.	4172.	5000.
$\dot{m}_v$ (kg/m2/s)	3.47E-4	2.23E-4	7.66E-3	9.18E-3
Pr_t	0.85	0.85	0.85	0.85
Sc_t	0.70	0.70	0.70	0.70
F_g^+	3.89E-3	3.76E-2	2.31E-2	3.83E-2
q^+	2.05E-3	2.41E-3	2.03E-2	3.23E-2
$\dot{q}_{tot}$ (W/m^2)	1123.	680.	20916.	24880.
Ra_x	1.29E10	2.01E10	1.03E12	7.44E11
$V_w^+ = V_i/u_\tau$	0.00205	0.00241	0.02045	0.03292

Table 4.7: Selected COPAIN Tests: Computed variables involved in the numerical boundary layers.

4.5 Conclusions of the chapter

The work carried out in this chapter shows that the most common models of low Reynolds number turbulence can correctly predict the effect of suction on a turbulent boundary layer.

For profiles in the presence of filmwise condensation, the limited number of data available does not allow us to conclude on the predictive character of the models. However, the obtained results on the gas temperature profile are acceptable. For the mass frac-

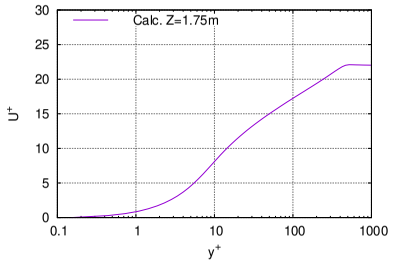

(a) P064 $Z = 1.75$ m U

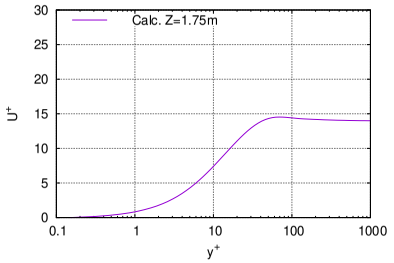

(b) P066 $Z = 1.75$ m U

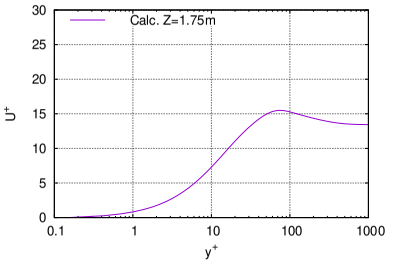

(c) P071 $Z = 1.75$ m U

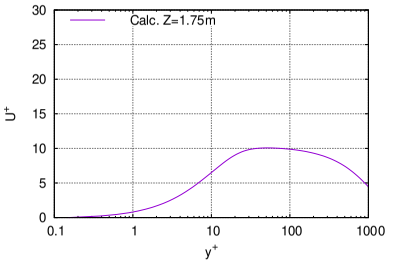

(d) P074 $Z = 1.75$ m U

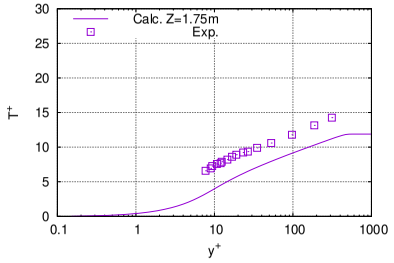

(e) P064 $Z = 1.75$ m T

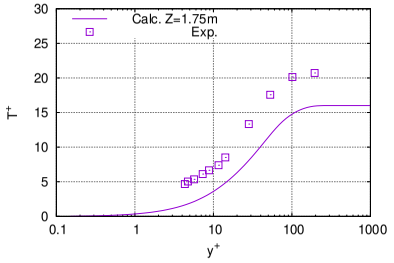

(f) P066 $Z = 1.75$ m T

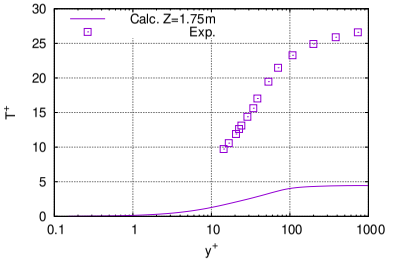

(g) P071 $Z = 1.75$ m T

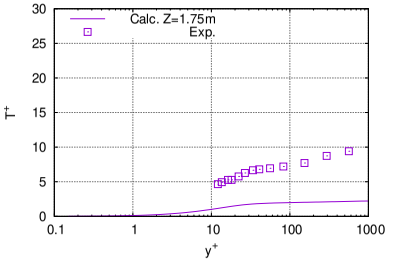

(h) P074 $Z = 1.75$ m T

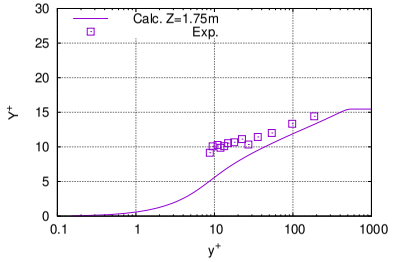

(i) P064 $Z = 1.75$ m Y_v

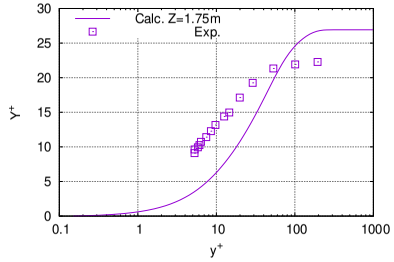

(j) P066 $Z = 1.75$ m Y_v

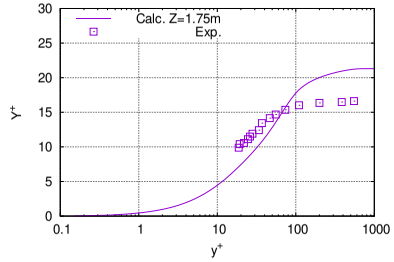

(k) P071 $Z = 1.75$ m Y_v

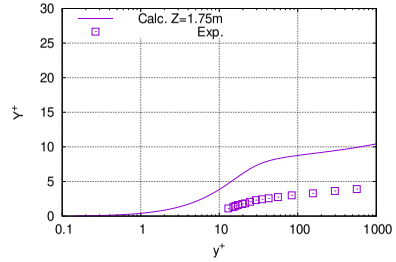

(l) P074 $Z = 1.75$ m Y_v

Figure 4.12: Wall-Functions: COPAIN results

Data	P064_4	P066_4	P071_4	P074_4
T_{ws} (°C)	56.6	47.9	128.4	142.8
$Y_{v,w}$	0.093	0.059	0.312	0.496
T_{bulk} (°C)	75.8	71.5	162.6	160.1
$Y_{v,bulk}$	0.127	0.128	0.702	0.698
$\dot{q}_{conv}$ (W/m^2)	233.	111.	633.	719.
$\dot{m}_v$ (kg/m^2/s)	3.98E-4	3.03E-4	8.46E-3	1.22E-2
$\dot{q}_{tot}$ (W/m^2)	1175.	835.	18976.	26740.
T^*	1.257	1.125	1.265	1.739
Y_v^*	2.36E-3	3.28E-3	2.34E-2	4.80E-2

Table 4.8: Selected COPAIN Tests: Measured and recomputed variables (based on Bucci's analysis) involved in the experimental boundary layers.

tion profile, the experimental boundary layer is probably affected by the measurement technique. In dimensionless form, the experiments have not provided the friction velocity. Consequently, the dimensionless profiles are plotted using the calculated friction velocity. Moreover, the partition between sensible and latent heat fluxes is determined with the method recommended by M. Bucci which does not take into account interdiffusion. With all these assumptions, the dimensionless temperature and mass fraction profiles are quite far from the numerical results, especially when the fluxes are large.

In future experiments, the simultaneous measurement of all three boundary layers should remain an experimental priority. Nevertheless, we consider that these results are accurate enough to obtain the dimensionless profiles for the scaling up to the wall functions in the next chapter. Improvement of the partition of the sensible and the latent heat in the experiments is also discussed in the next chapter in order to have a better scaling of the dimensionless experimental results.

Chapter 5

Extended wall functions for coupled heat and mass transfer

5.1 Introduction

We have seen in the previous chapter that accurate prediction of the mass and heat transfer requires a fine mesh near the wall, which is associated with a high computational cost. A method to assess the transfer with fewer computational resources is therefore needed. In standard approaches for wall modeling, one makes assumption of constant physical properties (density, viscosity, etc.). Wall functions can be obtained by analytical integration of the boundary layer equations functions [Leduc, 1995] based on discussions of the turbulence behavior in the viscous sub-layer and in the inertial sub-layer. This method is straightforward but requires the physical properties to be nearly unchanged, which is not the case for a simultaneous heat and mass transfer. It is therefore necessary to model the boundary layer in a manner that allows for variation of physical properties.

Over the last two decades, a consistent effort has taken place in order to generalize the wall function approach [Shih et al., 1999], [Craft et al., 2002a], [Utyuzhnikov, 2005],

[Mohammadi and Puigt, 2006] so that various physical phenomena can be accounted for. In our case the physics to be included include compressibility, coupled heat and mass transfer, condensation (which is associated here with suction effect). Other effects that will not be taken into account in the present description but have been the object of previous studies are the effect of the streamwise pressure gradient [Shih et al., 2002], film surface roughness [Suga et al., 2006] and buoyancy [Craft et al., 2002a].

Some of the aspects that we wish to include in the wall functions have already been successfully modelled. Cabrit and Nicoud [Cabrit and Nicoud, 2009] used direct numerical simulation to construct and validate a wall model for multicomponent reacting compressible turbulent flows. However their wall model did not account for suction effects associated with condensation.

In contrast, Yoon et al. [Yoon et al., 2018] considered filmwise condensation in presence of a non-condensable gas. They developed a condensation model where condensation appeared as a sink in the mass, momentum, energy, and species conservation equations, and introduced a stress-free condition at the interface, but their work did not lead to a directly usable wall function.

As pointed out by Cabrit and Nicoud, generalized wall functions should be obtained from the basic flow equations with as little curve-fitting or artificial integration as possible. One interesting approach in that respect was followed by Muto et al. [Muto et al., 2019], who derived an equilibrium wall model to include the effects of chemical reaction and variable properties. They used a look-up table to determine the variations of the mass fraction with the temperature at equilibrium. They obtained a system of one-dimensional transport equations where turbulent fluxes were modelled using classic gradient assumptions with a modified mixing length model based on semi-local scaling - i.e. using reference units based on the local density ρ instead of the wall density ρ_w. The equations were solved using a finite difference method (FDM).

We note that a related FDM approach was used in the early 1970s by Landis and Mills [Landis and Mills, 1972]. They derived the conservation equations with an integral of the momentum as the variable to predict skin friction and heat transfer coefficients. Their assumption was that the momentum equation is coupled to the species and energy equations only through spatial variations of the mean density and viscosity.

In this chapter, we chose to follow Muto's approach by deriving a set of 1-D ordinary differential equations for the problem of coupled heat and mass transfer, taking into account interdiffusion, modelling condensation with wall suction, and allowing physical properties of the mixture to vary. We use the mixing length hypothesis with a Van Driest correction factor. Integration of the system of ODE's yield numerical wall functions that are compared with low-Reynolds models as well as numerical simulation and experimental data for configurations of increasing physical complexity.

5.2 Wall functions for a turbulent layer without suction

First, one shall begin with the classic boundary layer equation which states that the total stress is constant:

$$\frac{\mathrm{d}}{\mathrm{d}y}\left((\mu+\mu_t)\frac{\mathrm{d}\overline{u}}{\mathrm{d}y}\right)=0. \tag{5.1}$$

Here, it is assumed that ρ and μ are constant. We further assume that the turbulent viscosity μ_t is given by mixing length model and Van Driest's model:

$$\mu_t=\mu\left(l_m^+\right)^2\left|\frac{\mathrm{d}u^+}{\mathrm{d}y^+}\right|, \tag{5.2}$$

$$l_m^+=\kappa y^+\left[1-\exp\left(-\frac{y^+}{A^+}\right)\right], \tag{5.3}$$

$$\frac{\mathrm{d}u^+}{\mathrm{d}y^+}=\frac{2}{1+\sqrt{1+4\kappa^2{y^+}^2\left[1-\exp\left(-\frac{y^+}{A^+}\right)\right]^2}}, \tag{5.4}$$

where the constant $\kappa = 0.41$ is the von Karman constant and $A^+ = 26$.

Dirichlet boundary conditions for $\overline{u}$ are imposed on the wall $\overline{u}_w = 0$ and in the bulk $\overline{u}_b = u_\infty$. We note that these conditions will hold in forced convection where the dynamics are not influenced by the characteristics of the transfer.

5.2.1 Finite Difference Method

In order to solve this equation numerically, one defines a mesh $(y_n)_{n=0,...,N}$ with $N+1$ nodes and geometrically refined on the wall as following:

$$\begin{cases} y_0 = 0, \\ y_i = y_b \left(\dfrac{y_b}{y_w} \right)^{-\frac{N-i}{N-1}}, \ i = 1, ..., N, \end{cases} \tag{5.5}$$

where $y_1 = y_w$ is the position of the first node and $y_N = y_b$ is the total length of the mesh. $\overline{u}$ is estimated on (y_n) as (u_n).

The Dirichlet boundary conditions are:

$$\begin{cases} u_0 = 0, \\ u_N = u_\infty. \end{cases} \tag{5.6}$$

The left hand side of the equation (5.1) is then discretized on the non-uniform mesh (y_n) using the finite difference method. One notes $[f]|_n$ the numerical estimation of the function f at y_n. By using a standard differentiation scheme, one obtains

$$\left[\alpha \frac{\mathrm{d}u}{\mathrm{d}y} \right] \Bigg|_{n+\frac{1}{2}} \approx \frac{\alpha_{n+1} + \alpha_n}{2} \cdot \frac{u_{n+1} - u_n}{y_{n+1} - y_n}$$

one can calculate

$$\left[\frac{\mathrm{d}}{\mathrm{d}y}\left(\alpha\frac{\mathrm{d}u}{\mathrm{d}y}\right)\right]\Big|_n \approx \frac{\left[\alpha\frac{\mathrm{d}u}{\mathrm{d}y}\right]\Big|_{n+\frac{1}{2}} - \left[\alpha\frac{\mathrm{d}u}{\mathrm{d}y}\right]\Big|_{n-\frac{1}{2}}}{y_{n+\frac{1}{2}} - y_{n-\frac{1}{2}}}$$
$$\approx \frac{\frac{\alpha_{n+1}+\alpha_n}{2}\cdot\frac{u_{n+1}-u_n}{y_{n+1}-y_n} - \frac{\alpha_{n-1}+\alpha_n}{2}\cdot\frac{u_n-u_{n-1}}{y_n-y_{n-1}}}{\frac{y_{n+1}+y_n}{2} - \frac{y_{n-1}+y_n}{2}}$$
$$\approx \frac{1}{y_{n+1}-y_{n-1}}\left(\frac{\alpha_{n+1}+\alpha_n}{y_{n+1}-y_n}\left(u_{n+1}-u_n\right) - \frac{\alpha_{n-1}+\alpha_n}{y_n-y_{n-1}}\left(u_n-u_{n-1}\right)\right)$$

Finally, one may estimate the expression $\frac{\mathrm{d}}{\mathrm{d}y}\left(\alpha\frac{\mathrm{d}u}{\mathrm{d}y}\right)$ at inner points using the following discretization:

$$\left[\frac{\mathrm{d}}{\mathrm{d}y}\left(\alpha\frac{\mathrm{d}u}{\mathrm{d}y}\right)\right]\Big|_n \approx \begin{pmatrix} \frac{1}{y_{n+1}-y_{n-1}}\frac{\alpha_{n-1}+\alpha_n}{y_n-y_{n-1}} \\ -\frac{1}{y_{n+1}-y_{n-1}}\left(\frac{\alpha_{n-1}+\alpha_n}{y_n-y_{n-1}}+\frac{\alpha_{n+1}+\alpha_n}{y_{n+1}-y_n}\right) \\ \frac{1}{y_{n+1}-y_{n-1}}\frac{\alpha_{n+1}+\alpha_n}{y_{n+1}-y_n} \end{pmatrix}^T \begin{pmatrix} u_{n-1} \\ u_n \\ u_{n+1} \end{pmatrix}, \; n = 1, ..., N-1. \quad (5.7)$$

The numerical estimation of μ_t is given by the equations (5.2, 5.3, 5.4) where the velocity profile is given by (u_n). A numerical estimate of u_τ is given by:

$$[u_\tau] = \sqrt{\frac{\mu}{\rho}\frac{u_1-u_0}{y_1-y_0}}, \quad (5.8)$$

and it is known that

$$\left[y^+\right]_n = \frac{\rho y_n [u_\tau]}{\mu}. \quad (5.9)$$

The discretization of equation (5.4), together with (5.6), is then solved iteratively until convergence is reached.

A linear profile was chosen to initialize (u_n) at the beginning of the interative process:

$$u_n = u_0 + \frac{y_n}{y_N}\left(u_N - u_0\right). \quad (5.10)$$

To summarize, the algorithm used to determine numerically the profile of the velocity $\overline{u}$ is the following:

Algorithm 1: Algorithm to compute the classic wall law

initialize (u_n) by Eq.(5.10);

while *Convergence of* (u_n) *not reached* **do**

calculate $[\mu_t]$ from (5.2, 5.3, 5.4) using (u_n) ;

impose Dirichlet boundary condition (5.6) to obtain the linear system

$A_{\text{BC}}(u_n) = B_{\text{BC}}$;

calculate the stiffness matrix $A_{\text{diff.}}$ of the LHS of (5.12) by (5.7);

solve the linear system $(A_{\text{BC}} + A_{\text{diff.}})(u_n) = B_{\text{BC}}$ to renew (u_n);

end

In practical, it was found that 30 iterations were enough for (u_n) to reach convergence (round-off error).

5.2.2 Results

Using the method described above, we obtain the velocity profile shown in FIG. 5.1 (blue curve). This profile can be compared with classic theoretical laws (linear law in viscous sub-layer and the log law in inertial sub-layer), numerical simulation results from Kim, Moin and Moser [Kim and Corradini, 1990] and experimental data from Favre [Favre et al., 1966] (without suction). A good agreement is observed, which constitutes validation of the method.

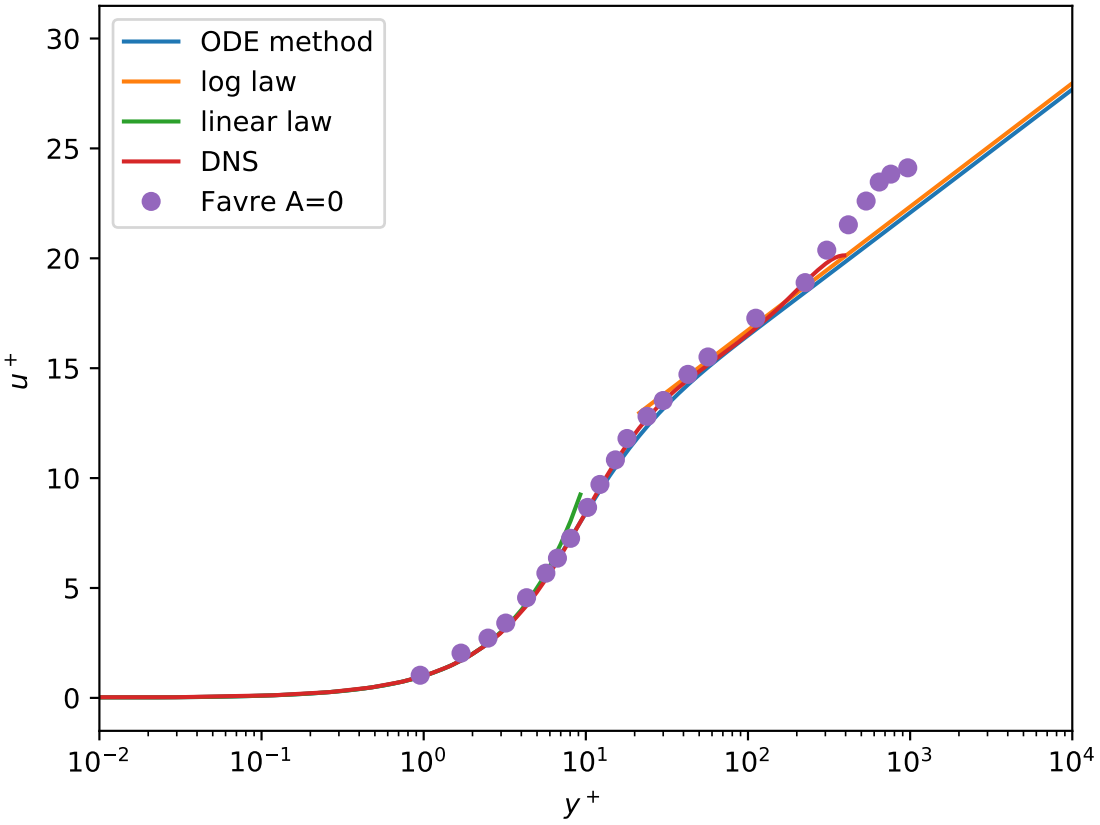

Figure 5.1: Comparison of the result of current ODE method with theoretical laws (linear law in viscous sub-layer and log law in inertial sub-layer) and Mansour's DNS result [Mansour et al., 1988]

5.3 Dynamic boundary layer modeling with suction or blowing

5.3.1 Analysis and method

In the case of wall suction or blowing, one writes from the conservation of mass at equilibrium ($\frac{\partial}{\partial t}$ and $\frac{\partial}{\partial x}$ are neglected) :

$$\frac{\mathrm{d}\overline{\rho v}}{\mathrm{d}y} = 0, \tag{5.11}$$

which shows that the mass flux normal to the wall noted $\overline{\phi}_y$ is constant in the boundary layer and equal to its value on the wall $\overline{\phi}_{y,w}$.

The flux $\overline{\phi}_{y,w}$ provides an additional contribution to the momentum conservation equation:

$$\frac{\mathrm{d}}{\mathrm{d}y}\left((\mu+\mu_t)\frac{\mathrm{d}\overline{u}}{\mathrm{d}y}\right)=\frac{\mathrm{d}}{\mathrm{d}y}\left(\overline{\phi}_{y,w}\overline{u}\right), \tag{5.12}$$

Following Favre [Favre et al., 1966], we introduce the definition of suction rate A

$$\overline{\phi}_{y,w}=-\rho u_\infty A. \tag{5.13}$$

We are aware that the notation A for the suction rate may not be the best choice here as it could lead to confusion with the definition of the damping factor constant A^+. However we kept this notation to be consistent with Favre's work and tried to remove all ambiguity in the text. Moreover, as we will see below, although they correspond to different nondimensional parameters, there is in fact a strong relationship between the suction rate A and the damping factor constant A_+ used in the model.

Here we adapt the method from the previous section, taking into account the right-hand side term from (5.12).

We compute $\left[\frac{\mathrm{d}\alpha u}{\mathrm{d}y}\right]\Big|_n$ using a centered scheme as following:

$$\begin{aligned}\left[\frac{\mathrm{d}\alpha u}{\mathrm{d}y}\right]\Big|_n &= \frac{[\alpha u]|_{n+1}-[\alpha u]|_{n-1}}{y_{n+1}-y_{n-1}}\\ &= \frac{\alpha_{n+1}u_{n+1}-\alpha_{n-1}u_{n-1}}{y_{n+1}-y_{n-1}}\end{aligned}$$

In order to keep the good convergence properties of our previous iterative scheme, we

choose to treat the convective flux as a source term. This leads to the following algorithm:

Algorithm 2: Algorithm to compute the dynamic wall law with suction

calculate $\overline{\phi}_{y,w}$ from (5.13) and the given suction rate A;

initialize (u_n) by Eq.(5.10);

while *Convergence of* (u_n) *not reached* **do**

calculate $[\mu_t]$ from (5.2, 5.3, 5.4) using (u_n) ;

impose Dirichlet boundary condition (5.6) to obtain the linear system $A_{\text{BC}}(u_n) = B_{\text{BC}}$;

calculate the stiffness matrix $A_{\text{diff.}}$ of the LHS of (5.12) by (5.7);

calculate the RHS of (5.12) as a vector $B_{\text{conv.}}$;

solve the linear system $(A_{\text{BC}} + A_{\text{diff.}})(u_n) = B_{\text{BC}} + B_{\text{conv.}}$ to renew (u_n);

end

It is assumed that with suction (or blowing) effect, the mixing length is still given by the Van Driest model (5.3), however the parameter A^+ is expected to vary with the suction rate. This aspect has been recently examined by Lehmkuhl [Lehmkuhl et al., 2016], who proposed and adapted a model for the evolution of A^+ from Cebeci [Cebeci, 1970]:

$$A^+_{\text{Cebeci}} = A^+_{\text{vanDriest}} e^{-v_w^+ \cdot \delta_S^+}, \tag{5.14}$$

where according to Cebeci:

$$\delta_S^+ = 11.8, \tag{5.15}$$

and according to Lehmkuhl:

$$\delta_S^+ = 27 \cdot e^{-\left(\frac{-v_w^+ - 0.09}{0.09}\right)^2}. \tag{5.16}$$

We note that v_w^+ is the non-dimensional wall suction velocity which is related to the suction rate with

$$v_w^+ = \frac{v_w}{u_\tau} = -A\frac{u_\infty}{u_\tau}. \tag{5.17}$$

5.3.2 Results

The validation cases are based on Favre's experimental data [Favre et al., 1966], for which Reynolds averaging simulations (RAS) using two different low-Reynolds turbulence models (Launder-Sharma and Chien) have been already described and applied in the previous chapter. Results are also compared with those based on the analytical wall function (EQ. 2.78) proposed by Leduc [Leduc, 1995].

A first velocity profile calculated with the standard value $A^+ = 26$ in the Van Driest's model showed that our extended wall function method is not satisfactory when the suction rate is high. Correct values for A^+ were determined by fitting the results obtained with the ODE integration with the experimental data. Since the Van Driest model is limited to the near-wall region, only measurements corresponding to $y^+ < 200$ were kept in the fitting procedure.

In FIG. 5.2 and 5.3, ODE results (for both the impermeable ($A^+ = 26$) and best-fit damping factor constant A^+) are compared with experimental data, results from low-Reynolds turbulence models, as well as Leduc's analytical profile (inertial sub-layer part) for different suction rates. It shows that our extended wall function with the corrected damping factor significantly outperforms Leduc's analytical wall function in the near-wall region and to some extent the low Reynolds turbulence models. It should be noted that Leduc's model is close to Van Driest's original model with $A^+ = 26$. Although Leduc does not use Van Driest's model, he does not vary his lower bound for y^+ with the suction rate, which is equivalent to keeping the Van Driest damping factor constant independent to the suction rate. Another point to emphasize is that by construction, the wall function aims to capture the behavior in the wall region. Only the viscous and the inertial sub-layers and their transition are taken into account in the Van Driest model, which explains why unlike the RAS models, our ODE-based model is not capable to reproduce the ”rising tail” in the outer layer.

The values of the best-fit damping factor constants A^+, along with the friction velocity u_τ are shown in Table 5.1.

A	Fitted A^+	Experimental u_τ	Fitted u_τ	Experimental $-v_w^+$	Fitted $-v_w^+$
0.00000	28.7	0.475	0.360	0.0000	0.0000
0.00084	41.9	0.497	0.452	0.0185	0.0204
0.00119	45.2	0.515	0.489	0.0253	0.0267
0.00252	72.6	0.514	0.602	0.0537	0.0459
0.00516	114.9	0.725	0.799	0.0779	0.0709
0.01070	71.3	1.037	1.120	0.1130	0.1044
0.01420	38.6	1.215	1.289	0.1280	0.1210

Table 5.1: A^+ and u_τ for each fitted ODE result in Figures 5.2 and 5.3

The table also represents the non-dimensional aspiration velocity that can be directly deduced from u_τ using $-v_w^+$ by $-v_w^+ = Au_\infty/u_\tau$. The table shows that the predicted friction velocities agree with the experiments within 10%. This can be considered a good agreement, given the uncertainty in the experimental determination due to few measurements points in the viscous sublayer. This allows us to represent the variation of the best-fit damping factor constant A^+ as a function of $-v_w^+$ in FIG. 5.4 for direct comparison with Lehmkuhl's model and Cebeci's model.

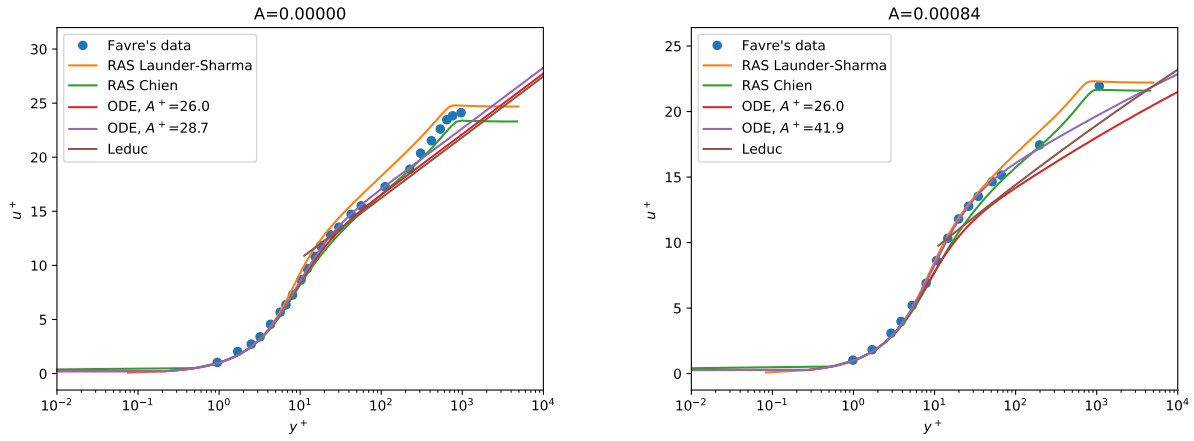

(a) A = 0.00000 (b) A = 0.00084

Figure 5.2: Velocity profiles for Favre's experimental data, RAS results using Launder-Sharma and Chien's model, Leduc's analytical model in inertial sub-layer and ODE solution with the no-suction $A^+ = 26$ and the best-fit damping factor constants: part 1

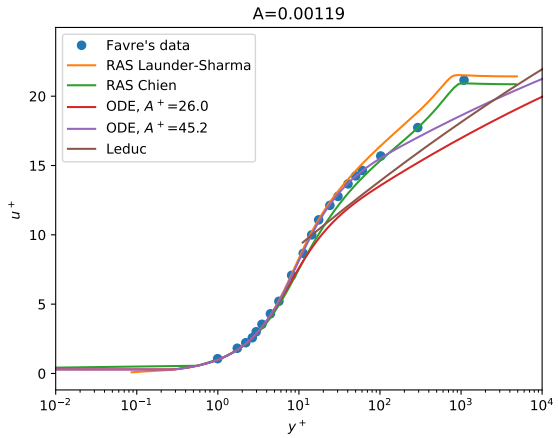

(a) A = 0.00119

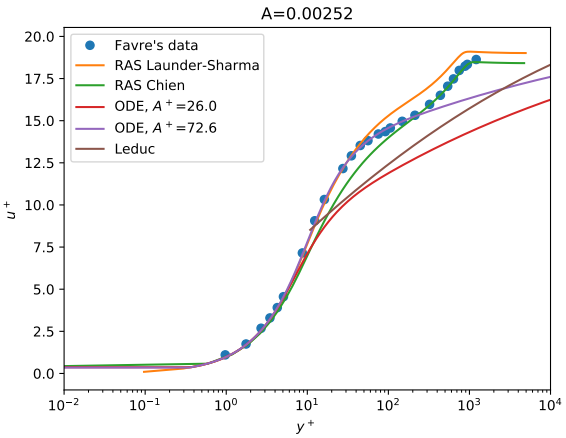

(b) A = 0.00252

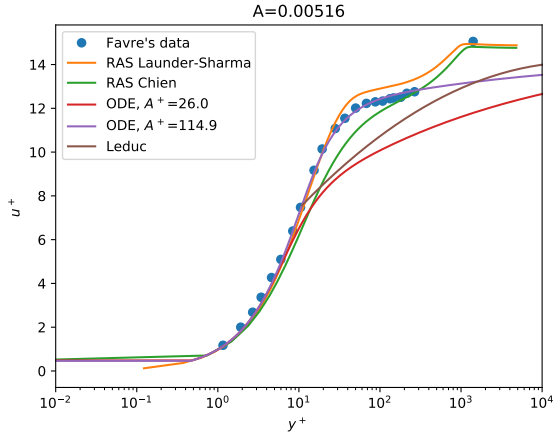

(c) A = 0.00516

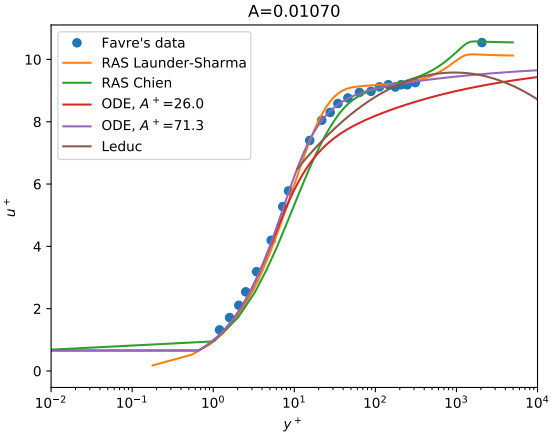

(d) A = 0.01070

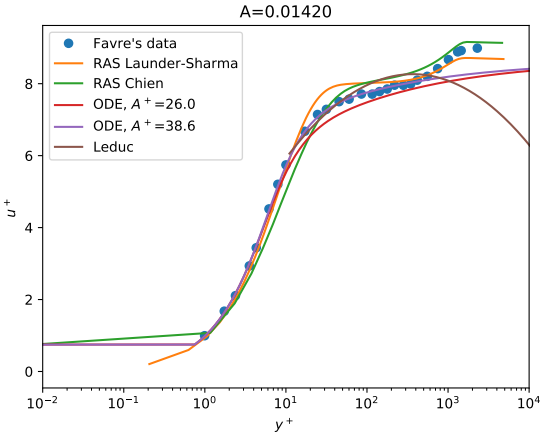

(e) A = 0.01420

Figure 5.3: Velocity profiles for Favre's experimental data, RAS results using Launder-Sharma and Chien's model, Leduc's analytical model in inertial sub-layer and ODE solution with the no-suction $A^+ = 26$ and the best-fit damping factor constants: part 2

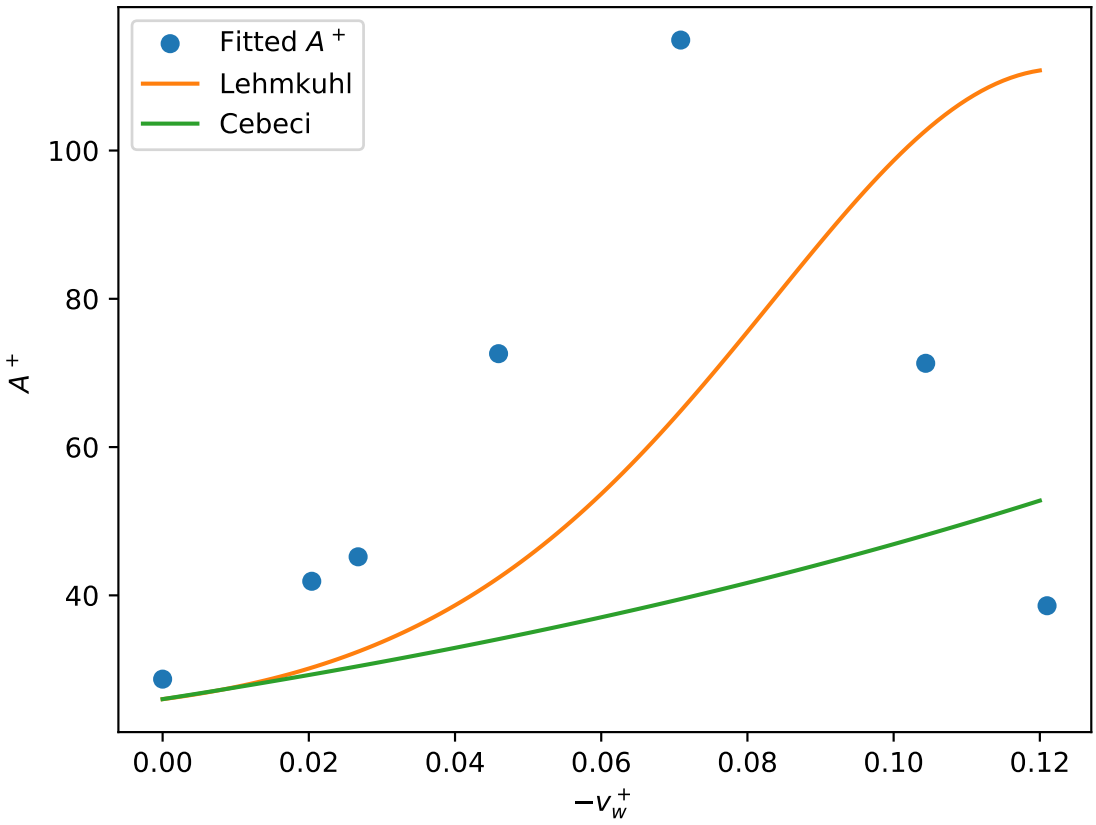

Figure 5.4: Variation of the damping factor constant A^+ with the dimensionless suction velocity $-v_w^+$: comparison of the best-fit value obtained in our ODE method with Lehmkuhl's model and Cebeci's model

For all approaches, the damping factor constant is seen to increase for low suction rates, albeit a stronger rate for Lehmkuhl compared to Cebeci and at an even stronger rate for our model. However, unlike Cebeci's and Lehmkuhl's models which predict a monotonic increase, the damping factor constant A^+ identified with our method shows a local maximum in the neighborhood of $-v_w^+ = 0.07$. Interestingly, this maximum seems to correspond to the value of the suction for which Favre noted the disappearance of the turbulent boundary layer and thus the relaminarisation of the boundary layer.

In all subsequent validation cases described in this chapter, the value of A^+ used in our model was adjusted from the data represented in FIG. 5.4. Wall suction was therefore considered a dominant effect to be taken into account by the wall function.

5.4 Simultaneous heat and mass transfer

By applying Favre's averaging and assuming that the turbulent contribution of interdiffusion is in form of $-\frac{\widetilde{c}_p \mu_t}{\mathrm{Pr}_{t,I}} \boldsymbol{\nabla} \widetilde{T}$ as proposed in Appendix D, one shall obtains the following boundary layer equations

$$\frac{\mathrm{d}}{\mathrm{d}y}\left[\left(\mu + \mu_t\right)\frac{\mathrm{d}\widetilde{u}}{\mathrm{d}y}\right] = \frac{\mathrm{d}}{\mathrm{d}y}\left(\overline{\phi}_w \widetilde{u}\right) \tag{5.18}$$

$$\frac{\mathrm{d}}{\mathrm{d}y}\left[\left(\overline{\rho} D + \frac{\mu_t}{\mathrm{Sc}_t}\right)\frac{\mathrm{d}\widetilde{Y}_v}{\mathrm{d}y}\right] = \frac{\mathrm{d}}{\mathrm{d}y}\left(\overline{\phi}_w \widetilde{Y}_v\right) \tag{5.19}$$

$$\frac{\mathrm{d}}{\mathrm{d}y}\left[\left(\lambda + \frac{\widetilde{c}_p \mu_t}{\mathrm{Pr}_t}\right)\frac{\mathrm{d}\widetilde{T}}{\mathrm{d}y}\right] = \frac{\mathrm{d}}{\mathrm{d}y}\left(\overline{\phi}_w \widetilde{c}_p \widetilde{T}\right) + \frac{\mathrm{d}}{\mathrm{d}y}\left[\overline{\rho}\widetilde{T} D \left(c_{p,v} - c_{p,a}\right)\frac{\mathrm{d}\widetilde{Y}_v}{\mathrm{d}y}\right] \tag{5.20}$$

with the ideal gas law assumed for the averaged properties

$$\overline{\rho} = \frac{P_{\mathrm{th}}}{\widetilde{r}\widetilde{T}}, \tag{5.21}$$

where

$$\widetilde{r} = r_a + (r_v - r_a)\widetilde{Y}_v, \tag{5.22}$$

$$r_k = \frac{R}{M_k}, \tag{5.23}$$

and the normal mass flux is given by Stefan's velocity

$$\overline{\phi}_w = -\frac{\rho_w D}{1 - Y_{v,w}} \left(\frac{\mathrm{d}\widetilde{Y}_v}{\mathrm{d}y} \right) \Bigg|_w . \tag{5.24}$$

The interdiffusion term may be discretized as matrix of $\widetilde{Y}_v$ or as vector based on $\widetilde{Y}_v$ from the last iteration. It could also be discretized as matrix of $\widetilde{T}$ but that could weaken the diagonal of the total matrix.

5.4.1 Physical modeling

The dynamic viscosities μ_i, the thermal conductivities λ_i, the heat capacities $C_{p,i}$ and the binary diffusion coefficient have already been described in Chapter 4. For the air/steam mixture properties, the following mixing rules are adopted.

For the dynamic viscosity, Sutherland [Sutherland, 1893] and Wilke [Wilke, 1950] suggested the following equation for gas mixtures:

$$\mu_{\mathrm{mix}} = \sum_{i=1}^{n} \frac{\mu_i}{1 + \frac{1}{X_i} \sum_{j=1, j \neq i}^{n} X_j \Phi_{ij}}, \tag{5.25}$$

with

$$\Phi_{ij} = \left[1 + \left(\frac{\mu_i}{\mu_j} \right)^{\frac{1}{2}} \left(\frac{M_j}{M_i} \right)^{\frac{1}{4}} \right]^2 \left[8 \left(1 + \frac{M_i}{M_j} \right) \right]^{-\frac{1}{2}} . \tag{5.26}$$

Likewise, Wassiljewa [Wassiljewa, 1904] introduced a mixture rule for the thermal con-

ductivity:

$$\lambda_{\text{mix}} = \sum_{i=1}^{n} \frac{\lambda_i}{1 + \frac{1}{X_i} \sum_{j=1, j \neq i}^{n} X_j A_{ij}}, \tag{5.27}$$

for which Mason and Saxena [Mason and Saxena, 1958] proposed the corresponding interaction parameter A_{ij}:

$$A_{ij} = \varepsilon \left[1 + \left(\frac{\lambda_{\text{tr},i}}{\lambda_{\text{tr},j}} \right)^{\frac{1}{2}} \left(\frac{M_i}{M_j} \right)^{\frac{1}{4}} \right]^2 \left[8 \left(1 + \frac{M_i}{M_j} \right) \right]^{-\frac{1}{2}}. \tag{5.28}$$

The interaction parameter A_{ij} is determined from the molecular weights M_i, the monoatomic values of the thermal conductivities $\lambda_{\text{tr},i}$ and the factor ε near unity. We employ the value of $\varepsilon = 1.0$ suggested by Poling et al. [Poling et al., 2001] and admit the relation

$$\frac{\lambda_{\text{tr},i}}{\lambda_{\text{tr},j}} = \frac{\mu_i}{\mu_j} \frac{M_j}{M_i}, \tag{5.29}$$

which leads to $A_{ij} = \Phi_{ij}$.

5.4.2 Algorithms

Similarly to the dynamic solver, we initialize the solution by:

$$u_n = u_w + \frac{y_n}{y_N} (u_b - u_w), \ n = 0, ..., N, \tag{5.30}$$

$$Y_{v,n} = Y_{v,w} + \frac{y_n}{y_N} (Y_{v,b} - Y_{v,w}), \ n = 0, ..., N, \tag{5.31}$$

$$T_n = T_w + \frac{y_n}{y_N} (T_b - T_w), \ n = 0, ..., N. \tag{5.32}$$

The boundary conditions write:

$$u_0 = u_w,\ u_N = u_b, \tag{5.33}$$

$$Y_{v,0} = Y_{v,w},\ Y_{v,N} = Y_{v,b}, \tag{5.34}$$

$$T_0 = T_w,\ T_N = T_b. \tag{5.35}$$

$$\tag{5.36}$$

The computation of the wall laws of a simultaneous heat and mass transfer with condensation may be carried out using Algorithm 3.

When there is only one species, Algorithm 3 could be simplified as Algorithm 4

Algorithm 3: Algorithm to compute the wall laws of velocity, mass fraction and temperature of the simultaneous heat and mass transfer with condensation

calculate $\overline{\phi}_{y,w}$ from (5.24) and the given A;
initialize (u_n) by Eq.(5.30, $(Y_{v,n})$ by Eq. (5.31), (T_n) by Eq. (5.32);
while *Convergence of* (u_n), $(Y_{v,n})$ *and* (T_n) *not reached* **do**
  calculate $[\mu_t]$ from (5.2, 5.3, 5.4) using (u_n) ;
  `// renew` (u_n)
  impose Dirichlet boundary condition (5.33) to obtain the linear system $A_{u,\text{BC}}(u_n) = B_{u,\text{BC}}$;
  calculate the stiffness matrix $A_{u,\text{diff.}}$ of the LHS of (5.18) by (5.7);
  calculate the RHS of (5.18) as a vector $B_{u,\text{conv.}}$;
  solve the linear system $(A_{u,\text{BC}} + A_{u,\text{diff.}})(u_n) = B_{u,\text{BC}} + B_{u,\text{conv.}}$ to renew (u_n);
  `// renew` $(Y_{v,n})$
  impose Dirichlet boundary condition (5.34) to obtain the linear system $A_{Y,\text{BC}}(Y_{v,n}) = B_{Y,\text{BC}}$;
  calculate the stiffness matrix $A_{Y,\text{diff.}}$ of the LHS of (5.19) by (5.7);
  calculate the RHS of (5.19) as a vector $B_{Y,\text{conv.}}$;
  solve the linear system $(A_{Y,\text{BC}} + A_{Y,\text{diff.}})(Y_{v,n}) = B_{Y,\text{BC}} + B_{Y,\text{conv.}}$ to renew $(Y_{v,n})$;
  `// renew` (T_n)
  impose Dirichlet boundary condition (5.35) to obtain the linear system $A_{T,\text{BC}}(T_n) = B_{T,\text{BC}}$;
  calculate the stiffness matrix $A_{T,\text{diff.}}$ of the LHS of (5.20) by (5.7);
  calculate the RHS of (5.20) as a vector $B_{T,\text{conv.}}$;
  solve the linear system $(A_{T,\text{BC}} + A_{T,\text{diff.}})(u_n) = B_{T,\text{BC}} + B_{T,\text{conv.}}$ to renew (T_n);
end

Algorithm 4: Algorithm to compute the wall laws of velocity and temperature of the heat transfer with suction

calculate $\overline{\phi}_{y,w}$ from (5.13) and the given A;
initialize (u_n) by Eq.(5.30, $(Y_{v,n})$ by Eq. (5.31), (T_n) by Eq. (5.32);
while *Convergence of* (u_n), $(Y_{v,n})$ *and* (T_n) *not reached* **do**
  calculate $[\mu_t]$ from (5.2, 5.3, 5.4) using (u_n) ;
  `// renew` (u_n)
  impose Dirichlet boundary condition (5.33) to obtain the linear system $A_{u,\text{BC}}(u_n) = B_{u,\text{BC}}$;
  calculate the stiffness matrix $A_{u,\text{diff.}}$ of the LHS of (5.18) by (5.7);
  calculate the RHS of (5.18) as a vector $B_{u,\text{conv.}}$;
  solve the linear system $(A_{u,\text{BC}} + A_{u,\text{diff.}})(u_n) = B_{u,\text{BC}} + B_{u,\text{conv.}}$ to renew (u_n);
  `// renew` (T_n)
  impose Dirichlet boundary condition (5.35) to obtain the linear system $A_{T,\text{BC}}(T_n) = B_{T,\text{BC}}$;
  calculate the stiffness matrix $A_{T,\text{diff.}}$ of the LHS of (5.20) by (5.7);
  calculate the RHS of (5.20) as a vector $B_{T,\text{conv.}}$;
  solve the linear system $(A_{T,\text{BC}} + A_{T,\text{diff.}})(u_n) = B_{T,\text{BC}} + B_{T,\text{conv.}}$ to renew (T_n);
end

5.4.3 Turbulent boundary layer with suction and heat transfer

In this section we now consider a turbulent boundary layer with both suction and heat transfer. Substantial work was done on this subject in the 1970s, with in particular the experimental studies of Verollet [Verollet, 1972] and Fulachier [Fulachier et al., 1977]. The latter provides scaled velocity and temperature normal profiles for a turbulent boundary layer with suction and wall heating, which we will use to test the prediction of our extended wall function. We have selected a case where both boundary layers are fully developed, i.e. the onset of heating coincides with the onset of the dynamic boundary layer. In this case, the flow velocity is 12 m/s and the temperature difference between the wall and the channel is $22°$C. The fluid is air under atmospheric pressure and injected at room temperature ($20°$C). We focus on three cases corresponding to suction rates A of 0, 0.0015 and 0.0030.

Accounting for thermal effects requires the definition of a turbulent Prandtl number Pr_t. We chose the usual value of 0.9, which is traditionally used for shear flows. As

noted above, the value of A^+ was determined from the suction rate A using our previous calculations without heat transfer. One first estimated u_τ from a calculation without suction ($A^+ = 26$) and we used this value to compute $-v_w^+$, from which we look up the appropriate value of A^+ from FIG. 5.4. A corrected value of u_τ could then be obtained from the new value of the damping factor constant A^+. These values are given in TAB. 5.2. These test conditions are below the threshold value for relaminarisation and correspond to moderate suction. According to the data in [Verollet, 1972], it is possible to estimate the friction velocity deduced from the experiments: $u_\tau = 0.523$ m/s for $A = 0.0015$ and $u_\tau = 0.609$ m/s for $A = 0.0030$. These values are in good agreement with the numerical predictions, especially as few points are available below $y^+ = 20$ in the experiments to compute the velocity.

A	A^+	$-v_w^+$	u_τ
0.0000	26	0.0000	0.4175
0.0015	26	0.0290	0.6214
0.0015	40	0.0299	0.6019
0.0030	26	0.0466	0.7733
0.0030	75	0.0489	0.7359

Table 5.2: A^+ used in the computations corresponding to Fulachier's experiments, and predicted values of $-v_w^+$ and u_τ

The predictions of our model are compared with the experimental results in FIG. 5.5.

Profiles obtained with the damping factor constant value from FIG. 5.4 show a good agreement with the experimental data. Our conclusion is that the extended wall function where the damping factor constant is solely adjusted for the suction rate provides a good prediction of a turbulent boundary layer with suction and heat transfer.

5.4.4 Filmwise condensation boundary layer in the COPAIN tests

In this section, we validate our model for filmwise condensation using results from the COPAIN experiments and comparing our predictions with a low Reynolds turbulence model.

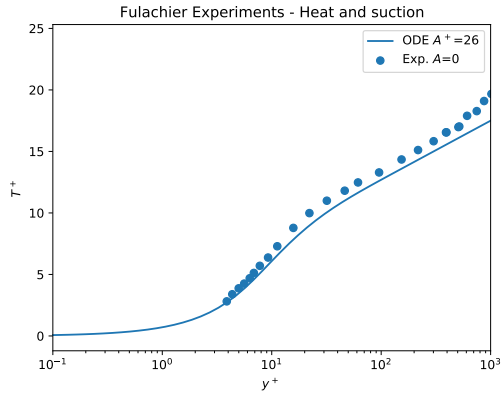

(a) T^+ as function of y^+, $A = 0$, $A^+ = 26$

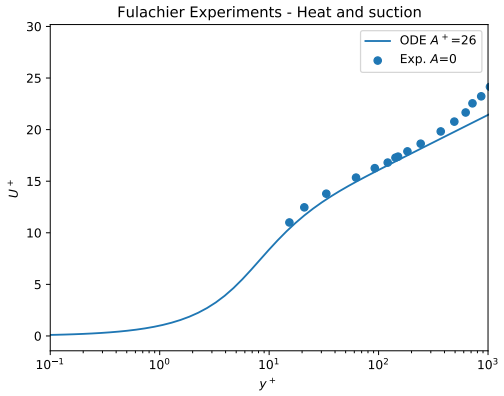

(b) U^+ as function of y^+, $A = 0$, $A^+ = 26$

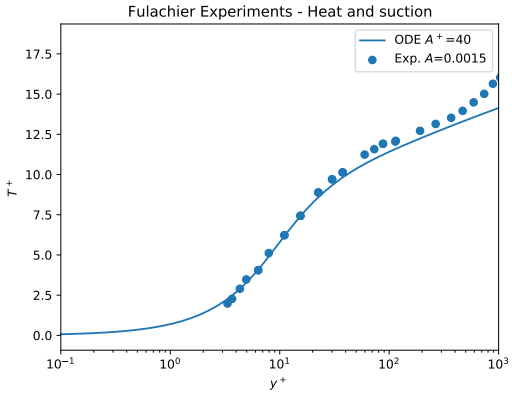

(c) T^+ as function of y^+, $A = 0.0015$, $A^+ = 40$

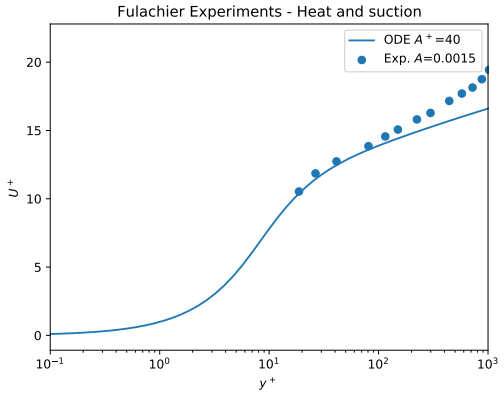

(d) U^+ as function of y^+, $A = 0.0015$, $A^+ = 40$

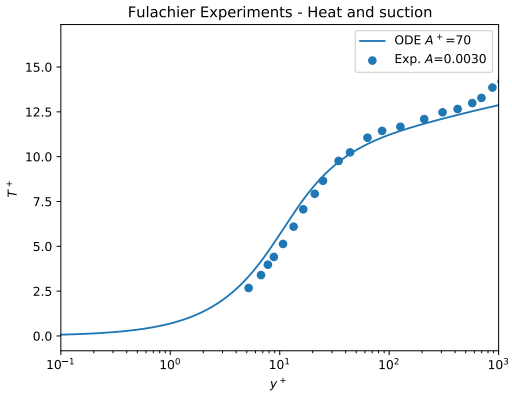

(e) T^+ as function of y^+, $A = 0.0030$, $A^+ = 75$

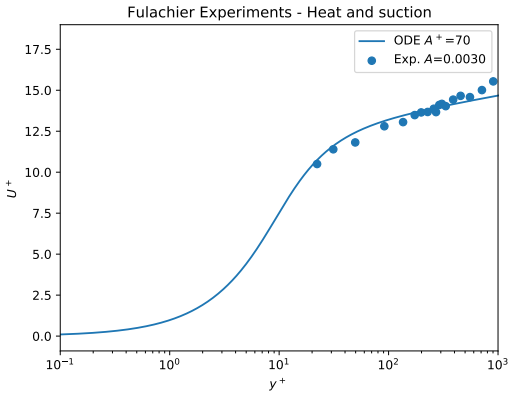

(f) U^+ as function of y^+, $A = 0.0030$, $A^+ = 75$

Figure 5.5: Velocity and temperature profiles for a boundary layer with heat transfer and suction - comparison with Fulachier experiments (cite: Fulachier)

As in the previous section, we choose to adjust the damping factor constant exclusively based on the suction rate. The four selected validation cases are characterized by a moderate suction rate, far from the relaminarisation observed by Favre. Their characteristics are given in TAB. 2.2 (Section 2.3).

As previously, we take $\mathrm{Pr}_t = 0.9$. Since we now have to account for mass transfer, we need to define a turbulent Schmidt number. The range of Schmidt numbers used in the literature is typically 0.5-1.3. We select the value $\mathrm{Sc}_t = 1.2$.

An important question is the determination of the friction velocity u_τ and its possible dependence on interdiffusion. Computations corresponding to different COPAIN test cases were carried out for various values of the damping factor constant, as well as with and without including the effect of interdiffusion. Results are reported in Table 5.3. Using a damping factor constant adjusted for the suction rate results in a decrease by about 10% in the friction velocity compared with the standard value. The effect of interdiffusion was much smaller, but still noticeable, particularly in the natural convection case (P071). We note that for the computations the boundary conditions in the bulk were taken from experimental measurements within the wall layer, since, as noted before, the wall function aims to describe the inner wall region.

The global results of the COPAIN tests with the ODE solver are reported in TAB. 5.4. Note that for the experiments, only the total heat flux through the condensing plate is measured. In order to obtain the sensible heat flux contribution and the mass flux from the global measurements, we used a method proposed by Bucci, and we developed a extension of that method in order to take interdiffusion into account. Details of the method are given in Appendix E.

TAB. 5.4 provides a comparison of the experimental fluxes partitioned with Bucci's method (exp Bucci), the experimental fluxes partitioned with the correction for interdiffusion (exp i.d.), the fluxes obtained with Chien's low Reynolds turbulence model (CH) and

Test	Solver	A^+	$-v_w^+$	u_τ
P064	noID	26	0.0021	0.1601
P064	w_ID	26	0.0021	0.1611
P064	noID	30	0.0020	0.1541
P064	w_ID	30	0.0020	0.1551
P066	noID	26	0.0050	0.0606
P066	w_ID	26	0.0050	0.0610
P066	noID	35	0.0046	0.0556
P066	w_ID	35	0.0047	0.0559
P070	noID	26	0.0258	0.1166
P070	w_ID	26	0.0259	0.1173
P070	noID	45	0.0230	0.1019
P070	w_ID	45	0.0230	0.1024
P071	noID	26	0.0386	0.0650
P071	w_ID	26	0.0385	0.0653
P071	noID	55	0.0323	0.0496
P071	w_ID	55	0.0321	0.0532
P071	noID	50	0.0332	0.0547
P071	w_ID	50	0.0329	0.0548

Table 5.3: A^+ used in the computations corresponding to the COPAIN test and predicted values $-v_w^+$, here "noID" means "no interdiffusion" while "w_ID" means "with interdiffusion"

those predicted by our ODE solver with (ODE i.d.) and without interdiffusion (ODE). It can be seen that while the sensible flux obtained with Bucci's original method is relatively small, implementation of the interdiffusion correction leads to a larger sensible heat flux, although it is still small compared with the latent heat flux. We can also see that our model overall predicts a larger sensible heat flux when interdiffusion is accounted for than when it is omitted. However both versions of the model predict similar mass fluxes.

For test P064 corresponding to forced convection, a very good consistency is shown between the result of our ODE solver with interdiffusion and the experimental data corrected for interdiffusion. When buoyancy effects become significant, the predicted fluxes are less consistent with the experiments, which is not surprising since the model has been derived for forced convection, however numerical predictions taking into account interdiffusion remain in a reasonable range. We note that the RAS model incorporates species interdiffusion through an additional turbulent diffusion term following [Bucci, 2009]. The RAS model with interdiffusion also predicts an increase of the sensible heat flux which is

Test	Data	Φ_{tot} (W/m^2)	Φ_{conv} (W/m^2)	$\dot{m}_v$ (10^{-6} kg/m^2/s)
P064	exp. Bucci	1175	207	409
P064	exp. i.d	1175	298	371
P064	CH	1123	303	347
P064	ODE no i.d.	1104	222	373
P064	ODE i.d.	1181	289	377
P066	exp. Bucci	835	106	305
P066	exp. i.d	835	175	277
P066	CH	680	149	223
P066	ODE no i.d.	916	133	328
P066	ODE i.d.	983	194	331
P070	exp. Bucci	22416	620	10189
P070	exp. i.d	22416	4687	8288
P070	CH	—	—	—
P070	ODE no i.d.	23790	1867	10249
P070	ODE i.d.	27290	5242	10307
P071	exp. Bucci	18976	596	8475
P071	exp. i.d	18976	3716	7036
P071	CH	20916	4172	7660
P071	ODE no i.d.	21559	2359	8853
P071	ODE i.d.	23536	4448	8801

Table 5.4: ODE Solver: Global results of the COPAIN tests of total heat flux, sensible heat flux and mass flux (—: Not Calculated): exp. Bucci: Sensible heat flux obtained from Bucci's method; exp. i.d.: Sensible heat flux obtained from the extension of Bucci's method for interdiffusion; CH: Chien Turbulent model; ODE no i.d.: Extended wall function without interdiffusion; ODE i.d.: Extended wall function with interdiffusion

however lower than the one predicted by our ODE solver.

Numerical and experimental results for the temperature, velocity and mass fraction profiles are compared in a series of figures for the following COPAIN test cases: P064 (FIG. 5.6), P066 (FIG. 5.7), P070 (FIG. 5.8) and P071 (FIG. 5.9). We recal that no velocity profile is available in the experiment, so it is only possible to compare our prediction with the low Reynolds turbulence model of Chien. For each case, both dimensional and non-dimensional representations are shown. Since it is not available in the experiment, we use the friction velocity u_τ predicted by the ODE model with interdiffusion to compute the non-dimensional experimental fluxes, which are recovered from the measured fluxes using a reconstruction method that is corrected for interdiffusion.

In non-dimensional units, the temperature profiles predicted by the model with interdiffusion (orange curve) are generally in good agreement with those from the RAS model (green curve), and are strongly different from those predicted by the model without interdiffusion (blue curve). The agreement is not as good for the mass fraction, although some similarity between our model and the RAS model is still present. The observed discrepancy could be the consequence of the inaccuracy of the measurement of concentration. This point has already been discussed in the thesis of M. Bucci claiming that the gas sampling technique used in the experiments has a sampling velocity which is not small compared to the Stefan velocity. The measurement technique is likely to be intrusive and to perturb the boundary layers. The underprediction could also be partly explained by the fact that the thickness of the viscous sub-layer may be over-estimated. This will lead to an under-estimation of u_τ and therefore an over-prediction of the experimental data when expressed in non-dimensional variables. However, the lack of agreement could also be due to the limitations of our model, which we discuss in the next section.

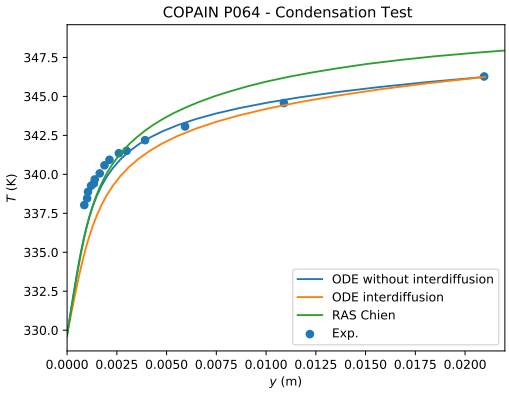

(a) dimensional temperature profile

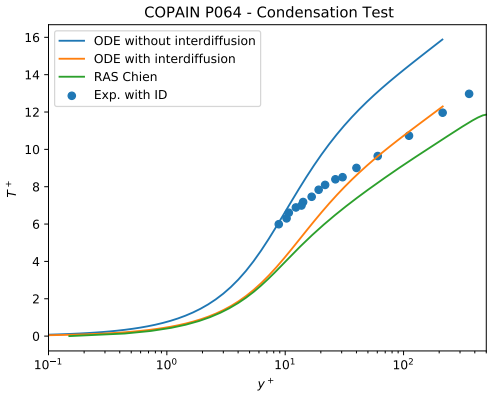

(b) dimensionless temperature profile

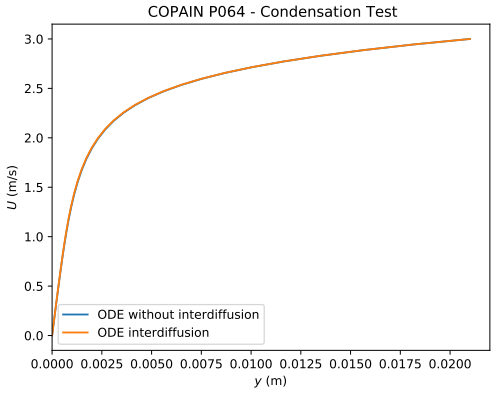

(c) dimensional velocity profile

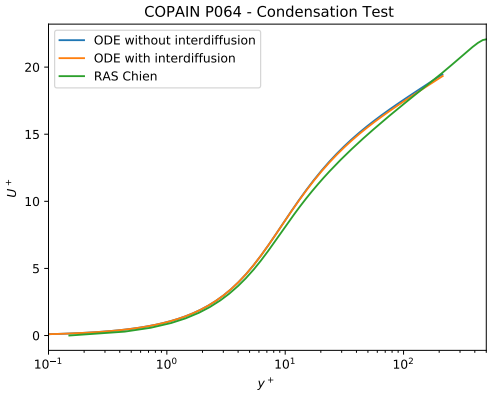

(d) dimensionless velocity profile

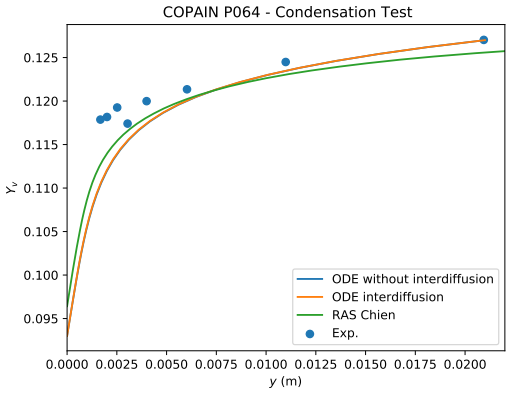

(e) dimensional mass fraction profile

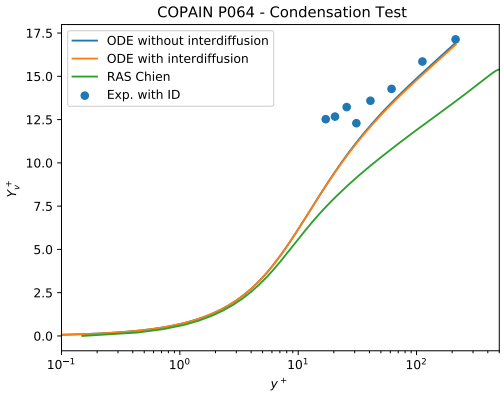

(f) dimensionless mass fraction profile

Figure 5.6: Numerical predictions of the temperature, velocity and mass fraction profile for the experimental data P064 of COPAIN facility [Bazin and Castelli, 2000]

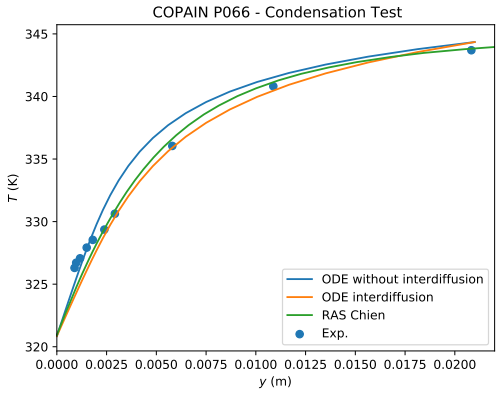

(a) dimensional temperature profile

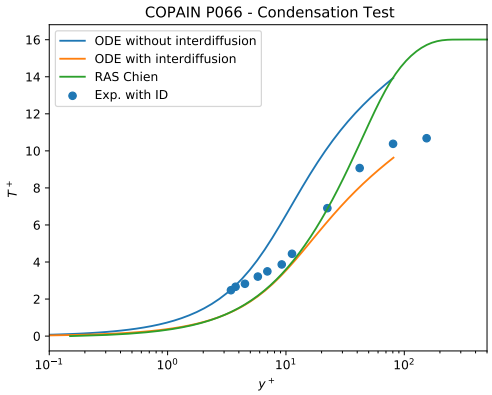

(b) dimensionless temperature profile

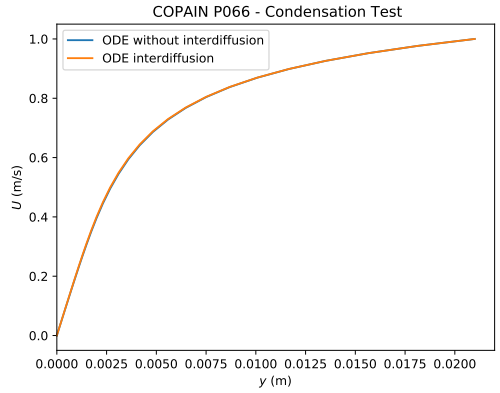

(c) dimensional velocity profile

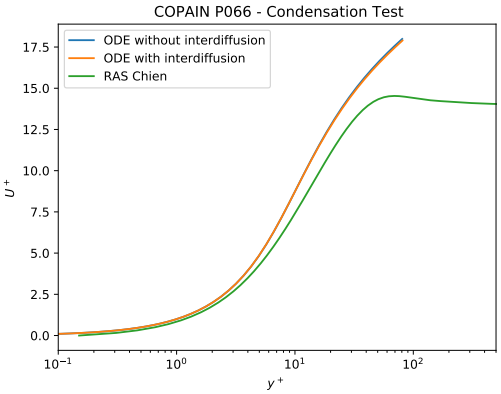

(d) dimensionless velocity profile

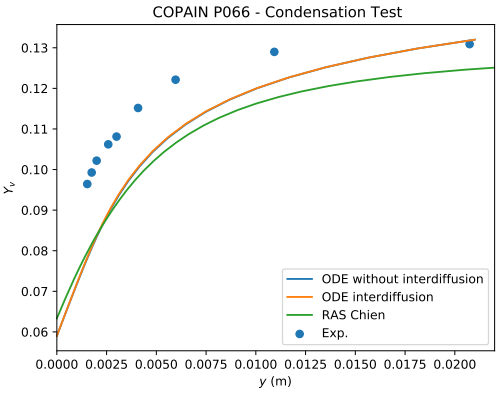

(e) dimensional mass fraction profile

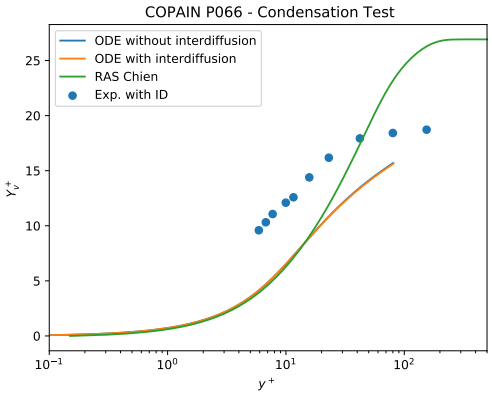

(f) dimensionless mass fraction profile

Figure 5.7: Numerical predictions of the temperature, velocity and mass fraction profile for the experimental data P066 of COPAIN facility [Bazin and Castelli, 2000]

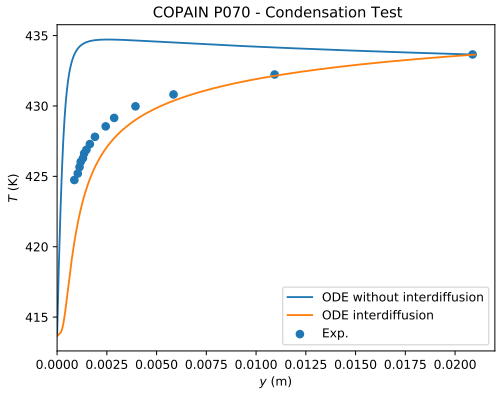

(a) dimensional temperature profile

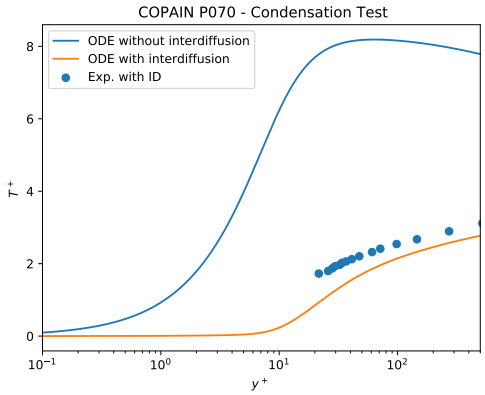

(b) dimensionless temperature profile

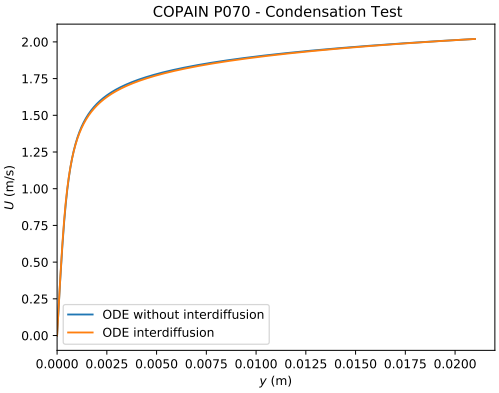

(c) dimensional velocity profile

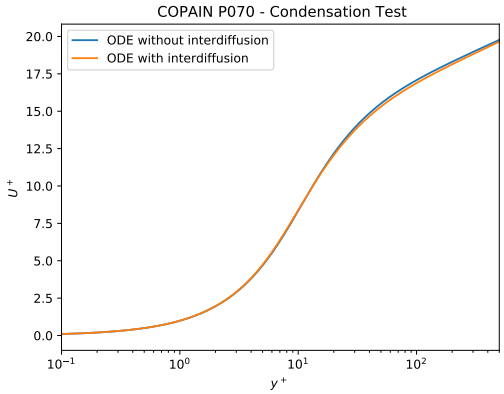

(d) dimensionless velocity profile

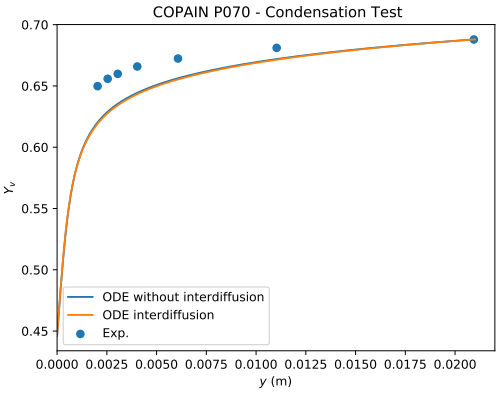

(e) dimensional mass fraction profile

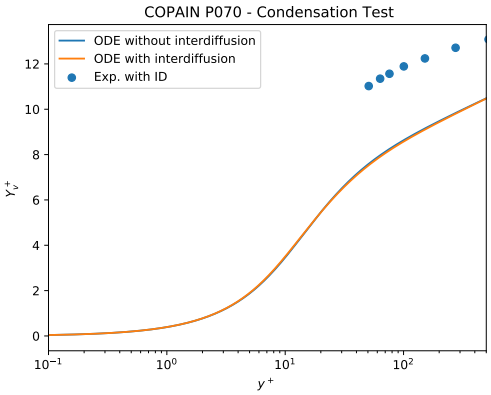

(f) dimensionless mass fraction profile

Figure 5.8: Numerical predictions of the temperature, velocity and mass fraction profile for the experimental data P064 of COPAIN facility [Bazin and Castelli, 2000]

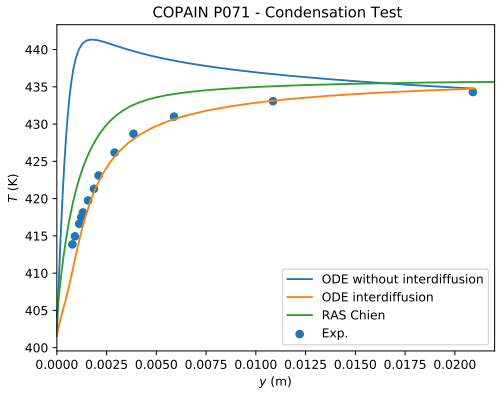

(a) dimensional temperature profile

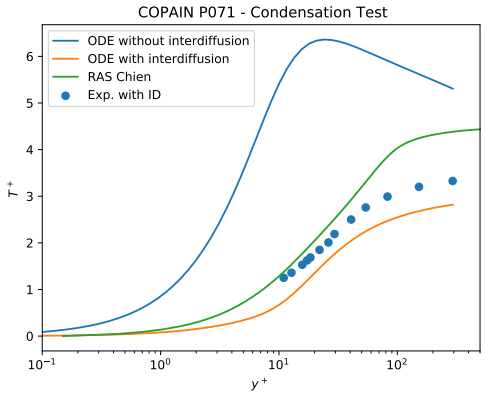

(b) dimensionless temperature profile

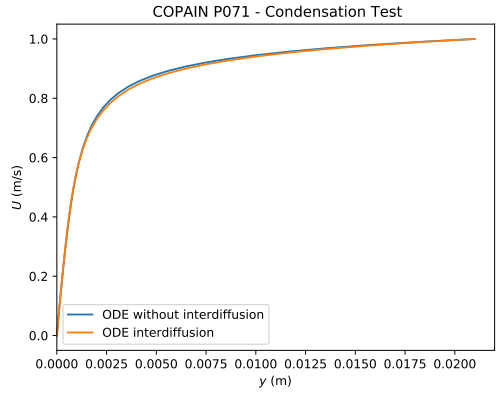

(c) dimensional velocity profile

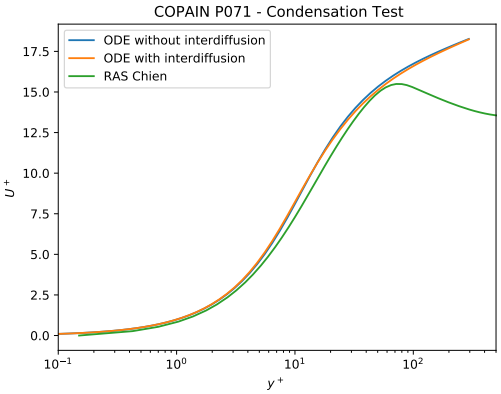

(d) dimensionless velocity profile

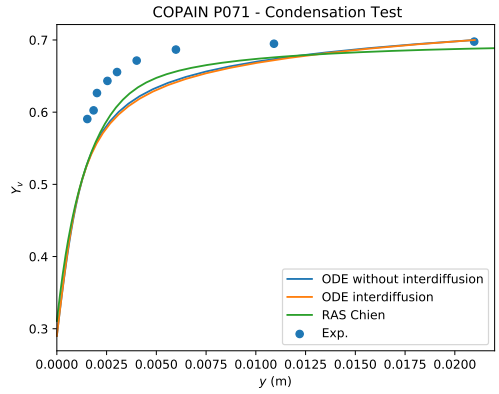

(e) dimensional mass fraction profile

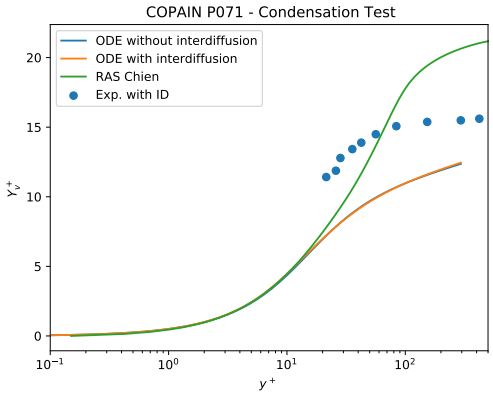

(f) dimensionless mass fraction profile

Figure 5.9: Numerical predictions of the temperature, velocity and mass fraction profile for the experimental data P071 of COPAIN facility [Bazin and Castelli, 2000]

5.5 Patankar-Spalding model: a better option for the damping factor?

In this section we discuss the limitations of our approach. Our derivation requires that EQ. 5.3 should be compatible with $\tau = \tau_w$. However this is not the case when a suction or blowing effect occurs at the wall. The correct relationship should write $\tau^+ = 1 + v_w^+ (u^+ - u_w^+)$. Thus, searching a different but still constant A^+ to correct the van Driest damping factor still needs a theoretical justification.

However, in order to allow for a variable damping factor, a possible correction of the van Driest model could be the Patankar-Spalding model [Landis and Mills, 1972; Meinert et al., 2001], in which the damping factor is defined as follows:

$$\begin{aligned} D_F &= 1 - \exp\left[\frac{y^+}{A^+}\frac{\sqrt{\tau/\rho}}{\sqrt{\tau_w/\rho_w}}\right] \\ &= 1 - \exp\left[\frac{y^+}{A^+}\sqrt{\frac{\rho_w}{\rho}\left(1 + v_w^+ u^+\right)}\right]. \end{aligned} \tag{5.37}$$

To complete the mixing length model, it is also calculated that:

$$\frac{\mathrm{d}u^+}{\mathrm{d}y^+} = \frac{2\left(\rho_w/\rho\right)\left(1 + v_w^+ u^+\right)}{1 + \sqrt{1 + 4\kappa^2 y^{+2} D_F^2 \left(\rho_w/\rho\right)\left(1 + v_w^+ u^+\right)}}. \tag{5.38}$$

It can be seen that this model is equivalent to a van Driest type mixing length model with A^+ as function of y^+. We note that the model could be able to take the variation of the density ρ into account, which might enable us to model more accurately the turbulence with heat and mass transfer. For all these reasons, it seems a good idea to implement this model in the current ODE solver, and to compare the results with those displayed in figure 5.4. This will be the object of future work.

5.6 Conclusions of the chapter

In this chapter, we derive extended wall functions that are able to take into account coupled heat and mass transfer. The procedure is based on an assumption of wall equilibrium in the conservation equations, which results in a system of 1-D ordinary differential equations which depend on the wall distance. Turbulent effects are modelled with a mixing length model with a Van Driest damping factor. The thermophysical properties of the mixture are allowed to vary in space. The wall function is then obtained by numerical integration. Validation of the approach is carried out for a series of test cases of increasing complexity. We first show that a very good agreement is obtained with existing experimental, theoretical and computational results in the inner layer of a turbulent boundary layer without heat or mass transfer at the wall.

We then consider the case of wall suction with which condensation is modelled. A main result is that the constant in the Van Driest damping factor then needs to be adjusted for the suction rate. The modified damping factor constant was determined by fitting Favre's experimental data and compared with the models of Cebeci and Lehmkuhl. These models both predict a monotonic increase in the damping factor constant with the suction rate, but the increase is much larger in the case of Lehmkuhl at high suction rate. Our empirical coefficient, however, is found to be increasing at low suction rates even faster than the Lehmkuhl's prediction, go through a maximum for an intermediate value of the suction rate, then decrease towards levels that are consistent with Cebeci. The suction value corresponding to the maximum damping factor constant appears to correspond to boundary layer relaminarization.

The last series of tests corresponded to coupled heat and mass transfer. As a first step, we considered suction combined with heat transfer and obtained a good agreeement between our model and Fulachier's experimental data. Results predicted by our solver were then compared with the low Reynolds models and with the COPAIN experiments. A much

better agreement with the experimental results was obtained when species interdiffusion effects were included in the wall function model. This clearly demonstrates the importance of taking interdiffusion into account in the wall model.

Chapter 6

Conclusions and perspectives

6.1 Conclusions

Setting Steam condensation phenomena in the presence of non-condensable gases involves several complex phenomena. Prediction of the heat and mass transfer therefore requires modelling which offers a good compromise between accurate description of the physics and numerical tractability. Identifying and quantifying the importance of cross-coupling effects between different physical quantities is a key ingredient of the modelling effort. The objective of the thesis is to contribute to this effort, with a particular focus on the often forgotten effect of species interdiffusion. This effect is usually neglected in studies without a proper justification.

Laminar case A first study of the influence of interdiffusion was carried out in a natural convection case and described in Chapter 3. The flow was assumed to be laminar. The configuration of interest was a 2-D square, differentially heated cavity containing a binary mixture of a condensable and a non-condensable gas. Condensation was modelled by a Stefan's velocity at the wall. The model was implemented into the OpenFOAM solver.

A numerical treatment for the boundary condition based on the air partial velocity was implemented in the solver in order to improve the robustness of the PISO algorithm. Our approach was validated on different test cases. We found that species interdiffusion represented a significant contribution to the sensible heat flux when the mass flux was large and the difference between the heat capacity of the two species contribution was noticeable. In addition, the influence of other cross-coupling phenomena such as the Soret and Dufour effects was examined. It was found that these two effects could be neglected for an air-steam mixture.

Turbulent case: low Reynolds models Most configurations of interest are characterized by turbulence. Turbulence models therefore need to be included in the modelling strategy. Consequently, we examined in Chapter 4 how low Reynolds models can be extended in order to accommodate for additional physics. We implemented two models: Chien and Launder-Sharma. We then compared their predictions with experimental data. Validation was carried out for a classical boundary layer, a boundary layer with suction, and a boundary layer with coupled heat and mass transfer corresponding to test cases in the COPAIN experiment. It was found that low Reynolds models could successfully capture the influence of suction. We then consider the case of filmwise condensation, for which only limited experimental data exists. In particular, it was not possible to determine an experimental friction velocity, which makes it difficult to identify correct scales to normalize the profiles. We note that only the total heat flux was measured in the experiment, and its partition into a sensible and a latent contribution relied on a splitting procedure that did not take interdiffusion into account. Nevertheless, despite these limitations, we concluded that the profiles predicted by the low Reynolds turbulence models could be used as a reference to be confronted with the extended wall function results that were obtained in the following chapter.

Turbulent case: extended wall functions Low Reynolds numbers are good predictive tools, but the computational expense associated with the mesh size they require constitutes a severe limitation to their practical application. An alternative that we examine in Chapter 5 is to derive extended wall functions to predict the mean profiles in the wall region. All physical properties are allowed to vary spatially. The model relies on the mixing length assumption, and features a Van Driest damping factor. In agreement with previous studies, the Van Driest factor is observed to depend on the suction rate at the wall. The dependence of the constant in the Van Driest damping factor was determined from fits with Favre's experimental data. It was seen to reach maximum for a relative suction rate of $A \approx 0.005$. The variations of the damping factor were found to be different from Cebeci's and Lemkuhl's approaches for low suction rates.

Using a suction-dependent damping factor constant, the model was then solved for a boundary layer with both suction and heat transfer and compared with Fulachier's experimental data. A good agreement was obtained. Finally, the last validation case consisted of a boundary layer with both heat and mass transfer corresponding to some test cases of the COPAIN experiments. A good agreement was also obtained, especially for cases where natural convection was limited. Comparison of the solver results with and without interdiffusion showed that it is essential to include this phenomenon in order to predict the heat flux correctly.

6.2 Perspectives

The work described in this thesis provides a certain level of understanding of the boundary layer of a filmwise condensation using the ODE solver. However, due to the hypotheses made, the current model could be improved in different aspects.

The first improvement could be related to the Van Driest damping factor used in the

solver, which assumes that the shear stress τ is constant in the boundary layer. In fact, the shear stress should vary linearly with respect to the distance to the wall due to the suction velocity. Patankar and Spalding have recommended a model which is capable to take this issue into account [Patankar, 1967; Landis and Mills, 1972], as well as the variation of density. In the future work, the Patankar-Spalding damping factor could be used in the place of the current one.

The second aspect is about the modelling of the turbulent contribution of species interdiffusion. Since the turbulent Prandtl number remains the same as in purely thermal transfer, the current ODE solver takes only the molecular effect of the interdiffusion, like in the work of Muto et al. [Muto et al., 2019]. However, in the thesis of Bucci [Bucci, 2009], a turbulent contribution is added to the mass transfer in the interdiffusion term, as in the RAS with low-Reynolds turbulence model in this thesis. The same choice could also be made for the improvement of the ODE solver. Moreover, in Appendix D, it is shown that the turbulent contribution of interdiffusion could be modelled by the same form of that of the Fourier's law, which will not change the form of the equation but only the value of turbulent Prandtl number, which has not been investigated in the present work.

It is also reported that the turbulent Prandtl and Schmidt numbers could depend on the distance to the wall [Magalhães et al., 2019], which is not discussed in the thesis. Although precise prediction is proposed for the turbulent Prandtl number [Srinivasan and Papavassiliou, 2011], the turbulent Schmidt number varies in a very large range. The influence of these numbers needs to be investigated.

The validation of the ODE solver needs also correct data coming from whether experiments or direct numerical simulations (DNS). In the experimental aspect, precise measurements of the velocity, the temperature and the composition of the gas profiles are greatly needed at the same location and for different convection regimes. On the other hand, DNS results like the one proposed by [Bahavar and Wagner, 2020] could also be used to compare with the results of the current ODE model.

In the work described in this dissertation, the liquid film is neglected because of its assumed low thermal resistance. This hypothesis corresponds to a high concentration of non-condensable as well as a high resistance to the steam flux to the wall. Low pressure tests in the COPAIN database correspond to this situation. However, in other COPAIN tests performed at high steam partial pressure, high condensation flux leads to stronger resistance of the liquid film, which needs to be taken into account in our model.

Finally, since the current ODE solver is based on forced convection, the buoyancy should be taken into account when natural convection is dominant. It is possible to consider the gravitational acceleration as a source term based on the work proposed by Gerasimov [Gerasimov, 2003].

Appendix A

Nomenclature

Latin letters

Symbol	Significance
A	Suction rate
A^+	Damping factor constant
B	Driving force of condensation (Spalding mass number)
C	Constants
C_p	Constant pressure heat capacity
D	Diffusion coefficient
d	Lagrangian derivative
e, E	Internal Energy
F	Acceleration coefficient of boundary layer
f	Damping function in low Reynolds turbulent models
g	Gravity
Gr	Grashof number
H	Enthalpy
h	Heat/Mass transfer coefficient

Symbol	Significance
j, J	Mass diffusive Flux
k	Turbulent kinetic energy or thermal conductivity (figure)
l ou L	Length scale
Le	Lewis number
$\dot{m}$	Mass Flux
M	Molecular weight
Nu	Nusselt number
P	Pressure
P_k	Production of turbulent kinetic energy
Pr	Prandtl number
$\dot{q}$	Heat Flux
R	Pipe Radius or Perfect gas constant
$r_k = R/M_k$	k Species perfect gas constant
r	Radial Abscissa
Ra	Rayleigh number
Re	Reynolds number
Ri	Richardson number
S	Source term
Sh	Sherwood number
Sc	Schmidt number
T	Temperature
t	Time
U	Tangential velocity to the wall
V	Normal velocity to the wall or Volume
X	Molar fraction
x	Tangential coordinate to the wall
Y	Mass Fraction

Symbol	Significance
y	Normal coordinate to the wall

Greek Letters

Symbol	Significance
α,β	Sum on space dimensions
δ	Boundary layer thickness
Δ	Difference
ϵ	Turbulent kinetic energy dissipation
Φ	Weighting coefficient in gas mixture properties or heat flux
ϕ	Variables or mass flux
γ	Constant or isentropic coefficient
κ	Von-Karman constant
λ	Thermal conductivity (see k)
μ	Kinematic viscosity
ν	Dynamic viscosity
$\dot{\omega_k}$	Chemical source term of k species
Ω	Volume
Ψ	Prefactor in wall function analyses
ρ	Density
σ	Constant in turbulence model
θ	Dimensionless Temperature
τ	Shear stress tensor
∂	Partial derivative
$\boldsymbol{\nabla}$	Gradient operator
$\boldsymbol{\nabla\cdot}$	Divergence operator

Subscript

Symbol	Significance
a	Related to advection
air	Air
asp	Suction
b or ∞ or e	Bulk Conditions
C	Related to cold wall
conv	Convective
d or D	Related to diffusion
Dd	Dufour diffusion
DS	Dufour Soret
eff	Effective
fc	free convection
g	Refer to the first mesh close to the wall
H	Related to hot wall
i	Interface
id	Interdiffusion related to diffusion flux
iS	Interdiffusion related to Soret effect
in	Condition à Injection or Channel entrance boundary condition
inc or nc	non condensable gases
k	Chemical species
lat	Related to the latent heat
m	Mass or Mixture
μ	Related to viscosity
p	Related to peak pressure
ref	Reference
sat	Saturation
S	Soret

Symbol	Significance
t	Total or turbulent
T	Related to temperature
th	Thermodynamic
τ	Related to friction
v or vap	Steam
vi	Boundary of the viscous sublayer
w	Wall
y	Related to wall distance

Superscript

Symbol	Significance
~	Favre mean value
″	Fluctuations Favre averaging
′	Fluctuations Reynolds averaging
+	Dimensionless related to the wall boundary layer

Appendix B

Species interdiffusion

In fact, the species interdiffusion is an intrinsic phenomenon of coupling heat and mass transfer. One shall calculate the sum of the partial convective heat flux:

$$\begin{aligned}\sum_i \rho_i h_i \boldsymbol{U}_i &= \sum_i \rho_i h_i \left(\boldsymbol{U} - \frac{\boldsymbol{j}_i}{\rho_i} \right) \\ &= \rho h \boldsymbol{U} - \sum_i h_i \boldsymbol{j}_i\end{aligned}$$

In the result, $\rho h \boldsymbol{U}$ is the total convective heat flux. However, besides the total convective heat flux, there exists a second term $\sum_i h_i \boldsymbol{j}_i$ which is related to the specific enthalpy and the mass flux of each component. This is what we call the species interdiffusion in this work.

In practical, one writes

$$\sum_i h_i \boldsymbol{j}_i = \sum_i c_{p,i} T \boldsymbol{j}_i$$

which shows that the species interdiffusion is a phenomenon caused by mass flux between components with different heat capacities.

In this study, only two components are considered, thus the flux of species interdiffu-

sion is given by, since $\mathbf{j}_a = -\mathbf{j}_v$:

$$\begin{aligned}\mathbf{q}_{\text{i.d.}} &= c_{p,v} T \mathbf{j}_v + c_{p,a} T \mathbf{j}_a \\ &= \left(c_{p,v} - c_{p,a}\right) T \mathbf{j}_v\end{aligned}$$

Appendix C

Modified PISO implemented in OpenFOAM

All $*$ are omitted in this section. The low Mach equations developed in chapter 3 were numerically solved with the openFOAM package, which is an open source C++ toolbox for computational fluid dynamics. The core of the package is a velocity-pressure correction iterative solver which was originally devised for incompressible flows but has been extended to compressible flows. Among the available algorithms (SIMPLE, PIMPLE, PISO), we chose to use and adapt PISO (Pressure Implicit with Splitting of Operators). In PISO, the conservation of momentum is discretized as the following:

$$\mathcal{M}\boldsymbol{U}_{\text{int}} = \mathcal{A}\boldsymbol{U}_{\text{int}} + \mathcal{H} = -\frac{1}{\gamma_0}\nabla p_d \tag{C.1}$$

Solving the corresponding Poisson equation requires that the change in total mass be consistent with the velocity boundary conditions. This condition, however, is not systematically satisfied with the calculated temperature density and mass fraction because the thermodynamic pressure is imposed. The solution for this problem is to adjust the thermodynamic pressure according to the mass flux at the edges before solving the Poisson

equation.

The modified PISO algorithm is given as the following:

Algorithm 5: Modified PISO for low-Mach model in one time step

initialization;

while *in outer corrector loop* **do**

  calculate T and Y renew BCs;

  adjust P_{th} to meet continuity equation;

  calculate $\boldsymbol{U}_{\text{int}}$ by solving $\mathcal{M}\boldsymbol{U}_{\text{int}} = -\frac{1}{\gamma_0}\nabla p_d$;

  while *in inner corrector loop* **do**

    calculate T and Y renew BCs and adjust P_{th} to meet continuity equation;

    calculate p_d by solving $\nabla \cdot \left(\frac{1}{\gamma_0}\rho\mathcal{A}^{-1}\nabla p_d\right) = \nabla \cdot \left(\rho\mathcal{A}^{-1}\mathcal{H}\right) + \frac{\partial \rho}{\partial t} + \nabla \cdot (\rho \boldsymbol{U}_b)$;

  end

end

calculate new mass using conservation of mass of air;

Appendix D

Favre's averaging of energy conservation equation

To begin with, we write the equation of energy conservation.

$$\frac{\partial}{\partial t}\left(\rho c_p T\right) + \boldsymbol{\nabla}\cdot\left(\rho \boldsymbol{U} c_p T\right) = \frac{\mathrm{d}P_{\mathrm{th}}}{\mathrm{d}t} - \boldsymbol{\nabla}\cdot\boldsymbol{q}, \tag{D.1}$$

where the heat flux is defined by

$$\boldsymbol{q} = -\lambda\boldsymbol{\nabla}T + \sum_k c_{p,k} T \boldsymbol{j}_k, \tag{D.2}$$

and the mass flux is defined by

$$\boldsymbol{j}_k = \rho D \boldsymbol{\nabla} Y_k. \tag{D.3}$$

We see that beside the term of convection $\rho\boldsymbol{U}c_pT$, non-linearity also appears in the term of species interdiffusion.

Generally, assuming $A = \overline{a}$, $B = \overline{b}$ and $C = \overline{c}$, on obtains

$$\overline{abc} = \overline{(A + a')(B + b')(C + c')} \tag{D.4}$$

$$= ABC + \overline{a'BC} + \overline{Ab'C} + \overline{ABc'} + \overline{Ab'c'} + \overline{a'Bc'} + \overline{a'b'C} + \overline{a'b'c'} \tag{D.5}$$

$$= ABC + \overline{Ab'c'} + \overline{a'Bc'} + \overline{a'b'C} + \overline{a'b'c'}, \tag{D.6}$$

where one shall modelize all the terms containing fluctuation by

$$\overline{Ab'c'} + \overline{a'Bc'} + \overline{a'b'C} + \overline{a'b'c'} \sim f(A, B, C). \tag{D.7}$$

By averaging the convection term, one obtains

$$\overline{\boldsymbol{\nabla} \cdot (\rho \boldsymbol{U} c_p T)} \sim \boldsymbol{\nabla} \cdot \left(\overline{\rho} \widetilde{\boldsymbol{U}} \overline{c_p} \widetilde{T} \right) + \boldsymbol{\nabla} \cdot \boldsymbol{q}_{t,C}, \tag{D.8}$$

where the turbulent flux is usually modelized by

$$\boldsymbol{q}_{t,C} = -\lambda_{t,C} \boldsymbol{\nabla} \widetilde{T}. \tag{D.9}$$

Idem for the species interdiffusion term:

$$\overline{c_{p,k} T \rho D \boldsymbol{\nabla} Y_k} \sim c_{p,k} \widetilde{T} \overline{\rho} D \boldsymbol{\nabla} \widetilde{Y}_k + \lambda_{t,k} \boldsymbol{\nabla} \widetilde{T} \tag{D.10}$$

By assuming $\overline{\rho c_p T} \sim \overline{\rho}\, \overline{c_p} \widetilde{T}$, one obtains

$$\frac{\partial}{\partial t} \left(\overline{\rho c_p T} \right) + \boldsymbol{\nabla} \cdot \left(\overline{\rho} \widetilde{\boldsymbol{U}} \overline{c_p} \widetilde{T} \right) = \frac{\mathrm{d} \overline{P_{\mathrm{th}}}}{\mathrm{d} t} - \boldsymbol{\nabla} \cdot \left(\overline{\boldsymbol{q}} + \boldsymbol{q}_t \right), \tag{D.11}$$

where the turbulent heat flux is defined by

$$\boldsymbol{q}_t = -\left(\lambda_{t,C} + \lambda_{t,I}\right) \boldsymbol{\nabla} \widetilde{T} = -\lambda_t \boldsymbol{\nabla} \widetilde{T} = -\frac{\mu_t}{\sigma_T} \boldsymbol{\nabla} \widetilde{T}. \tag{D.12}$$

Thus, if ρ does not vary very largely, $\overline{T} \sim \widetilde{T}$ and one obtains $\overline{\boldsymbol{q}} = \lambda \boldsymbol{\nabla} \widetilde{T}$ thus

$$\frac{\partial}{\partial t}\left(\overline{\rho c_p T}\right) + \boldsymbol{\nabla} \cdot \left(\overline{\rho} \widetilde{\boldsymbol{U}} \overline{c_p} \widetilde{T}\right) = \frac{\mathrm{d}\overline{P_{\mathrm{th}}}}{\mathrm{d}t} + \boldsymbol{\nabla} \cdot \left(\left(\lambda + \frac{\mu_t}{\sigma_T}\right) \boldsymbol{\nabla} \widetilde{T} + \overline{\rho} \widetilde{T} D_k \sum_k c_{p,k} \boldsymbol{\nabla} \widetilde{Y_k}\right), \tag{D.13}$$

which writes in the binary fluid mixture case,

$$\frac{\partial}{\partial t}\left(\overline{\rho c_p T}\right) + \boldsymbol{\nabla} \cdot \left(\overline{\rho} \widetilde{\boldsymbol{U}} \overline{c_p} \widetilde{T}\right) = \frac{\mathrm{d}\overline{P_{\mathrm{th}}}}{\mathrm{d}t} + \boldsymbol{\nabla} \cdot \left(\left(\lambda + \frac{\mu_t}{\sigma_T}\right) \boldsymbol{\nabla} \widetilde{T} + \overline{\rho} \widetilde{T} D \left(c_{p,v} - c_{p,a}\right) \boldsymbol{\nabla} \widetilde{Y_v}\right), \tag{D.14}$$

$$\widetilde{h} = \widetilde{\overline{c_p} T} = \widetilde{\sum_k c_{p,k} T} = \sum_k c_{p,k} \widetilde{Y_k T} \tag{D.15}$$

It is supposed that the pressure P_{th} is constant.

$$\rho \left[r_a + \left(r_v - r_a\right) Y_v\right] T = P_{\mathrm{th}} \tag{D.16}$$

Appendix E

Contribution of sensible and latent heat fluxes

In Bucci's thesis [Bucci, 2009], the ratio of the sensible heat flux $\Phi_{w,s}$ and the mass flux ϕ_w on the wall is expressed by

$$\frac{\Phi_{w,s}}{\phi_w} = \frac{c_p\left(T_w - T_b\right)}{\frac{Y_{v,w}-Y_{v,b}}{1-Y_{v,w}}}\mathrm{Le}^{2/3}, \tag{E.1}$$

where the Lewis number is defined as $\mathrm{Le} = \mathrm{Sc}/\mathrm{Pr} = k/(\rho c_p D)$. However, the species interdiffusion is not taken into account in this equation.

One shall write the expressions of the mass flux by diffusion $\mathbf{j}_d$, the heat flux by diffusion $\mathbf{q}_d$ and the heat flux by interdiffusion $\mathbf{q}_i$.

$$\boldsymbol{j}_{\mathrm{d}} = -\rho D \boldsymbol{\nabla} Y_v \tag{E.2}$$

$$\boldsymbol{q}_{\mathrm{d}} = -\lambda \boldsymbol{\nabla} T \tag{E.3}$$

$$\boldsymbol{q}_{\mathrm{i}} = -\left(c_{p,v} - c_{p,a}\right) T \rho D \boldsymbol{\nabla} Y_v \tag{E.4}$$

By definition of Nusselt and Sherwood numbers, one shall have:

$$\phi_w = \mathrm{Sh} \cdot \rho D \frac{Y_{v,w} - Y_{v,b}}{\Delta y \left(1 - Y_{v,w}\right)} \tag{E.5}$$

$$\Phi_{w,d} = \mathrm{Nu}_d \cdot \lambda \frac{T_w - T_b}{\Delta y} \tag{E.6}$$

On the other hand,

$$\Phi_{w,i} = \left(c_{p,v} - c_{p,a}\right) T_w \cdot \mathrm{Sh} \cdot \rho D \frac{Y_{v,w} - Y_{v,b}}{\Delta y \left(1 - Y_{v,w}\right)} \tag{E.7}$$

Thus, considering that the heat and mass transfer analogy shall still works between diffusion and conduction according to the results in Chapter 3, one shall calculate:

$$\begin{aligned}
\frac{\Phi_{w,s}}{\phi_w} &= \frac{\Phi_{w,d} + \Phi_{w,i}}{\phi_w} \\
&= \frac{\Phi_{w,d}}{\phi_w} + \frac{\left(c_{p,v} - c_{p,a}\right) T_w \phi_w}{\phi_w} \\
&= \frac{c_p \left(T_w - T_b\right)}{\frac{Y_{v,w} - Y_{v,b}}{1 - Y_{v,w}}} \mathrm{Le}^{2/3} + \left(c_{p,v} - c_{p,a}\right) T_w.
\end{aligned}$$

That leads to a bigger sensible heat flux than Bucci's estimation, thus a smaller mass flux.

Appendix F

Résumé substantiel en langue française

Lors d'un accident de perte de réfrigérant primaire (APRP) dans une centrale nucléaire, la vaporisation de l'eau du circuit primaire entraîne à l'augmentation de la pression dans l'enceinte de confinement. Par contre, cette augmentation est limitée par la condensation en paroi. la modélisation de la condensation en paroi en présence de gaz incondensables nécessite la considération un couplage du transfert de chaleur et du transfert de masse, qui met en jeu l'interdiffusion des espèces. Le flux de cette dernière représente la différence entre la somme des flux convectifs partiels et le flux convectif total. Or cet effet est généralement négligé dans la littérature sans justification claire.

Pour étudier l'influence de l'interdiffusion des espèces sur la condensation en film, j'ai travaillé en 3 étapes dans cette thèse.

F.1 Cas laminaire : effets de couplage des transferts de chaleur et de masse

L'effet de l'interdiffusion est d'abord examiné dans le régime laminaire en considérant le mélange binaire d'un gaz condensable et d'un incondensable dans une cavité carrée différentiellement chauffée avec des films liquides. Les phénomènes considérés sont la convection naturelle et la condensation, qui est modélisée avec une vitesse de Stefan. L'hypothèse du bas nombre de Mach est posée pour filtrer les ondes acoustiques. Un solveur est réalisé sur le plateforme OpenFOAM en adaptant l'algorithme PISO pour le modèle à bas Mach.

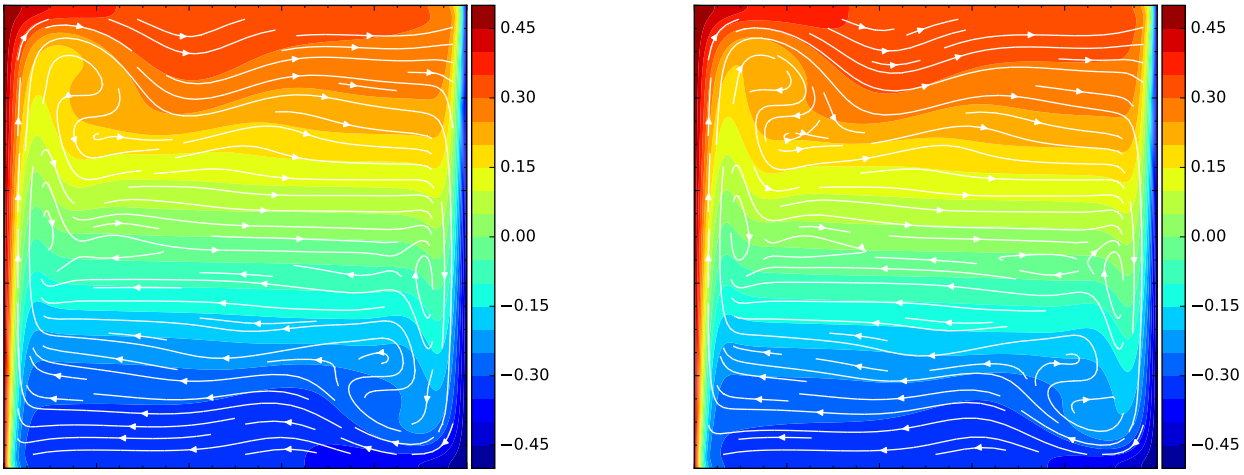

(a) T^* sans interdiffusion (b) T^* avec interdiffusion

Figure F.1: Comparaison des champs de température adimensionnelle (T^*) sans et avec interdiffusion (voir FIG. 3.2)

Les calculs de différents cas ont montré que la contribution de l'interdiffusion au transfert de chaleur est significative lorsque la différence de capacité thermique entre les deux espèces n'est pas négligeable et que le flux de masse est important. De plus, la conservation de l'énergie ne s'établit que si l'interdiffusion des espèces prise en compte dans le modèle. L'influence des effets Soret et Dufour a également été examinée dans cette étude. Il a été établi que ces effets peuvent être négligés pour un mélange d'air et de vapeur. Mais lorsque le facteur de diffusion thermique est élevé, l'effet Dufour peut avoir

une influence importante donc il faut faire attention aux autres compositions du mélange.

Cet étape est décrit dans le chapitre 3.

F.2 Cas turbulent : application des modèles de turbulence à bas Reynolds pour l'effet de la condensation

Nous avons ensuite considéré le régime turbulent. Nous nous sommes dans un premier temps intéressés aux capacités des modèles bas Reynolds (Chien, Launder-Sharma).

Après une validation pour l'écoulement de canal classique (sans aspiration), nous avons validé ces modèles avec l'expérience de Favre où l'aspiration est présente. Nous avons montré que ces modèles sont capables de prédire correctement l'effet d'aspiration dans une couche limite turbulente.

Ensuite nous avons étudié l'écoulement de canal en présence de condensation et comparé le modèle avec les essais COPAIN. Nous avons trouvé que ces modèles sont capables d'estimer de manière acceptable le profil de température, et de manière moins cohérente le profil de la fraction de masse. Toutefois il est possible que ce manque d'accord soit dû à la technique de mesure dans les expériences.

Cet étape est décrit dans le chapitre 4.

F.3 Cas turbulent : extension des fonctions de paroi pour la condensation

Nous avons dans un deuxième temps cherché à capturer les couplages ainsi que les variations des propriétés physiques en construisant des fonctions de paroi généralisées.

La méthode que nous proposons s'appuie sur la résolution d'un système d'équations aux dérivées ordinaires et fait intervenir le modèle de longueur de mélange avec le facteur d'amortissement de van Driest. Les profils et flux prédits par la méthode ont été comparés avec les modèles bas Reynolds ainsi que des résultats expérimentaux pour trois types de cas: une couche limite avec aspiration (ou soufflage), une couche limite avec aspiration et transfert thermique, et enfin une couche limite avec transfert de masse et de chaleur couplé. Nous avons montré que le paramètre d'amortissement dépend de la vitesse d'aspiration.

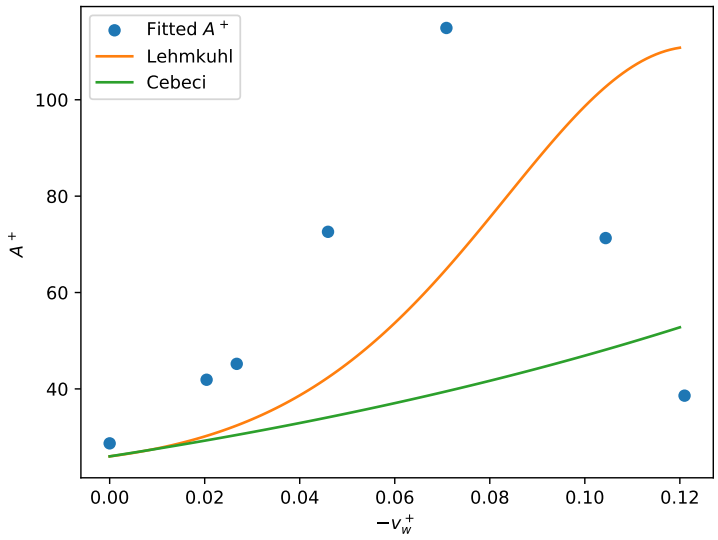

Figure F.2: Variation de A^+ la constante du facteur d'amortissement de Van Driest en fonction du taux d'aspiration $-v_w^+$ comaprée avec les prédictions existantes (voir FIG. 5.4)

Enfin, nous avons établi que la prise en compte de l'interdiffusion conduit à une amélioration substantielle de l'accord du modèle de paroi avec les résultats expérimentaux.

Cet étape est décrit dans le chapitre 5.

F.4 Conclusions et perspectives

L'interdiffusion des espèces est un effet de couplage du transfert de chaleur et de masse. Cet effet est souvent oublié mais il est important quand la différence des capacités thermiques et le flux de masse sont élevés.

Dans le régime laminaire, les effets de couplage ont été quantifiés précisément en convection naturelle pour un mélange air-vapeur, dans le cas d'une cavité carrée différentiellement chauffée avec condensation à la paroi. Les résultats montrent que l'influence de l'interdiffusion est importante mais que celle des effets Soret et Dufour est négligeable.

Dans le cas turbulent, des fonctions de paroi étendues ont été obtenues par résolution d'un système d' équations différentielles ordinaires pour la couche limite construit à partir du modèle de longueur de mélange et d'un facteur d'amortissement de Van Driest qui dépend de l'aspiration. Les résultats sont en bon accord avec les mesures expérimentales et avec les calculs des modèles de turbulence à bas nombre de Reynolds, qui prédisent correctement l'effet de l'aspiration. Les comparaisons montrent aussi qu'il est nécessaire de prendre en compte l'interdiffusion des espèces dans la modélisation.

Dans la suite de ce travail, les fonctions de paroi étendues devront être intégrées dans les modèles RANS à haut Reynolds. Pour améliorer la modélisation des fonctions de paroi, on pourra prendre en compte la variation du cisaillement dans le facteur d'amortissement, examiner d'autres modélisations pour la contribution turbulente de l'interdiffusion, et également faire varier Pr_t et Sc_t avec la distance à la paroi. Par ailleurs, il serait utile de disposer de données expérimentales plus complètes pour la validation, avec des mesures des trois champs u^+, T^+ et Y^+ à la fois. Finalement le modèle physique lui-même pourra être étendu : on pourra d'une part inclure la flottabilité dans le cas de la

convection naturelle turbulente et d'autre part modéliser directement le film liquide pour prendre en compte les effets de ruissellement.

Bibliography

K. Abe, T. Kondoh, and Y. Nagano. A new turbulence model for predicting fluid flow and heat transfer in separating and reattaching flows I. Flow field calculations. *International Journal of Heat and Mass Transfer*, 37(1):139–151, Jan. 1994.

D. Ackermann. Warme und Stoffubergangskoeffizienten bei der Abkuhlung von Dampf Gas Gemischen in Oberflachenkondensatoren. *Chemie Ingenieur Technik*, 44(5):274–280, 1972.

W. Ambrosini, N. Forgione, A. Manfredini, and F. Oriolo. On various forms of the heat and mass transfer analogy: Discussion and application to condensation experiments. *Nuclear Engineering and Design*, 236(9):1013–1027, May 2006.

W. Ambrosini, N. Forgione, F. Merli, F. Oriolo, S. Paci, I. Kljenak, P. Kostka, L. Vyskocil, J. Travis, J. Lehmkuhl, S. Kelm, Y.-S. Chin, and M. Bucci. Lesson learned from the SARNET wall condensation benchmarks. *ERMSAR 2013 conference of the SARNET network*, 74:153–164, Dec. 2014.

ANSYS, Inc. ANSYS CFX-Solver Theory Guide and Solver Modeling Guide, Release 15. Technical report, ANSYS Inc., Canonsburg, 2013.

P. Bahavar and C. Wagner. Condensation-induced flow structure modifications in turbulent channel flow investigated in direct numerical simulations. *Physics of Fluids*, 32(1): 015115, Jan. 2020.

P. Bazin and P. Castelli. Validation d'un modele de condensation sur la base des resultats experimentaux COPAIN. Technical Report Note SETEX/LETS/2000-102, CEA, 2000.

S. Benteboula and F. Dabbene. Modeling of wall condensation in the presence of noncondensable light gas. *International Journal of Heat and Mass Transfer*, 151:119313, Apr. 2020.

A. S. L. Bergman, D. P. DeWitt, and F. P. Incropera. *Introduction to heat and mass transfer*. Wiley, 2006.

H. Bian, Z. Sun, N. Zhang, Z. Meng, and M. Ding. A new modified diffusion boundary layer steam condensation model in the presence of air under natural convection conditions. *International Journal of Thermal Sciences*, 145:105948, Nov. 2019.

R. B. Bird, W. E. Stewart, and E. N. Lightfoot. *Transport phenomena*, volume 1. John Wiley & Sons, 2006.

M. Bucci. Experimental and Computational Analysis of Condensation Phenomena for the Thermalhydraulic Analysis of LWRs Containments. Technical report, Thesis of Pisa University, 2009.

M. Bucci, M. Sharabi, W. Ambrosini, N. Forgione, F. Oriolo, and S. He. Prediction of transpiration effects on heat and mass transfer by different turbulence models. *Nuclear Engineering and Design*, 238(4):958–974, Apr. 2008.

W. Cabot and P. Moin. Approximate wall boundary conditions in the large-eddy simulation of high Reynolds number flow. *Flow, Turbulence and Combustion*, 63(1-4):269–291, 2000.

O. Cabrit and F. Nicoud. Direct simulations for wall modeling of multicomponent reacting compressible turbulent flows. *Physics of Fluids*, 21(5):055108, 2009.

Cast3M. Accueil — Cast3M, 2019. URL `www-cast3m.cea.fr`.

T. Cebeci. Behavior of turbulent flow near a porous wall with pressure gradient. *AIAA Journal*, 8(12):2152–2156, 1970.

P. Chatelard, N. Reinke, S. Arndt, S. Belon, L. Cantrel, L. Carenini, K. Chevalier-Jabet, F. Cousin, J. Eckel, F. Jacq, C. Marchetto, C. Mun, and L. Piar. ASTEC V2 severe accident integral code main features, current V2.0 modelling status, perspectives. *Nuclear Engineering and Design*, 272:119–135, June 2014.

K. Y. Chien. Predictions of channel and boundary-layer flows with a low-Reynolds number turbulence model. *AIAA Journal*, 20(1):33–39, 1982.

T. Craft, S. Gant, H. Iacovides, and B. E. Launder. Development and application of a new wall function for complex turbulent flows. In *ECCOMAS Computational Fluid Dynamics Conference*, Swansea, Wales, 2001.

T. Craft, A. Gerasimov, H. Iacovides, and B. Launder. Progress in the generalization of wall-function treatments. *International Journal of Heat and Fluid Flow*, 23(2):148–160, 2002a.

T. J. Craft, A. V. Gerasimov, H. Iacovides, and B. E. Launder. Progress in the generalization of wall-function treatments. *International Journal of Heat and Fluid Flow*, 23(2):148–160, 2002b.

G. De Vahl Davis. Natural convection in a square cavity: a comparison exercise. *International Journal for numerical methods in fluids*, 3:227–248, 1983a.

G. De Vahl Davis. Natural convection of air in a square cavity: a benchmark numerical solution. *International Journal for numerical methods in fluids*, 3:249–264, 1983b.

C. Duprat, G. Balarac, O. Metais, P. M. Congedo, and O. Brugiere. A wall-layer model for large-eddy simulations of turbulent flows with/out pressure gradient. *Physics of fluids*, 23(1):015101, 2011.

P. A. Durbin. Limiters and wall treatments in applied turbulence modeling. *Fluid Dynamics Research*, 41(1):012203, Jan. 2009.

P. A. Durbin and A. Petterson Reif. *Statistical theory and modeling for turbulent flows*. John Wiley & Sons, 2001.

A. Favre. Equations statistiques des gaz turbulents -masse, quantite de mouvement. *Compte-rendus hebdomadaires de l'academie des sciences*, 246(18):2576–2579, 1958. Publisher: GAUTHIER-VILLARS/EDITIONS ELSEVIER 23 RUE LINOIS, 75015 PARIS, FRANCE.

A. Favre, R. Dumas, E. Verollet, and M. Coantic. Couche limite turbulente sur paroi poreuse avec aspiration. *Journal de Mecanique*, 5(1):3–28, 1966.

M. Ferro. *Experimental study on turbulent boundary-layer ows with wall transpiration*. PhD Thesis, Royal Institute of Technology Department of Mechanics, Stockholm, Sweden, 2017.

L. Frazza, A. Loseille, and F. Alauzet. Mesh adaptation strategies using wall functions and low-reynolds models. *Fluid Dynamics Conference, AIAA AVIATION Forum*, 2018.

L. Fulachier, E. Verollet, and I. Dekeyser. Resultats experimentaux concernant une couche limite turbulente avec aspiration et chauffage a la paroi. *International Journal of Heat and Mass Transfer*, 20(7):731–739, July 1977.

A. V. Gerasimov. *Development and validation of an analytical wallfunction strategy for modelling forced, mixed and natural convection phenomena*. PhD thesis, Ph. D. Thesis. UMIST, Manchester, UK, 2003.

J. Green and K. Almenas. An overview of the primary parameters and methods for determining condensation heat transfer to containment structures. *Nuclear Safety*, 37:26–48, 1996.

J. Hinze. *Turbulence*. Mc Graw - Hill, 1976.

M. Holling and H. Herwig. Asymptotic analysis of the near-wall region of turbulent natural convection flows. *Journal of Fluid Mechanics*, 541:383–397, 2005.

A. Hundhausen, H. Muller, S. Kelm, E. A. Reinecke, and H.-J. Allelein. Towards CFD-grade measurements in a condensing boundary layer - First results of the new SETCOM facility. In *ERMSAR*, Warsaw, Poland, 2017.

C. B. Hwang and C. A. Lin. Improved low-Reynolds-number k-epsilon model based on direct numerical simulation data. *AIAA journal*, 36(1):38–43, 1998.

N. Jiang and E. Studer. Interpretation des essais COPAIN avec un modele de turbulence a bas nombre de Reynolds : mesures locales et analyses. Technical Report DES/ISAS/DM2S/STMF/LATF/NT/2020-66522/A, CEA, 2020.

W. P. Jones and B. E. Launder. The prediction of laminarization with a two-equation model of turbulence. *International Journal of Heat and Mass Transfer*, 15:301–314, 1972.

B. A. Kader. Temperature and concentration profiles in fully turbulent boundary layers. *International Journal of Heat and Mass Transfer*, 24(9):1541–1544, 1981.

G. Kalitzin, G. Medic, G. Iaccarino, and P. A. Durbin. Near-wall behavior of RANS turbulence models and implications for wall functions. *Journal of Computational Physics*, 204:265–291, 2005.

W. M. Kays. Heat transfer to the transpired turbulent boundary layer. *International Journal of Heat and Mass Transfer*, 15:1023–1044, 1972.

G. R. Kefayati. FDLBM simulation of entropy generation in double diffusive natural convection of power-law fluids in an enclosure with Soret and Dufour effects. *International Journal of Heat and Mass Transfer*, 89:267–290, 2015. Publisher: Elsevier.

G. R. Kefayati. Simulation of double diffusive natural convection and entropy generation of power-law fluids in an inclined porous cavity with Soret and Dufour effects (Part II:

Entropy generation). *International Journal of Heat and Mass Transfer*, 94:582–624, 2016a. Publisher: Elsevier.

G. R. Kefayati. Simulation of double diffusive natural convection and entropy generation of power-law fluids in an inclined porous cavity with Soret and Dufour effects (Part II: Entropy generation). *International Journal of Heat and Mass Transfer*, 94:582–624, 2016b. Publisher: Elsevier.

S. Kelm, H. Muller, A. Hundhausen, C. Druska, A. Kuhr, and H. Allelein. Development of a multi-dimensional wall-function approach for wall condensation. *Nuclear Engineering and Design*, 353:110239, Nov. 2019.

M. Kim and M. Corradini. Modeling of condensation heat transfer in a reactor containment. *Nuclear Engineering Design*, 118:87–102, 1990.

C. K. G. Lam and K. Bremhorst. A Modified Form of the k-epsilon Model for Predicting Wall Turbulence. *Journal of Fluids Engineering*, 103(3):456–460, Sept. 1981.

R. Landis and A. Mills. The calculation of turbulent boundary layers with foreign gas injection. *International Journal of Heat and Mass Transfer*, 15(10):1905–1932, 1972. Publisher: Elsevier.

B. E. Launder and B. I. Sharma. Application of the nergy-dissipation model of turbulence to the calculation of flow near a spinning disc. *Letters in Heat and Mass transfer*, 1: 131–138, 1974.

B. E. Launder and D. B. Spalding. The numerical computation of turbulent flows. *Computational Methods in Apllied Mechanical Engieering*, 3(3):269–289, 1974.

P. Le Quéré, C. Weisman, H. Paillère, J. Vierendeels, E. Dick, R. Becker, M. Braack, and J. Locke. Modelling of natural convection flows with large temperature differences: a benchmark problem for low Mach number solvers. Part 1. Reference solutions. *ESAIM:*

Mathematical Modelling and Numerical Analysis, 39(3):609–616, 2005. Publisher: EDP Sciences.

C. Leduc. *Modelisation de la condensation en film sur les paroi d'une enceinte de reacteur*. PhD thesis, Universite Joseph Fourier, Grenoble 1, 1995.

J. Lee, G.-C. Park, and H. K. Cho. Simulation of wall film condensation with non-condensable gases using wall function approach in component thermal hydraulic analysis code CUPID. *Journal of Mechanical Science and Technology*, 32(3):1015–1023, Mar. 2018.

F. Legay-Desesquelles and B. Prunet-Foch. Dynamic behaviour of boundary layer with condensation along a flat plate: comparison with suction. *International Journal of Heat and Mass Transfer*, 28(12):2363–2370, 1985.

J. Lehmkuhl, S. Kelm, M. Bucci, and H. J. Allelein. Improvment of wall condensation modeling with suction wall functions for containment applications. *Nuclear Engineering and Design*, 299:105–111, 2016.

W. Li, C. Zhang, T. Chen, J. Min, D. Senechal, and S. Mimouni. A unified wall function for wall condensation modelling in containment multi-component flows. *Nuclear Engineering and Design*, 348:24–36, July 2019.

L. Magalhães, A. Silva, and J. Barata. Locally variable turbulent Prandtl number considerations on the modeling of Liquid Rocket Engines operating above the critical point. In *ILASS–Europe 2019, 29th Conference on Liquid Atomization and Spray Systems*, Paris, France, 2019.

J. Malet, E. Porcheron, and J. Vendel. OECD International Standard Problem ISP 47 on containment thermalhydraulics Conclusions of the TOSQAN part. *4th International Topical Meeting on High Temperature Reactor Technology (HTR 2008), with Regular Papers*, 240(10):3209–3220, Oct. 2010.

J. Malet, E. Porcheron, F. Dumay, and J. Vendel. Code experiment comparison on wall condensation tests in the presence of non condensable gases Numerical calculations for containment studies. *SI : CFD4NRS-3*, 253:98–113, Dec. 2012.

N. N. Mansour, J. Kim, and P. Moin. Reynolds-stress and dissipation-rate budgets in a turbulent channel flow. *Journal of Fluid Mechanics*, 194:15–44, 1988.

T. R. Marrero and E. A. Mason. Gaseous diffusion coefficients. *J. Phys. Chem. Ref. Data*, 1(1):3–83, 1972.

E. Mason and S. Saxena. Approximate formula for the thermal conductivity of gas mixtures. *The Physics of fluids*, 1(5):361–369, 1958. Publisher: American Institute of Physics.

E. A. Mason. Higher approximations for the transport properties of binary gas mixtures. I. General formulas. *The Journal of Chemical Physics*, 27(1):75–84, 1957. Publisher: American Institute of Physics.

J. Meinert, J. Huhn, E. Serbest, and O. J. Haidn. Turbulent Boundary Layers with Foreign Gas Transpiration. *Journal of Spacecraft and Rockets*, 38(2):191–198, mar 2001.

B. Mohammadi and G. Puigt. Wall functions in computational fluid mechanics. *Computers & Fluids*, 35(10):1108–1115, 2006.

L. Monchick and E. Mason. Transport properties of polar gases. *The Journal of Chemical Physics*, 35(5):1676–1697, 1961. Publisher: American Institute of Physics.

R. D. Moser, J. Kim, and N. N. Mansour. Direct numerical simulation of turbulent channel flow up to Re=590. *Physics of Fluids*, 11(4):943–945, Mar. 1999.

I. A. Mudawwar and M. A. El-Masri. Momentum and heat transfer across freely-falling turbulent liquid films. *International journal of multiphase flow*, 12(5):771–790, 1986.

H. Muller, J. Lehmkuhl, S. Kelm, A. Hundhausen, A. Belt, and H. J. Allelein. Development of a wall condensation model for coarse mesh containment scale applications. In *Proc.*

OECD/NEA and IAEA Workshop Experiments and CFD Codes Application to Nuclear Reactor Safety (CFD4NRS), pages 9–13, 2016.

D. Muto, Y. Daimon, T. Shimizu, and H. Negishi. An equilibrium wall model for reacting turbulent flows with heat transfer. *International Journal of Heat and Mass Transfer*, 141: 1187–1195, 2019.

W. Nusselt. De oberflachenkondensation des waserdampfes. *Z Vereines Deutch. Ing.*, 60: 541–546, 1916.

S. Oh and S. T. Revankar. Boundary layer analysis for steam condensation in a vertical tube with noncondensable gases. *International Journal of Heat Exchangers*, 6(1524-5608):93–123, 2005.

H. Paillère. Modelling of natural convection flows with large temperature differences: A benchmark problem for low Mach number solvers. Part 2. Contributions to the June 2004 conference. *ESAIM: M2AN*, 39(3):617–621, 2005.

S. Paolucci. On the filtering of sound from the Navier Stokes equations. Technical report, Sandia National Laboratories SAND82-8257, 1982.

C. H. Park and S. O. Park. On the limiters of two-equation turbulence models. *International Journal of Computational Fluid Dynamics*, 19(1):79–86, Jan. 2005.

S. V. Patankar. *Heat and mass transfer in turbulent boundary layers*. PhD thesis, Faculty of Engineering, Univesity of London, 1967. Publisher: Imperial College London.

V. C. Patel, W. Rodi, and G. Scheuerer. Turbulence models for near-wall and low Reynolds number flow : a review. *AIAA Journal*, 23(9):1308–1319, 1985.

P. Peterson. Theoretical basis for the uchida correlation for condensation in reactor containments. *Nuclear Engineering and Design*, 162:301–306, 1996.

B. E. Poling, J. M. Prausnitz, and J. P. O'connell. *Properties of gases and liquids*. McGraw-Hill Education, 2001.

S. B. Pope. *Turbulent flow*. Cambridge University Press, 2000.

W. M. Rohsenow. Effect of vapor velocity on laminar and turbulent film condensation. *Transactions of ASME*, pages 1645–1648, 1956.

A. Sarkar and R. So. A critical evaluation of near-wall two-equation models against direct numerical simulation data. *International Journal of Heat and Fluid Flow*, 18(2):197–208, Apr. 1997.

T. Shih, L. Povinelli, N. Liu, M. Potapczuk, and J. Lumley. A generalized wall function. Technical report, NASA TM_1999-209398, July 1999.

T. H. Shih and Z. Yang. New time scale based k-epsilon model for near-wall turbulence. Technical report, NASA Lewis Research Center, July 1993. URL `http://ntrs.nasa.gov/search.jsp?R=19930057912`.

T.-H. Shih, L. A. Povinelli, and N.-S. Liu. Application of generalized wall function for complex turbulent flows. In W. RODI and N. FUEYO, editors, *Engineering Turbulence Modelling and Experiments 5*, pages 177–186. Elsevier Science Ltd, Oxford, 2002.

R. L. Simpson. The turbulent boundary layer on a porous plate: an experimental study of the fuidl dynamics with injection and suction. Technical report, PhD Stanford University, 1968.

C. Srinivasan and D. V. Papavassiliou. Prediction of the Turbulent Prandtl Number in Wall Flows with Lagrangian Simulations. *Industrial & Engineering Chemistry Research*, 50 (15):8881–8891, aug 2011.

K. Suga, T. Craft, and H. Iacovides. An analytical wall-function for turbulent flows and heat transfer over rough walls. *International Journal of Heat and Fluid Flow*, 27:852–866, 2006.

H. Sun, G. Lauriat, D. Sun, and W. Tao. Transient double-diffusive convection in an enclosure with large density variations. *International Journal of Heat and Mass Transfer*, 53 (4):615–625, 2010.

W. Sutherland. LII. The viscosity of gases and molecular force. *The London, Edinburgh, and Dublin Philosophical Magazine and Journal of Science*, 36(223):507–531, 1893. Publisher: Taylor & Francis _eprint: https://doi.org/10.1080/14786449308620508.

T. Tagami. Interim report on safety assessments and facilities. *Unpublished Report*, 1965.

H. Tennekes and J. Lumley. *A first course in turbulence*. M.I.T Press, 1972.

J. Travis. An improved wall function approach for condensing and evaporating turbulent boundary layers in the GASFLOW-II code, 2007.

H. Uchida, A. Oyama, and Y. Togo. Evaluation of post-accident cooling systems of LWR's. In *Proccedings of the International Conference of the peaceful uses of Atomic Energy*, 1965.

S. Utyuzhnikov. Some new approaches to building and implementation of wall-functions for modeling of near-wall turbulent flows. *Computers & Fluids*, 34(7):771–784, 2005.

S. Utyuzhnikov. The method of boundary condition transfer in application to modeling near-wall turbulent flows. *Computers and Fluids*, 35:1193–1204, 2006.

E. R. Van Driest. On Turbulent Flow Near a Wall. *Journal of the Aeronautical Sciences*, 23(11):1007–1011, Nov. 1956. Publisher: American Institute of Aeronautics and Astronautics.

E. Verollet. Etude d'une couche limite turbulente avec aspiration et chauffage à la paroi. Technical report, Rapport CEA - R-4872, 1972.

J. Vierendeels, K. Riemslagh, and E. Dick. A Multigrid Semi-implicit Line-Method for Viscous Incompressible and Low-Mach-Number Flows on High Aspect Ratio Grids. *Journal of Computational Physics*, 154(2):310–341, 1999.

A. Wassiljewa. Warmeleitung in gasgemischen. *Physik. Z.*, 5:737–742, 1904.

J. Weaver and R. Viskanta. Natural convection due to horizontal temperature and concentration gradients—2. Species interdiffusion, Soret and Dufour effects. *International Journal of Heat and Mass Transfer*, 34(12):3121–3121–3133, Jan. 1991a.

J. A. Weaver and R. Viskanta. Natural convection due to horizontal temperature and concentration gradients—2. Species interdiffusion, Soret and Dufour effects. *International Journal of Heat and Mass Transfer*, 34(12):3121–3133, 1991b.

C. R. Wilke. A viscosity equation for gas mixtures. *The Journal of Chemical Physics*, 18 (4), 1950.

Z. Yang, T.-H. Shih, Lewis Research Center., and Institute for Computational Mechanics in Propulsion. *A k-epsilon modeling of near wall turbulence*. NASA Lewis Research Center, Institute for Computational Mechanics in Propulsion ; [For sale by the National Technical Information Service], Cleveland, Ohio; [Springfield, Va.], 1991.

J. M. Yoo, J. H. Kang, B. J. Yun, S. W. Hong, and J. J. Jeong. Improvement of the MELCOR condensation heat transfer model for the thermal-hydraulic analysis of a PWR containment. *Progress in Nuclear Energy*, 104:172–182, Apr. 2018.

D. S. Yoon, H. Jo, and M. L. Corradini. Cfd modeling of filmwise steam condensation with noncondensable gas with modified boundary condition. *International Journal of Heat and Mass Transfer*, 125:485–493, 2018.

I. Zadrazil, O. K. Matar, and C. N. Markides. An experimental characterization of downwards gas-liquid annular flow by laser-induced fluorescence: Flow regimes and film statistics. *International Journal of Multiphase Flow*, 60:87–102, 2014.

L. Zaichik, B. Nigmatulin, V. Alipchenkov, and V. Belov. Film condensation and aerosol deposition in turbulent flows with noncondensable gases. *Heat transfer Soviet Research*, 28(4-6):277–288, 1997.

université PARIS-SACLAY
ÉCOLE DOCTORALE
Sciences mécaniques et énergétiques, matériaux et géosciences (SMEMAG)

Titre : Incorporation de l'interdiffusion des espèces dans la modélisation de la couche limite de condensation en film avec des gaz incondensables

Mots clés : transfert de chaleur, transfert de masse, couche limite, condensation en film

Résumé : Le phénomène de condensation de la vapeur en présence de gaz incondensables met en jeu l'interdiffusion des espèces. Or cet effet est généralement négligé dans la littérature sans justification claire.
L'effet de l'interdiffusion est d'abord examiné dans le régime laminaire en considérant le mélange binaire d'un gaz condensable et d'un incondensable dans une cavité carrée différentiellement chauffée. Les phénomènes considérés sont la convection naturelle et la condensation, qui est modélisée avec une vitesse de Stefan. Les calculs de différents cas ont montré que la contribution de l'interdiffusion au transfert de chaleur est significative lorsque la différence de capacité thermique entre les deux espèces n'est pas négligeable et que le flux de masse est important. L'influence des effets Soret et Dufour a également été examinée dans cette étude. Il a été établi que ces effets peuvent être négligés pour un mélange d'air et de vapeur.
Nous avons ensuite considéré le régime turbulent. Nous nous sommes dans un premier temps intéressés aux capacités des modèles bas Reynolds (Chien, Launder-Sharma). Nous avons montré que ces modèles sont capables de prédire correctement l'effet d'aspiration dans une couche limite turbulente, d'estimer de manière acceptable le profil de température, et de manière moins cohérente le profil de la fraction de masse.
Nous avons dans un deuxième temps cherché à capturer les couplages ainsi que les variations des propriétés physiques en construisant des fonctions de paroi généralisées. La méthode que nous proposons s'appuie sur la résolution d'un système d'équations aux dérivées ordinaires et fait intervenir le modèle de longueur de mélange avec le facteur d'amortissement de van Driest. Les profils et flux prédits par la méthode ont été comparés avec les modèles bas Reynolds ainsi que des résultats expérimentaux pour trois types de cas: une couche limite avec aspiration (ou soufflage), une couche limite avec aspiration et transfert thermique, et enfin une couche limite avec transfert de masse et de chaleur couplé. Nous avons montré que le paramètre d'amortissement dépend de la vitesse d'aspiration. Enfin, nous avons établi que la prise en compte de l'interdiffusion conduit à une amélioration substantielle de l'accord du modèle de paroi avec les résultats expérimentaux.

Title: Incorporation of species interdiffusion in boundary layer modelling of filmwise condensation with non-condensable gases

Keywords: heat transfer, mass transfer, boundary layer, filmwise condensation

Abstract: Steam condensation in the presence of non-condensable gases involves species interdiffusion. Yet this effect is generally neglected in the literature without a clear justification.
We first examine the effect of species interdiffusion in the laminar regime. We consider a binary mixture of a condensable and a non-condensable gas in a differentially heated square cavity. The phenomena described by the numerical simulation are natural convection and condensation, which we model with a Stefan velocity. Examination of various cases shows that species interdiffusion can contribute significantly to the heat transfer when the mass flux is large and when the difference in the heat capacity of the two species is not small. In addition, we examine the influence of Dufour and Soret effects and find that both can be neglected for an air-steam mixture.
We then consider the turbulent regime. As a first step, we determine the prediction abilities of low Reynolds models such as the Chien and Launder-Sharma formulations by comparing them with experimental results. We show that the models are able to reproduce successfully the modification of the velocity profile due to wall suction and to estimate correctly the temperature profile. The mass fraction is not as well recovered, but there are reasons to believe that this could be at least partly due to a bias in experimental measurements.
As a second step, we build generalized wall functions to capture the different phenomena characterized by spatially-varying physical properties. Our method is grounded on a wall equilibrium model that leads to a system of ordinary differential equations. It relies on the mixing length assumption with the incorporation of a Van Driest damping factor. Results obtained with the method are confronted with low Reynolds model calculations and experimental measurements for three types of boundary layers: a purely kinetic boundary layer with suction/blowing, a boundary layer with suction and heat transfer, and a boundary layer with coupled heat and mass transfer. We determine how the damping factor depends on the wall suction. Finally, we establish that including the effect of interdiffusion is essential to obtain a good agreement of the wall function with experimental results.